CHALMERS
UNIVERSITY OF TECHNOLOGY

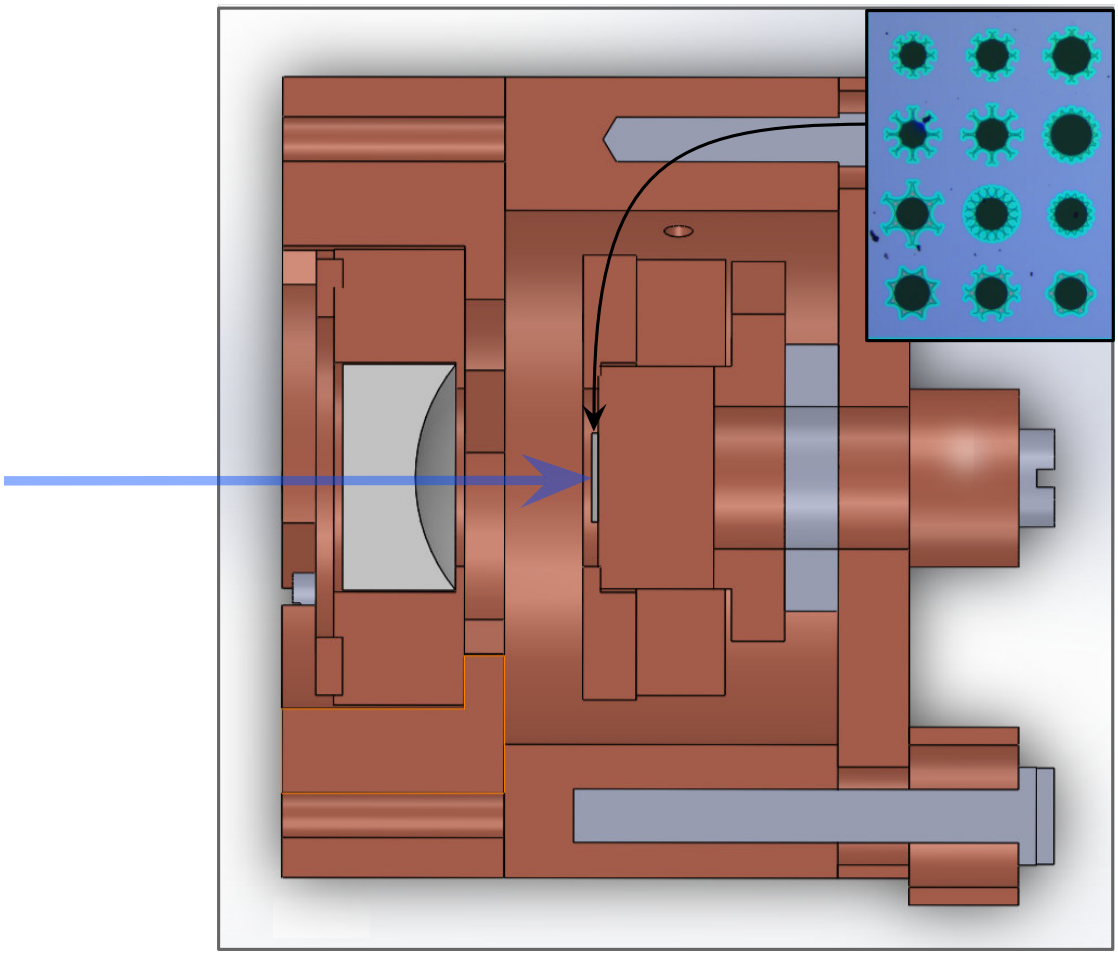

Towards cavity optomechanics with integrated multi-element mechanical resonators

Master's thesis in Physics

JOHAN KOLVIK

DEPARTMENT OF MICROTECHNOLOGY AND NANOSCIENCE

CHALMERS UNIVERSITY OF TECHNOLOGY
Gothenburg, Sweden 2021
www.chalmers.se

Master's thesis 2021

Towards cavity optomechanics with integrated multi-element mechanical resonators

Johan Kolvik

CHALMERS
UNIVERSITY OF TECHNOLOGY

Department of Microtechnology and Nanoscience
Quantum Technology lab
Mechanical quantum devices
Chalmers University of Technology
Gothenburg, Sweden 2021

Towards cavity optomechanics with integrated multi-element mechanical resonators

Johan Kolvik

Supervisors: Anastasiia Ciers, Sushanth Kini, Witlef Wieczorek, Department of Microtechnology and Nanoscience
Examiner: Witlef Wieczorek, Department of Microtechnology and Nanoscience

Master's Thesis 2021
Department of Microtechnology and Nanoscience
Quantum Technology lab
Mechanical quantum devices
Chalmers University of Technology
SE-412 96 Gothenburg
Telephone: +46 31 772 1000

Cover: Optomechanical cavity with integrated GaAs photonic crystal membrane devices.

Typeset in LaTeX
Printed by Chalmers Reproservice
Gothenburg, Sweden 2021

Towards cavity optomechanics with integrated multi-element mechanical resonators

Johan Kolvik
Department of Microtechnology and Nanoscience
Chalmers University of Technology

Abstract

Cavity optomechanics describes the interaction between an intracavity light field and a mechanical resonator. This mutual coupling allows for a means to optically control mechanical motion down to the quantum regime. Using an optomechanical device to observe non-linear quantum effects, such as direct generation of non-classical states, requires the strong single photon-phonon coupling regime, which is yet to be experimentally realized for chip-based devices. Coupling light to the collective motion of an array of highly reflective mechanical resonators has been predicted to increase the coupling strength and is therefore a promising way forward in achieving this goal.

In this thesis, I present the first steps towards realizing cavity optomechanics with multi-element membrane-type resonators fabricated from an AlGaAs heterostructure. The optical and mechanical properties of single- and double-layer resonators are characterized, showing resonance frequencies in the 100 kHz regime and room temperature mechanical quality factors of 10^4 at high vacuum. The reflectivity of the AlGaAs heterostructure is measured to be > 95 % at telecom wavelengths. The membrane devices are subsequently inserted as the back mirror of a 10 mm long Fabry-Pèrot-type cavity. This membrane-at-the-edge geometry shows a cavity linewidth of 6.38(8) MHz, corresponding to a finesse of 2370(30). Finally, an experimental setup for characterizing optomechanical properties is discussed, and its performance is analyzed in terms of cavity mirror impedance mismatch and membrane clipping loss.

Keywords: Cavity optomechanics, AlGaAs heterostructures, Micro-mechanical resonators, Optical measurement.

Acknowledgements

The completion of this thesis would not have been possible without the fantastic support of my supervisors Sushanth Kini, Anastasiia Ciers and Associate Prof. Witlef Wieczorek. During the project, they provided guidance when the way forward was unclear by asking questions that would make me see problems from novel points of view. Our scientific discussions have improved my way of thinking in ways which will be invaluable in my career going forward.

Individually, I want to first thank Witlef for allowing me to be a part of the optomechanics project and for challenging me to improve in every aspect of my scientific work. The lessons I've learned under your supervision will be not be easily forgotten. Secondly, I want to thank Sushanth for his everlasting support and down to earth argumentation. You provided a sense of calm by always having wise explanations for concepts of both simple and complex nature, whether it being in the office or in the lab. Lastly, I want to thank Anastasiia for her patience with my work in the lab and for the excellent help she provided with reflectivity simulations. I wish the three of you the best of luck with the project going forward and with all of your future endeavors.

I also want to thank the rest of the team working under Witlef's supervision, who provided a stimulating work environment during my stay in the group. I will miss discussing civic problems with Martí, helping Hanlin make his way into optomechanics, and get deep into unrelated physics discussions with Achintya. A special mention goes to Avan who provided support during the late nights leading up to the completion of this thesis.

Finishing this thesis also marks the end of my B.Sc. and M.Sc. education at Chalmers University of Technology. I would like to thank the Engineering Physics B.Sc. program, which at that time was under leadership of Prof. Jana Madjarova. This education sparked my interest for physics with its excellent and challenging courses. The Physics M.Sc. program along with valuable discussions with its coordinator Prof. Anders Hellman has provided guidance for me in finding the branch of physics that I want to pursue in my future career.

Outside of work, I want to thank my irreplaceable friends who help me to keep pursuing my goals. Those of you who provided mental support which helped me stay on track deserves a special mention, you make all doubts seem irrelevant. On a lighter note, I will sincerely miss the way too cold lunches on Origogården with the LB-gang which provided both goofy and interesting discussions, making for excellent breaks from work. And of course, I could not finish this section without thanking the all mighty Adrian.

Last but not least, I want to thank my family, whose support has been crucial for the finishing of this thesis. I want to thank my wonderful mother Åsa, sister Annie and father Jens, who understand me like none other. I send you my everlasting love.

Johan Kolvik, Gothenburg, August 2021

Table of Contents

List of Figures

List of Tables

1. Introduction

1.1 Radiation pressure

Optomechanics is a field of physics that focuses on the interaction between a mechanical resonator and the light field. This mutual interaction can for instance mediated by radiation pressure. Radiation pressure is a force acting on a body shined on by a source of light and originates from the momentum carried by the electromagnetic field. This momentum can be derived classically through Maxwell's equations. It can also be intuitively explained by the quantum description of light and its energy carrying particle, the photon. A photon carries the momentum $p = hf/c$ which is given by its frequency f weighted by the speed of light c and Plank's constant h. An elastic scattering process where a photon reflects off an object will thus transfer the momentum $\Delta p = h(f + f')/c$ where f, f' is the frequency of the light before and after reflection, see Figure 1.1.

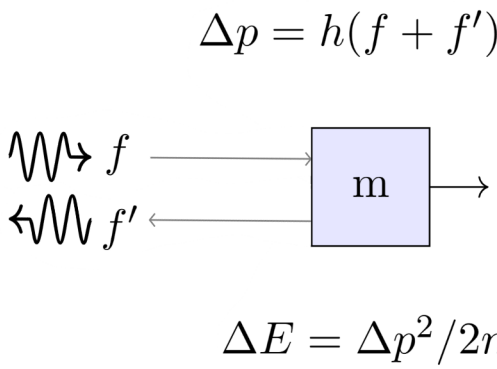

Figure 1.1: An incident photon of frequency f scatters on an object with mass m. Momentum and energy is conserved in the elastic process which leads to the exchanged quantities Δp and ΔE.

The change in the momentum indicates that a force has been exerted on the object. However, the interaction is very weak due to the magnitude of h and can thus be omitted in all circumstances. The radiation pressure of the sunlight hitting earth has a magnitude of about 10 pN/m^2, meaning that the face of a typical smartphone experiences a radiation pressure force equivalent to supporting a yeast cell against gravity. But even though the interaction is weak, it can still be observed in systems at appropriate mass and time scales. The first observation of the effect was made by Johannes Kepler as early as 1619 by studying the tails of comets in our solar system. The comets seemed to have two

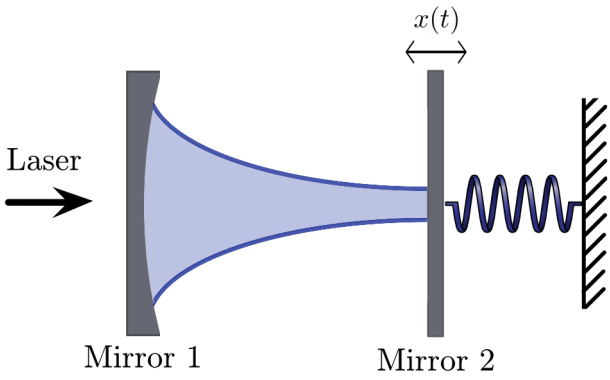

Figure 1.2: A schematic of the canonical cavity optomechanical system. Laser light is incident on a pair of mirrors forming a cavity. The back mirror of the cavity is allowed to move and is held in place by a spring, its motion in time described by $x(t)$. The light that enters the cavity circulates between the mirrors and, through radiation pressure, interacts with the back mirror.

different tails, one parallel to the comet velocity and one pointing away from the sun, as if pushed by some invisible force [1]. It was not until the early 1900s, however, that the effect would be experimentally shown in works done by Lebedev [2] and Nichols and Hull [3]. In the late 20th century, research on controlling the motion of small objects with light was gaining momentum. Starting in the 1970s, focused laser beams were utilized to trap atoms and ions [4] and the ability to cool ions with laser sidebands was demonstrated by Neuhauser in 1978 [5].

1.2 Cavity optomechanics

When increasing the mass of a mechanical object beyond the size of atoms and ions, the effect of the radiation pressure is very weak. Therefore, to study how light can control the motion of larger bodies, the intensity of the light field must be increased. This task can be performed by a cavity that confines electromagnetic radiation into a small region of space and enhances its intensity. Coupling this field to the mechanical motion thus allows for the study of light-matter interaction beyond the scale of atoms and ions. The interaction between an intracavity field and a mechanical resonator is described by cavity optomechanics [6].

The canonical cavity optomechanical system is shown in Figure 1.2 in which a laser is incident to an optical cavity, which is comprised of two mirrors. Crucially, the back mirror of the cavity is allowed to move and is attached to a spring, forming the mechanical resonator part of the system. In this configuration, photons entering the cavity are allowed to travel back and forth between the mirrors and interact with the mechanical resonator once every round trip. The strength of the radiation pressure exerted on the back mirror

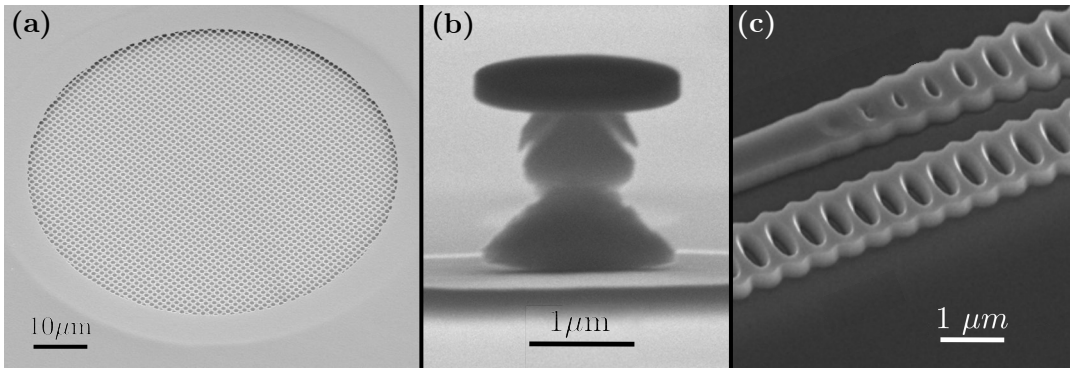

Figure 1.3: Examples of optomechanical systems. **(a)**. GaAs photonic crystal patterned micro-membrane. The figure shows the type of membranes studied in this thesis. **(b)** GaAs micro-disc resting on a pillar serving as an optomechanical resonator. Optical and mechanical modes are co-localized within the disc and interact through radiation pressure. Figure taken from [8]. **(b)**. Lithium niobate (LN) optomechanical crystal. As for the microdisc, the structure co-localizes mechanical and optical fields that interact within the structure. Figure taken from [9].

is thus increased proportionally to the number of round trips that are allowed for each photon before it is lost to scattering, absorption, or transmission. The movement of the back mirror introduces another interesting interaction between light and matter. When the back mirror is displaced, the resonance frequency is shifted which reduces the intracavity intensity. Thus, a natural coupling between light and mechanical motion is realized, which results in interesting static and dynamic phenomena [6]. The mentioned effects could, for example, be used to cool mechanical resonators down to their quantum ground state of motion [7].

The field of cavity optomechanics has seen a lot of activity since the first study of the optomechanical interaction with a macroscopic mirror in 1983 [10]. In general, the work is centered around performing studies of fundamental physical phenomena, such as observing macroscopic mechanical quantum states or investigating novel sensing applications. To achieve this, different types of highly isolated optomechanical systems which favor strong light-matter interaction are investigated. Advances in microfabrication techniques in the 21st century have allowed for the realization of precise micromechanical systems with promising optomechanical capabilities.

Figure 1.3 shows three types of realizations that are, among many others, used to study cavity optomechanics. Panel **(a)** displays a micromechanical mirror which can serve as the back mirror of an optical cavity, similar to the system presented in Figure 1.2. This type of system has been investigated by several groups in the late 2000s and has been used to demonstrate optomechanical cooling [11], [12]. Panel **(b)** shows a micrometer-scale optomechanical resonator in which breathing mechanical modes in the micro-disc

are coupled to a whispering gallery mode of the electromagnetic field. The coupling can be understood by noting that light circulating in the disc exerts radiation pressure against the resonator inner walls, pushing it outwards. Deformations in the disc increase the effective length of the resonator which mediates the mutual light-matter interaction. Micro-resonators have the advantages of high mechanical frequencies which allows for sideband-resolved optomechanics as well as design solutions to minimize clamping losses [8], [13]. Another realization is the optomechanical crystal (OMC) which trap optical and mechanical energy into highly confined regions of space. A lithium niobate OMC is shown in panel **(c)** of Figure 1.3. Silicon OMC's has been used to cool nanomechanical breathing motion to the quantum ground state [7]. The design also allows for interesting photonic-phononic circuitry applications such as bidirectional optical to microwave photon transduction which is crucial for quantum information technology [9], [14].

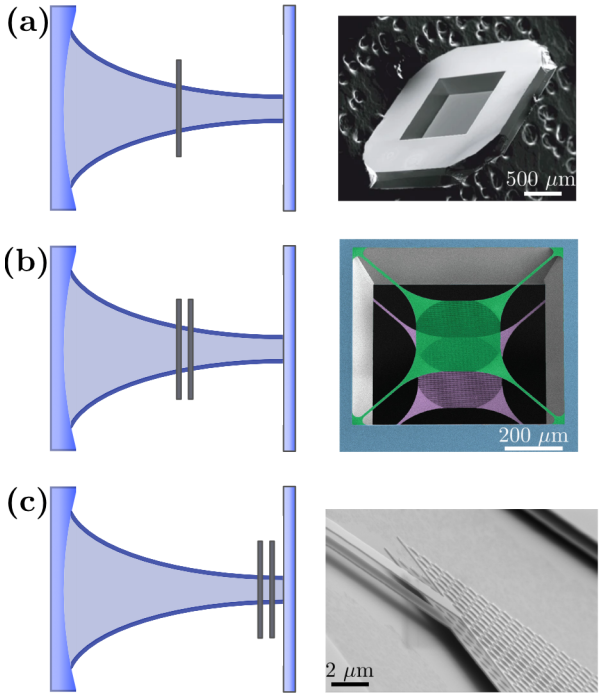

Figure 1.4: Comparison of different optomechanical systems utilizing micromechanical membranes. **(a)** SiN membrane utilized in a membrane in the middle (MIM) setup. Figure taken from [15] **(b)**. Two SiN membrane deposited on each side of a silicon wafer designed for multi-element MIM optomechanics. Photonic crystal patterns increases membrane reflectivity for a given wavelength. Figure taken from [16] **(c)**. Double-layer GaAs membrane grown using molecular beam epitaxy (MBE) on a distributed Bragg reflector (DBR) mirror forming a multi-element membrane at the edge system. This geometry is studied in our group and allows for integrated on-chip optomechanics devices.

Within the micromechanical membrane geometry, several works have investigated systems

where the resonator is placed in the middle of an optical cavity leading to a dispersive optomechanical coupling. This was demonstrated by Thompson *et al.* in 2008 and offers a way to perform quantum non-demolishing measurements of mechanical resonator phonon numbers [15], see panel **(a)** of Figure 1.4. In addition, theoretical work by Xuereb *et al.* in 2012 suggests that a stack of identical mechanical resonators placed within a high finesse optical cavity has the potential to increase the optomechanical coupling strength by several orders of magnitude [17]. This is of great interest since systems where the coupling strength exceeds losses to the environment enter the realm of single-photon strong coupling. This regime allows for the study of interesting single-photon statistics as well as quantum states of motion for micromechanical systems [6].

1.2.1 Multi-element cavity optomechanics with GaAs membranes

With the promise of reaching strong optomechanical coupling strengths with multi-element mechanical resonator stacks, several groups have investigated the phenomenon in recent years. In 2018, two different works centered around double-layer mechanical resonators were published. Piergentili *et al.* reported on two SiN membranes with tuneable separation in a macroscopic cavity for which they demonstrated an increase in optomechanical coupling strength by a factor of 2.47 compared to the single-layer case [18]. A crucial challenge with their system is the fact that two individual chips of SiN are glued together to form the stack. This introduces an unwanted degree of freedom in mutual membrane tilt. In addition, the reflectivity of the dielectric slabs is not high enough to create high coupling strengths for multi-element stacks [19]. A solution to both of these problems was presented by Gärtner *et al.* in the same year [16]. In their work, SiN membranes deposited on either side of a 200 μm thick Si wafer were used in a membrane in the middle optomechanical setup, see panel **(b)** of Figure 1.4. The membranes were suspended by removing the silicon between the membranes by wet etching from both sides of the chip. The reflectivity of the membranes was increased by perforating the membranes with a lattice of holes which forms a photonic crystal. The crystal defines a photonic bandgap that restricts the transmission of a certain wavelength effectively increasing the membrane reflectivity. Similar to the work of Piergentili, an increase in optomechanical coupling strength to the center of mass motion of a factor of 1.3 was demonstrated. However, the coupling to the relative motion of the membranes was predicted to be increased by 120.

The aforementioned attempts at creating Membrane In the Middle (MIM) optomechanical geometries with SiN membranes show that larger coupling between the electromagnetic field and the center of mass and relative motion of a membrane stack is possible. However, to reach even higher optomechanical couplings, the gap between the membranes in the multi-element stack requires fine-tuning in the nanometer range. To achieve this, semiconductor heterostructures grown using Molecular Beam Epitaxy (MBE) can be utilized which allow for precision growth of device and sacrificial layers. This is however not compatible with SiN's non-crystalline structure that doesn't allow for MBE growth

of consecutive layers. A solution to this problem, proposed by our group, is to use the crystalline material GaAs for the membranes which can be grown by MBE. Additional layers of AlGaAs can be added in between membranes which in turn are etched away with hydrofluoric acid [20].

In this work, I present the characterization of an optomechanical system utilizing GaAs membranes grown on top of a Distributed Bragg Reflector (DBR) forming a membrane at the edge geometry, see panel **(c)** of Figure 1.4. This system uses the power of MBE-grown heterostructures which has the potential to form a fully integrated on-chip optomechanical system with the potential to reach high optomechanical coupling strengths.

1.3 Thesis organization

The work of this thesis is focused to developing a platform for optomechanical characterization of single- and double-layer micromechanical resonators. The structure of the thesis aims to introduce the relevant concepts, both theoretical and experimental, that are used here to investigate and analyze the optomechanical system. The chapters divide the thesis into manageable pieces and are organized as follows:

Chapter 2. aims to make the reader familiar with the system under study by first introducing the basics description of the optical and mechanical degrees of freedom which together make up the optomechanical system. With understanding of the ingoing subsystems, the optomechanical Hamiltonian is derived, and some system dynamics is explored in terms of optomechanical damping and optical spring effect.

Chapter 3. presents the experimental techniques and setups used during the production of this thesis. The techniques discussed are Pound-Drever-Hall cavity frequency locking and homodyne detection which enables sensitive readout of micromechanical motion. These techniques are implemented in the optomechanical readout setup that was developed during this work.

Chapter 4. covers the results of the thesis, categorized in three main parts. First, the optical and mechanical properties of the micromechanical membranes are presented. Secondly, the properties of optical cavities with integrated mechanical resonators are investigated. Lastly, the performance of the optomechanical readout setup is discussed.

Chapter 5. contains the conclusion of the thesis, which summarizes the presented work and discusses the outlooks for the future of this project.

2. Theory

In this chapter, the basic theory needed for understanding this thesis is presented. I begin by introducing the optomechanical system which is studied in this work. To this end, both the optical and mechanical subsystems are described, after which I introduce the optomechanical Hamiltonian. Next, the concept of how the optomechanical interaction can be increased through means of multi-element mechanical resonators is described. Finally, I discuss the concept of using photonic crystals to increase the reflectivity of the mechanical resonator. High membrane reflectivity is one requirement for reaching strong light-matter interaction within the multi-element optomechanics framework.

2.1 Mechanical resonator

The harmonic oscillator is a fundamental physical concept with widely applicable modelling capabilities, describing phenomena ranging from thermal baths to the electromagnetic field. In this work, we will use it to model both the optical and mechanical subsystems. Starting with the mechanical resonator, an introduction to the classical and quantum setting is given.

2.1.1 Classical description

The one-dimensional mechanical resonator in its simplest form is described by a point mass m attached to a spring with force constant k, viscous damping Γ_m and time dependent external force $F_\mathrm{ext}(t)$. The resonance frequency of this system is defined by the mass and force constant alone and is given by $\Omega_\mathrm{m} = \sqrt{k/m}$. Another figure of merit is the quality

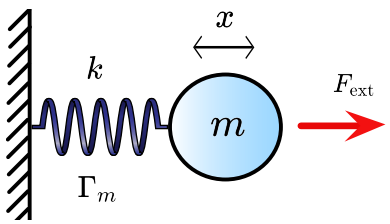

Figure 2.1: The classical mechanical resonator described by a point mass m attatched to a spring with force constant k. The motion x is damped with viscous damping Γ_m and driven by the external force F_ext.

factor Q_m of the mechanical mode, given by

$$Q_\mathrm{m} = \frac{\Omega_\mathrm{m}}{\Gamma_\mathrm{m}} \tag{2.1}$$

which is a measure of the energy loss of the system. It is roughly corresponding to the number of coherent oscillations performed by the system during the ringdown motion after excitation by a delta pulse.

For this system, Newton's equation of motion for the time dependent position $x(t)$ of the point mass reads

$$\frac{\mathrm{d}^2x(t)}{\mathrm{d}t^2} + \Gamma_\mathrm{m}\frac{\mathrm{d}x(t)}{\mathrm{d}t} + \Omega_\mathrm{m}^2 x(t) = \frac{F_\mathrm{ext}(t)}{m}\,. \tag{2.2}$$

To explain the frequency response of the mechanical motion with respect to the external force F_ext we perform a Fourier transform of (2.2) defined by $\tilde{x}(\omega) = \int_{-\infty}^{\infty} x(t)\exp\{-\mathrm{i}\omega t\}\mathrm{d}t$. Solving the equation for $\tilde{x}(\omega)$ gives

$$\tilde{x}(\omega) = \tilde{F}_\mathrm{ext}(\omega)\chi(\omega) \tag{2.3}$$

where $\chi(\omega)$ is the linear response or susceptibility of the mechanical motion with respect to the force $F_\mathrm{ext}(t)$ and reads

$$\chi(\omega) = \frac{1}{m(\Omega_\mathrm{m}^2 - \omega^2 + \mathrm{i}\Gamma_\mathrm{m}\omega)}\,. \tag{2.4}$$

The susceptibility is a complex valued quantity with real and imaginary parts corresponding to the system phase response to the external force. The real part is the in-phase response, whilst the imaginary part describes the response which is $\pi/2$ out-of-phase with the applied force [21]. By ergodicity, taking the square average of (2.3) over an ensemble of trajectories $x(t)$ with different initial conditions gives the *power spectrum* of the mechanical motion describing the mechanical energy distribution as a function of frequency,

$$S_{xx}(\omega) = \langle\tilde{x}(\omega)\tilde{x}^*(\omega)\rangle = \frac{\left|\tilde{F}_\mathrm{ext}(\omega)\right|^2}{m^2((\Omega_\mathrm{m}^2 - \omega^2)^2 + \Gamma_\mathrm{m}^2\omega^2)}\,. \tag{2.5}$$

This quantity is crucial when analyzing mechanical motion, telling us what frequency components are present for a given dynamical system.

Consider a special case of the above system in which a mechanical resonator is in thermal equilibrium with an external environment of temperature T and is not subject to any additional external forces. The coupling to the environment will induce a stochastic flow of energy between the resonator and the external thermal bath. This stochastic process can be modeled by letting the resonator be subject to viscous damping Γ_th and time dependent stochastic force $F_\mathrm{th}(t)$ [22]. The equation of motion thus becomes

$$\ddot{x}(t) + \Gamma_\mathrm{th}\dot{x}(t) + \Omega_\mathrm{m}^2 x(t) = \frac{F_\mathrm{th}(t)}{m}\,, \tag{2.6}$$

which has the same form as (2.2). The stochastic nature of the thermally induced parameters $\Gamma_{\rm th}$ and $F_{\rm th}$ makes this problem similar to that of a particle experiencing thermal Brownian motion, the difference here being the additional spring force term $\Omega_{\rm m}^2 x(t)$ anchoring the motion to the origin. To see how the thermal bath interacts with the mechanical motion we make use of the expressions derived above along with results from statistical physics.

Firstly, the fluctuation dissipation theorem states that [21]

$$\mathrm{Im}[\chi(\omega)] = \frac{\omega}{2k_B T} C_{xx}(\omega)\,. \tag{2.7}$$

which links the imaginary part of the susceptibility to the Fourier transform of the equal time correlation function

$$C_{xx}(\omega) = \int_{-\infty}^{\infty} \langle x(\tau)x(0)\rangle \exp\{i\omega\tau\}\mathrm{d}\tau\,. \tag{2.8}$$

Next, for a stationary stochastic process $x(t)$ [1], the Wiener-Khinchin theorem gives that

$$S_{xx}(\omega) = C_{xx}(\omega). \tag{2.9}$$

Finally, we make use of (2.4) and (2.5) in conjunction with (2.7) to get an expression for the Fourier transform of the thermal force

$$\left|F_{\rm th}(\omega)\right|^2 = 2k_B T \Gamma_{\rm th} m\,, \tag{2.10}$$

telling us that the bath interaction is independent of frequency[2].

We can now approximate the power spectrum (2.5) by noting that around the mechanical frequency $\omega \sim \Omega_{\rm m}$ we can write $\Omega_{\rm m}^2 - \omega^2 = (\Omega_{\rm m} - \omega)(\Omega_{\rm m} + \omega) \approx 2\Omega_{\rm m}(\Omega_{\rm m} - \omega)$, yielding a simplified form of the power spectrum is given as

$$S_{xx}(\omega) \approx \frac{k_B T}{2m\Omega_{\rm m}^2} \frac{\Gamma_{\rm th}}{(\omega - \Omega_{\rm m})^2 + (\Gamma_{\rm th}/2)^2}\,. \tag{2.11}$$

The above expression states that the power spectrum of the mechanical motion in thermal equilibrium can be approximated as a Lorentzian at the resonance frequency $\Omega_{\rm m}$ with Full Width Half Maximum (FWHM) given by the mechanical damping $\Gamma_{\rm th}$. We emphasize that the above describes a resonator with only one resonant mode $\Omega_{\rm m}$. However, it is also valid for a system with an arbitrary number of uncoupled modes given that $\Gamma_{\rm th} \ll \Delta\Omega$ where $\Delta\Omega$ is the smallest frequency spacing between individual oscillating modes.

From this analysis, another important result can be derived. By inverting the Fourier transform in (2.9), and setting $\tau = 0$ we see that

$$\langle x^2 \rangle = \int_{-\infty}^{\infty} S_{xx}(\omega) \frac{\mathrm{d}\omega}{2\pi}\,, \tag{2.12}$$

[1] A stationary stochastic process $x(t)$ has time independent mean and second order moment [23].

[2] The white noise nature of the thermal force originates from the Markovianity of the bath dynamics $\langle F(t-\tau)F(t)\rangle \propto \delta(\tau)$.

which states that the mean square value of the mechanical displacement can be obtained by integration of the power spectrum. This is a powerful result which allows to study the average mean displacement of a mechanical oscillation by observing its frequency response. Solving this integral for the power spectrum (2.5) with thermal interaction gives [24]

$$\langle x^2 \rangle = \frac{k_B T}{m\Omega_{\mathrm{m}}^2}, \tag{2.13}$$

which is what we would expect when assuming equipartition for a mechanical resonator coupled to a thermal bath at temperature T.

2.1.2 Quantum description

To describe the quantum mechanical nature of a mechanical resonator, one starts by deriving its Hamiltonian. We consider a single, undamped, harmonic oscillating mode with mass m described by the position x and momentum p, oscillating at frequency Ω_{m}. The energy of the system is given by

$$H_{\mathrm{m}} = \frac{1}{2} m\Omega_{\mathrm{m}}^2 x^2 + \frac{p^2}{2m}\,. \tag{2.14}$$

We now continue by promoting the coordinates to quantum mechanical operators $x \to \hat{x}$, $p \to \hat{p}$ and invoke the canonical commutator relation

$$[\hat{x}, \hat{p}] = \mathrm{i}\hbar\,. \tag{2.15}$$

To find the eigenstates to this Hamiltonian we insert it into the Schrödinger equation

$$i\hbar \frac{\mathrm{d}\,|\psi\rangle}{\mathrm{d}t} = \hat{H}_{\mathrm{m}}\,|\psi\rangle\,, \tag{2.16}$$

which is most conveniently solved by introducing bosonic creation and annihilation operators

$$\begin{aligned} \hat{b}^\dagger &= \frac{1}{2x_{\mathrm{ZPF}}}\left(\hat{x} + \frac{\mathrm{i}}{m\Omega_{\mathrm{m}}}\hat{p}\right), \\ \hat{b} &= \frac{1}{2x_{\mathrm{ZPF}}}\left(\hat{x} - \frac{\mathrm{i}}{m\Omega_{\mathrm{m}}}\hat{p}\right), \\ [\hat{b}, \hat{b}^\dagger] &= 1\,, \end{aligned} \tag{2.17}$$

where x_{ZPF} is the zero-point fluctuation given by

$$x_{\mathrm{ZPF}} = \sqrt{\frac{\hbar}{2m\Omega_{\mathrm{m}}}}. \tag{2.18}$$

In this coordinate system we express the harmonic oscillator Hamiltonian as

$$\hat{H}_{\mathrm{m}} = \hbar\Omega_{\mathrm{m}}\left(\hat{b}^\dagger\hat{b} + \frac{1}{2}\right), \tag{2.19}$$

where the operator $\hat{b}^\dagger\hat{b} = \hat{n}_b$ is the number operator for the quanta of oscillation in the harmonic mode, also known as phonons. From (2.19) it is apparent that the energy

eigenstates are simultaneous eigenstates of the number operator which indicates that the number of phonons is a measure for the energy in an oscillating mode. Solving (2.16) in the position basis gives a set of eigenstates obeying $\hat{H}_{\mathrm{m}} |\psi_n\rangle = E_n |\psi_n\rangle$ with eigenenergies E_n given by the creation operator [25]

$$\begin{aligned} |\psi_n\rangle &= (\hat{b}^\dagger)^n |\psi_0\rangle \,, \\ \langle x|\psi_0\rangle &= \frac{1}{(2\pi)^{1/4}\sqrt{x_{\mathrm{ZPF}}}} \exp\left[-\frac{1}{4}\left(\frac{x}{x_{\mathrm{ZPF}}}\right)^2\right], \\ E_n &= \hbar\omega\left(n+\frac{1}{2}\right). \end{aligned} \tag{2.20}$$

From the second line in (2.20) we see that x_{ZPF} defines the spatial extension of the quantum mechanical ground state of the oscillator. Note that in this description we have considered an isolated harmonic oscillator mode which does not interact with its environment. To introduce a coupling to an environment one can, for instance, couple the system to an ensemble of harmonic oscillators which is further explored in works such as [22].

2.2 Optical cavity

The second subsystem we look at is the electromagnetic field, which interacts with the mechanics through radiation pressure. As discussed in Section 1.1, the radiation pressure is usually omitted due to the small magnitude of the force. To increase the magnitude of this interaction, we will make use of a *Fabry-Pérot* (FP) cavity which enhances the strength of the electromagnetic field, from now on referred to as the optical field even though microwaves can be utilized in optomechanical systems as well [26].

2.2.1 Classical description

We begin the classical analysis by considering two identical and perfectly reflecting mirrors of negligible thickness that are facing each other at a distance L. The material in between the mirrors is assumed to be homogeneous and is taken to be vacuum for simplicity. It is assumed that the optical field inside the cavity is monochromatic and linearly polarized, thus taking the form

$$E(\mathbf{r}, t) = A(\mathbf{r})\mathrm{e}^{i\omega t} \,, \tag{2.21}$$

where $A(\mathbf{r})$ is the amplitude and ω is the single angular frequency of the light. Restricting our analysis to one dimension, the cavity of length L defines the boundary conditions for the electrical field E inside the cavity. With these assumptions, Maxwell's equations for the electric field (2.21) inside the cavity are simplified to a stationary Helmholtz equation for the amplitude

$$\frac{\partial^2}{\partial x^2}A(x) + k^2 A(x) = 0 \,, \quad \begin{cases} A(0) = 0 \\ A(L) = 0 \end{cases} \tag{2.22}$$

with $k = \omega/c$. Given that $kL = \pi n$, where n is an integer, the solution describes a linear combination of standing waves inside the cavity

$$A(x) = \sum_n A_n \sin\left(\frac{n\pi x}{L}\right), \quad x \in [0, L] \text{ and } n = 1, 2, \dots, \tag{2.23}$$

with harmonic amplitudes A_n. This is equivalent to the classical "particle in a box" example. The three first standing wave solutions are visualized in Figure 2.2.

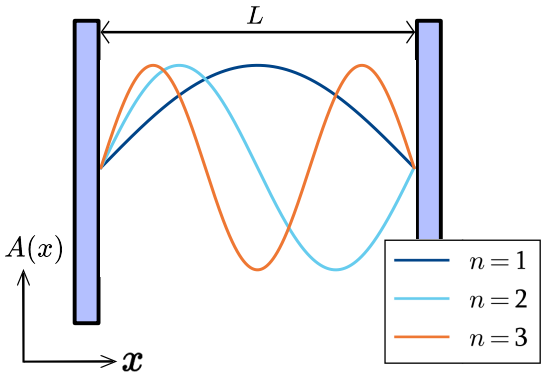

Figure 2.2: The stationary solutions to the perfectly reflecting mirror cavity presented in (2.23) are electrical field amplitudes with fixed frequencies $\omega_{\text{cav}} = \pi cn/L$, $n = 1, 2, \dots$. The first three harmonics are shown above.

The cavity thus acts as a spectral filter supporting only the harmonics of the resonant frequency given by

$$\omega_{\text{cav}} = \pi cn/L\,. \tag{2.24}$$

The spectral spacing between two adjacent cavity harmonics is called the Free Spectral Range (FSR) and is given by $\text{FSR} = c/2L$.

In all realistic cases the cavity mirrors will not be perfectly reflecting, thus also having a finite transmission $T \neq 0$ and other intrinsic losses, *e.g.*, scattering and absorption. The losses are modelled by the parameter β, which is defined as an attenuation per unit length of propagation within the cavity. Because of the finite transmission it is possible to insert power into the cavity with an external light source and thus populate the intracavity field.

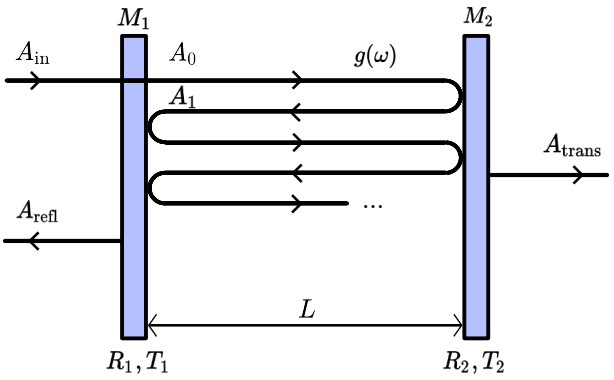

Figure 2.3: Optical cavity with imperfectly reflecting mirrors M_1 and M_2. The field A_{in} is incident on the cavity and populates the intracavity amplitudes A_i with $i = 0, 1, \ldots$. The leakage of the intracavity field contributes to the reflected (transmitted) amplitude A_{refl} (A_{trans}).

Consider the system presented in Figure 2.3. An incident light field of amplitude A_{in} and angular frequency ω impinges on the left side of a cavity with mirrors M_1 and M_2. The intensity reflection and transmission coefficients of the mirrors are assumed to be R_i, T_i, respectively for $i = 1, 2$. The amplitude of the transmitted field into the cavity is defined by the transmission coefficient of M_1 and is given by $A_0 = \sqrt{T_1} A_{\text{in}}$. Now, the field inside the cavity will start to circulate between the two cavity mirrors and be attenuated by subsequent transmissions through the cavity mirrors. The following derivation closely follows that of [27] where it is shown that for each roundtrip i of the cavity, the amplitude of the field is multiplied by a roundtrip factor $g(\omega)$:

$$\begin{aligned} A_i &= A_{i-1} g(\omega)\,, \\ g(\omega) &= g_{\text{m}} \mathrm{e}^{-\mathrm{i}\delta\phi(\omega)}\,, \\ g_{\text{m}} &= \sqrt{R_1 R_2 \mathrm{e}^{-L\beta}}\,. \end{aligned} \tag{2.25}$$

The roundtrip factor $g(\omega)$ accounts for the amplitude attenuation via transmission and internal losses through the factor g_{m} and the cavity roundtrip phase difference through $\delta\phi(\omega) = (\omega - \omega_{\text{cav}})2L/c$. The total amplitude inside the cavity is the sum of the roundtrip amplitudes which can be evaluated as a geometric series:

$$A_{\text{cav}} = \sum_{i=0}^{\infty} A_i = A_0 \sum_{i=0}^{\infty} g(\omega)^i = \frac{A_0}{1 - g(\omega)}\,, \quad |g(\omega)| < 1\,. \tag{2.26}$$

The intensity of the field is given by the square of the amplitude

$$I_{\text{cav}} = |A_{\text{cav}}|^2 = \frac{T_1 |A_{\text{in}}|^2}{(1 - g_{\text{m}})^2} \frac{1}{1 + (2\mathcal{F}/\pi)^2 \sin^2(\delta\phi/2)}\,, \tag{2.27}$$

where $\mathcal{F}$ is the finesse of the cavity and is given by

$$\mathcal{F} = \frac{\pi\sqrt{g_{\text{m}}}}{1 - g_{\text{m}}}\,. \tag{2.28}$$

Considering equation (2.27) some important observations can be made. Firstly, at frequencies $\omega \sim \omega_{\text{cav}}$ the roundtrip phase difference is small *i.e.*, $|\delta\phi| \ll 1$, and we can expand the second factor on the right hand side using a small angle approximation. This gives the intracavity field intensity as a Lorentzian in frequency space centered around $\omega = \omega_{\text{cav}}$,

$$I_{\text{cav}} \approx \frac{T_1 |A_{\text{in}}|^2}{(1-g_{\text{m}})^2} \frac{(\kappa/2)^2}{(\omega-\omega_{\text{cav}})^2 + (\kappa/2)^2} \,. \tag{2.29}$$

The parameter κ is the FWHM of the Lorenzian, often referred to as the cavity linewidth, and is given by

$$\frac{\kappa}{2\pi} = \frac{c}{2L\mathcal{F}} = \frac{\text{FSR}}{\mathcal{F}}. \tag{2.30}$$

This means that the intracavity field does not vanish for nonzero cavity detunings, *i.e.* $\Delta = \omega - \omega_{\text{cav}} \neq 0$. The allowed frequency range is centered around $\omega = \omega_{\text{cav}}$ with a width defined by the cavity finesse $\mathcal{F}$. Secondly, the intensity of the field at resonance ($\Delta = 0$) is proportional to the incident intensity $I_{\text{in}} = |A_{\text{in}}|^2$ and approaches infinity when $g_{\text{m}} \to 1$, allowing us to create strong intracavity fields with carefully chosen mirrors.

Turning our attention to the cavity reflection and transmission, the relevant amplitudes are given by

$$\begin{aligned} A_{\text{refl}} &= -\sqrt{R_1} A_{\text{in}} + \sqrt{T_1 R_2} \mathrm{e}^{-2L\beta + \mathrm{i}\delta\phi} A_{\text{cav}}, \\ A_{\text{trans}} &= \sqrt{T_2} \mathrm{e}^{-L\beta + \mathrm{i}\delta\phi/2} A_{\text{cav}}. \end{aligned} \tag{2.31}$$

By inserting the intracavity amplitude (2.26) and normalizing to the incident intensity we get the following relations

$$\begin{aligned} \frac{I_{\text{refl}}}{I_{\text{in}}} &= \frac{\left|R_1 - g(\omega)\right|^2}{R_1 \left|1 - g(\omega)\right|^2} \,, \\ \frac{I_{\text{trans}}}{I_{\text{in}}} &= \frac{T_1 T_2 \left|g(\omega)\right|^2}{R_1 R_2 \left|1 - g(\omega)\right|^2} \,. \end{aligned} \tag{2.32}$$

For the special case of a lossless symmetric cavity ($R_1 = R_2$, $T_1 = T_2$, $\beta = 0$) excited by a resonant incident field we obtain $g(\omega) \to R\mathrm{e}^{-i\delta\phi(\omega)}$. For this case, we can again invoke a small angle approximation for the relative cavity reflection when $\omega \sim \omega_{\text{cav}}$ giving

$$\frac{I_{\text{refl}}}{I_{\text{in}}} \approx 1 - \frac{(\kappa/2)^2}{(\omega-\omega_{\text{cav}})^2 + (\kappa/2)^2} \,, \tag{2.33}$$

which is a useful result when analyzing cavity reflections. Additionally, we see that at resonance, *i.e.* $\omega = \omega_{\text{cav}}$, the lossless symmetric case gives $I_{\text{refl}}/I_{\text{in}} = 0$ and $I_{\text{trans}}/I_{\text{in}} = 1$. For arbitrary $R < 1$ the highly reflective cavity is therefore totally transparent to the incoming light due to the reflection destructively interfering with the back-transmission of the intracavity field. If the cavity is not symmetric, there is an impedance mismatch between the mirrors which decreases the cavity resonance. In Figure 2.4 the cavity reflection is calculated over two full FSRs at different impedance mismatches.

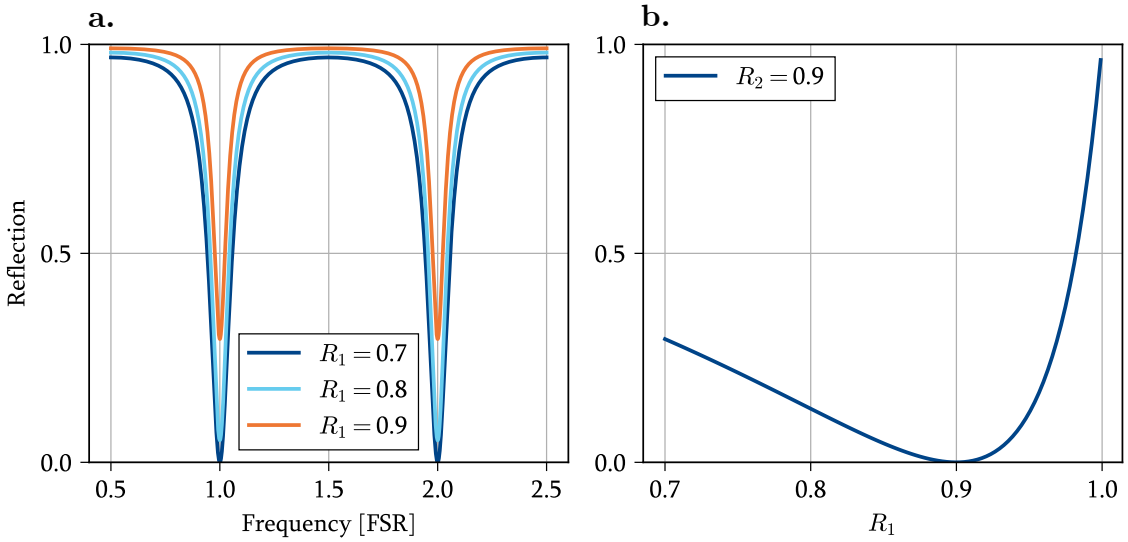

Figure 2.4: **a.** Cavity reflection spectra at different levels of impedance mismatch. For all traces $R_2 = 0.7$. For $R_1 = R_2$ the symmetrical case is achieved and the reflection vanishes for the resonant wavelengths. Note that the reflection spectra retains its Lorentzian shape for non-zero impedance mismatches. **b.** Magnitude of cavity resonance *e.g.*, reflection spectrum minimum as a function R_1 for fixed $R_2 = 0.9$. Impedance mismatch is more severe for higher reflecting mirrors.

2.2.2 Fabry-Pérot cavity architecture

We have seen that the FP optical cavity is comprised of two flat mirrors facing each other at distance L. In practice, this configuration is not desirable due to the strict alignment conditions required to prevent intracavity light leakage. To confine the optical field inside the cavity, spherical mirrors are used to trap the light. Important to note is that spherical mirrors can be modeled as perfect lenses with focal distance $f = r/2$ where r is the radius of curvature of the mirror, see Figure 2.5. This means that a cavity can be modeled as an infinite series of lenses which guides a certain spatial mode of light.

Having stationary ray paths inside the cavity using spherical mirrors puts restrictions on the length of the cavity. A cavity, with mirror distance L and radii of curvature r_1 and r_2, in which all light paths are closed loops is called stable and obeys the following condition [28]

$$0 \leq \left(1 - \frac{L}{r_1}\right)\left(1 - \frac{L}{r_2}\right) \leq 1\,. \tag{2.34}$$

Special cases of stable cavities include

$$\begin{aligned} &\text{Concentric:} && r_1 = r_2 = L/2 \\ &\text{Confocal:} && r_1 = r_2 = L \\ &\text{Hemispheric:} && r_1 = \infty,\ r_2 = L\,. \end{aligned} \tag{2.35}$$

In this work a hemispheric cavity is used and we will thus turn our focus to this special

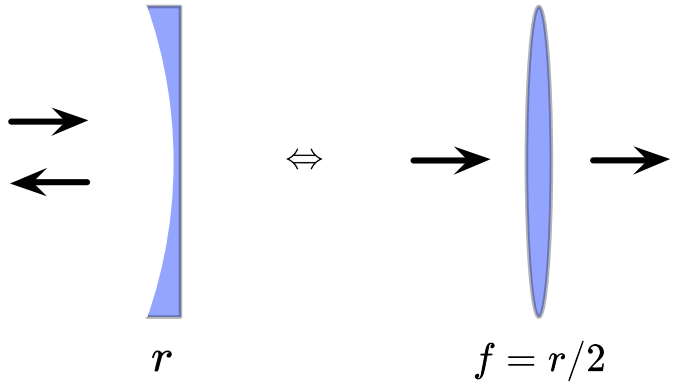

Figure 2.5: A spherical mirror with radius of curvature r focuses incoming light equivalently to a spherical lens with focal distance $f = r/2$.

case of the FP cavity. When $L \to r_2$ a perfect focus on the flat mirror is maintained by the curved mirror due to the focus being at a distance $2f$ from the focusing element, where f is the effective focal distance of M_2. Of course, there is no perfect focus in practice and it can be shown that the beam radius w for the focus on the flat mirror of a hemispheric cavity satisfies [24]

$$w^2 = \frac{L\lambda}{\pi}\sqrt{\frac{r_2}{L} - 1}\,. \tag{2.36}$$

2.2.3 Cavity spatial modes

The waist radius w is the radial distance from the optical axis where the light intensity has decayed by a factor of e^{-2}. This is a parameter which describes the Gaussian nature of propagating light rays. The electrical field of a Gaussian ray propagating in the z-direction can be described by [27]

$$E(x,y,z) = E_0 \frac{w_0}{w(z)} \exp\left\{-\frac{x^2+y^2}{w(z)^2}\right\} \exp\left\{-ikz - ik\frac{x^2+y^2}{2R(z)} + i\zeta(z)\right\}, \tag{2.37}$$

where w_0 is the beam radius at position $z = 0$, $w(z) = w_0\sqrt{1+(z/z_r)^2}$ with Rayleigh range $z_r = \pi w_0^2/\lambda$, $R(z) = z(1+(z/z_r)^2)$ is the radius of curvature of the propagating wavefront, k is the wavenumber of the light. $\zeta(z) = -\arctan(z/z_r)$ is the so called Gouy phase which is a phase shift that accounts for the transverse confinement of the optical mode. This is the fundamental spatial distribution of light field intensity and is the most common output of single mode lasers and optical fibers. When the light field is not strictly described by the precise transverse spatial distribution stated above it is called a multimode field and it can be described by a linear combination of spatially orthogonal optical modes. These optical modes arise from solving the paraxial wave equation in the x, y-plane with defined boundary conditions [27]. A specific set of solutions is the so called

Hermite-Gauss set

$$E_{l,m}(x,y,z) = E_0 A_{l,m} \frac{w_0}{w(z)} H_l\left(\frac{\sqrt{2}x}{w(z)}\right) H_m\left(\frac{\sqrt{2}y}{w(z)}\right) \exp\left\{-\frac{x^2+y^2}{w(z)^2}\right\} \times \\ \exp\left\{-ikz - ik\frac{x^2+y^2}{2R(z)} + i\zeta_{l,m}(z)\right\},\ l,m = 0,1,2\ldots . \tag{2.38}$$

In this equation $H_l(x) = (-1)^l \exp\left(x^2\right) \frac{\mathrm{d}^l}{\mathrm{d}x^l} \exp\left(-x^2\right)$ are the Hermite polynomials and $A_{l,m}$ are normalization constants. The Gouy phase is also dependent on the spatial mode and is given by [29]

$$\zeta_{l,m}(z) = -(2+l+m)\arctan z/z_R\,. \tag{2.39}$$

In Section 2.2.1 we have seen that the resonant condition of an optical cavity is that the roundtrip phase difference $\delta\phi(\omega)$ mod $2\pi = 0$. Now, looking at the phase of an Hermite-Gauss mode at the optical axis $(x, y = 0)$ that is allowed to propagate within one cavity roundtrip we get the condition for the resonance frequency

$$\begin{aligned} \delta\phi_{l,m} &= 2Lk - (\zeta_{l,m}(0) - \zeta_{l,m}(2L)) \\ &= \frac{2\omega_{l,m}L}{c} - \Delta\zeta_{l,m} = 2\pi n \\ &\Leftrightarrow \\ \omega_{l,m} &= \omega_{\mathrm{cav}} + \mathrm{FSR}\Delta\zeta_{l,m}\,. \end{aligned} \tag{2.40}$$

Here $\Delta\zeta_{l,m} = \zeta_{l,m}(0) - \zeta_{l,m}(2L)$ and $\omega_{\mathrm{cav}} = cn\pi/L$ is the resonant frequency for a plane wave inside the cavity. From (2.40) we see that the spectral seperation between two spatial modes with Hermite-Gauss indices m, l and m', l' is defined by

$$\Delta\omega_{m,l}^{m',l'} = \mathrm{FSR}\left|\Delta\zeta_{l,m} - \Delta\zeta_{l',m'}\right|, \tag{2.41}$$

which originates from the difference in Gouy phase of the spatial modes. Another thing to note is that the separation is independent of frequency and will be same for all harmonics. This result is remarkable, not only does the cavity work as a spectral filter, allowing a band of frequencies around the resonance to pass through, but in the process also acts as a spatial filter by filtering out the resonant spatial mode. The phenomena is depicted in Figure 2.6 where the transmission spectrum of an FP cavity with an incident multimode field is shown. The amplitudes of the resonances is determined by the linear combination of spatial modes in the incident field. To access only the fundamental Gaussian mode, a perfect single mode field has to impinge with correct alignment and focusing which, in practice, is performed by aligning a single mode laser output with a set of lenses and mirrors. A measure of how well aligned the incident laser field is to a certain cavity mode is the ratio of its transmission to the sum of transmission in all modes present in one FSR.

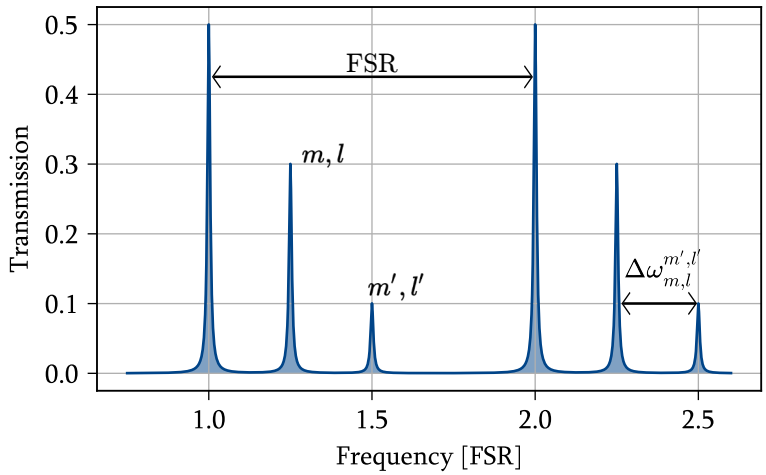

Figure 2.6: The intensity transmission spectrum of a FP cavity with an incident multimode field normalized to the incident intensity. Harmonics are separated by the FSR whereas the separation between spatial modes with Hermite-Gauss indices m, l and m', l' is defined by $\Delta\omega_{m,l}^{m',l'}$. The amplitude of the resonances is determined by the spatial composition of the incident field.

2.2.4 Quantum description

In Section 2.2.1, we introduced the optical cavity as a classical system with parameters such as resonance frequency ω_{cav} and linewidth κ. These parameters define the frequency behaviour of an excitation within the optical field, not unlike how we viewed the mechanical resonator in Section 2.1.1. The similarities between optical and mechanical resonances is a motivation for thinking of the electromagnetic field as a harmonic oscillator. In fact, it is not even necessary to consider a cavity to conclude that the electromagnetic field can be quantized as harmonic oscillator modes with frequencies given by the relevant geometry. The derivation showing how the electromagnetic field can be quantized is given in basic quantum mechanics textbooks such as [25] and starts from Maxwell's equations and ends up in a quantum mechanical Hamiltonian describing the energy in the electromagnetic field as

$$\hat{H}_{\text{em}} = \sum_{\mathbf{k},p} \hbar\omega_{\mathbf{k},p} \left(\hat{a}^{\dagger}_{\mathbf{k},p} \hat{a}_{\mathbf{k},p} + \frac{1}{2} \right), \tag{2.42}$$

where $\mathbf{k}$ and p is the wavenumber and polarization of the quantized modes with frequencies $\omega_{\mathbf{k},p}$ and bosonic operators $a_{\mathbf{k},p}$ and $a^{\dagger}_{\mathbf{k},p}$ obeying $[a_{\mathbf{k},p}, a^{\dagger}_{\mathbf{k}',p'}] = \delta_{\mathbf{k},\mathbf{k}'}\delta_{p,p'}$. As in the mechanical system described above the bosonic operators govern the quantized energy in the given mode, this time referring to photons. The number of photons in a given mode $\{\mathbf{k}, \mathbf{p}\}$ is given by the number operator $\hat{n}_{\mathbf{k},\mathbf{p}} = a^{\dagger}_{\mathbf{k},p} a_{\mathbf{k},p}$. As seen in the classical description, the consequence of an optical cavity is a restriction of the allowed optical modes within a geometry which will reduce the amount of terms in the sum of (2.42). Consider an optical cavity of high finesse which adequately separates the cavity harmonics in frequency space, allowing for approximating the modes as non-interacting. The energy in one of the

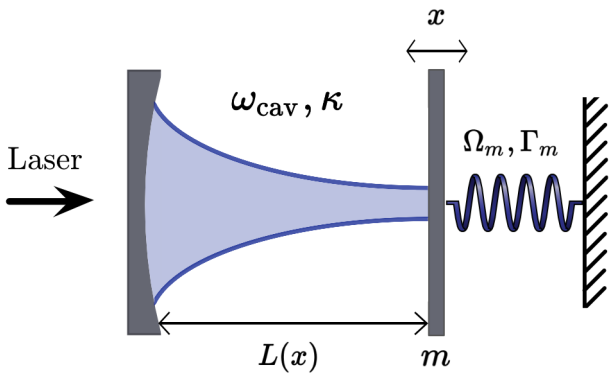

Figure 2.7: Canonical optomechanical system. A laser is shined on an optical cavity with resonance frequency ω_{cav} and loss κ which is connected to a mechanical resonator via the harmonic movement x of the back cavity mirror with frequency Ω_{m} and damping Γ_{m}.

resonances with frequency $\omega_{\mathrm{cav}} = c\pi/L$ can thus be reduced to

$$\hat{H}_{\mathrm{o}} = \hbar\omega_{\mathrm{cav}}\left(\hat{a}^{\dagger}\hat{a} + \frac{1}{2}\right), \tag{2.43}$$

which is the Hamiltonian we consider when exploring the dynamics of the optomechanical system in the coming sections.

2.3 Optomechanical coupling

In this section, we discuss the optomechanical interaction between a cavity mode and a mechanical resonator through radiation pressure. We begin by analyzing the energy of the coupled system and derive the optomechanical Hamiltonian. Using the Hamiltonian, the equations of motion for the coupled system are derived which allows for studying the consequences of the coupling such as optomechanical cooling. Lastly, the optomechanical system is expanded by introducing multi-element mechanical resonators, allowing for stronger light-matter interactions.

2.3.1 Optomechanical Hamiltonian

We start off by introducing the Hamiltonian which governs the dynamics of the coupled system. In this derivation we assume a single mechanical mode interacting with a single optical mode which is an accepted approximation for high quality mechanical and optical resonators. For now, we omit the coupling to the optical and mechanical environments which makes us consider a closed system. The system under study is the canonical optomechanical setup shown in Figure 2.7 where one of the end mirrors of an optical cavity is allowed to oscillate with frequency Ω_{m}. The length of the cavity now depends on the position of the back mirror x. We assume that L is the cavity length at the rest position

of the back mirror and thus have

$$L(x) = L + x\,, \tag{2.44}$$

where it is assumed that $|x|/L \ll 1$. Taking the first harmonic of (2.24) (n = 1), we have that a shift in the cavity length will cause a shift in cavity resonance frequency

$$\omega(x) = \frac{\pi c}{L(x)} = \frac{\pi c}{L+x} \approx \omega\left(1 - \frac{x}{L}\right)\,, \tag{2.45}$$

where $\omega = \pi c/L$ is taken as the unperturbed cavity frequency. We are now ready to formulate the basic optomechanical Hamiltonian by again promoting the position of the mirror to a quantum mechanical operator $x \to \hat{x}$. The Hamiltonian consists of the energy in the optical and mechanical systems given in (2.19) and (2.43)

$$\begin{aligned}\hat{H} = \hat{H}_{\mathrm{m}} + \hat{H}_o &= \hbar\Omega_{\mathrm{m}}\hat{b}^\dagger\hat{b} + \hbar\omega(\hat{x})\hat{a}^\dagger\hat{a} \\ &\approx \hbar\Omega_{\mathrm{m}}\hat{b}^\dagger\hat{b} + \hbar\omega\hat{a}^\dagger\hat{a} - \hbar\frac{\omega}{L}\hat{x}\hat{a}^\dagger\hat{a}\,,\end{aligned} \tag{2.46}$$

where we use (2.45) and omit vacuum fluctuations. In this Hamiltonian the last term describes the nonlinear interaction between the two modes. From (2.17) we have that $\hat{x} = x_{\mathrm{ZPF}}(\hat{b} + \hat{b}^\dagger)$ which gives the interaction term the following form

$$\hat{H}_{\mathrm{int}} = -\hbar g_0(\hat{b} + \hat{b}^\dagger)\hat{a}^\dagger\hat{a}\,. \tag{2.47}$$

In this expression, g_0 is the single photon-phonon coupling given in frequency units as

$$g_0 = \frac{\omega}{L}x_{\mathrm{ZPF}}\,. \tag{2.48}$$

This coupling is a crucial quantity which describes the cavity frequency shift corresponding to one zero point displacement of the mechanical resonator. When looking at parameters relevant for the systems described in this thesis, *i.e.* $\Omega_{\mathrm{m}} \sim 100$ kHz, $L \sim 10$ mm, $m \sim 0.1$ pg, $\omega \sim 200$ THz, gives $g_0/2\pi \sim 100$ Hz. Reaching the strong single-photon-phonon coupling regime, *i.e.* $\kappa < g_0$ thus requires extremely low loss cavities.

Finally, we introduce an optical drive with frequency ω_l which adds another term to the Hamiltonian. Adding this term and going to a rotating frame[3] that rotates at the laser drive frequency gives the final optomechanical Hamiltonian [24]

$$\hat{H}_{\mathrm{OM}} = \hbar\Omega_{\mathrm{m}}\hat{b}^\dagger\hat{b} - \hbar\Delta\hat{a}^\dagger\hat{a} - \hbar g_0(\hat{b} + \hat{b}^\dagger)\hat{a}^\dagger\hat{a} + i\hbar E(\hat{a}^\dagger - \hat{a})\,, \tag{2.49}$$

where E is related to the power P of the laser drive $|E| = \sqrt{P\kappa/\hbar\omega_l}$ and $\Delta = \omega_l - \omega$ is the cavity detuning.

[3] $\hat{H}_{\mathrm{rot}}(t) = i\hbar\frac{\partial\hat{R}(t)}{\partial t}\hat{R}(t)^\dagger + \hat{R}(t)\hat{H}(t)\hat{R}(t)^\dagger$ where $\hat{R}(t) = \exp\left(i\omega_l\hat{a}^\dagger\hat{a}t\right)$.

2.3.2 Linearized coupling and the Langevin equations

Given the optomechanical Hamiltonian (2.49) we are now ready to study the dynamics of the system at hand. However, complications arise from the nonlinear nature of the interaction which makes analytical treatment of the system cumbersome. To tackle this we study the system by using a semi-classical approach in which the optical amplitude of the cavity $\hat{a}$ is given by

$$\hat{a} = \alpha + \delta\hat{a}\,. \tag{2.50}$$

Here it's assumed that the input field has a strong, time independent coherent amplitude denoted α with only small time dependent fluctuations $\delta\hat{a}$ where $\sqrt{\langle\delta\hat{a}^2\rangle} \ll |\alpha|$. In this description α is a complex number but is without loss of generality taken to be real and is connected to the intracavity photon number $\alpha = \sqrt{n_{\mathrm{cav}}}$. Using this approach prevents us from analyzing nonlinear quantum effects such as optomechanical parametric instability [6].

Given this assumption, the interaction term can be simplified to [6]

$$\hat{H}_{\mathrm{int,lin}} = -\hbar g_0\sqrt{n_{\mathrm{cav}}}(\delta\hat{a}^\dagger + \delta\hat{a})(\hat{b}^\dagger + \hat{b}) \tag{2.51}$$

From this equation we see that the coupling is now dependent on the strength of the intracavity field, therefore we define the optomechanical coupling strength as $g = g_0\sqrt{n_{\mathrm{cav}}}$. This interaction term describes four possible processes a system state can evolve according to, described by the terms in (2.51)

$$\begin{aligned}
&\delta\hat{a}^\dagger\hat{b} && \text{transfer of phonon to photon,}\\
&\delta\hat{a}\hat{b}^\dagger && \text{transfer of photon to phonon,}\\
&\delta\hat{a}^\dagger\hat{b}^\dagger && \text{creation of phonon and photon pair,}\\
&\delta\hat{a}\hat{b} && \text{annihilation of phonon and photon pair.}
\end{aligned} \tag{2.52}$$

Solving the Heisenberg equation for the uncoupled motion of the operators $\delta\hat{a}$ and $\hat{b}$ gives [30]

$$\begin{aligned}
\delta\hat{a}(t) &= \delta\hat{a}(0)\mathrm{e}^{\mathrm{i}\Delta t}\,,\\
\hat{b}(t) &= \hat{b}(0)\mathrm{e}^{-\mathrm{i}\Omega_{\mathrm{m}}t}\,,
\end{aligned} \tag{2.53}$$

which allows for invoking the rotating wave approximation for the terms in (2.52) when the cavity detuning $\Delta = \pm\Omega_{\mathrm{m}}$. For red cavity detunings *i.e.*, $\Delta \approx -\Omega_{\mathrm{m}}$, the last two terms of (2.52) can be omitted due to fast oscillations $\exp(\pm\mathrm{i}(\Delta - \Omega_{\mathrm{m}})) \approx \exp(\mp 2\mathrm{i}\Omega_{\mathrm{m}})$. For this detuning the interaction reads

$$\hat{H}_{\mathrm{int,BS}} = -\hbar g(\delta\hat{a}^\dagger\hat{b} + \delta\hat{a}\hat{b}^\dagger) \tag{2.54}$$

and is sometimes called "Beam Splitter" interaction which describes two harmonic oscillators exchanging energy quanta at the rate g.

The linear nature of the presented Hamiltonian is not at first glance apparent due to the field operator products in (2.52). However, the linearity will become clear when studying the dynamics of the system. Due to the two quantum systems being in contact with environments, the effects of the bath has to be taken into account. The evolution of quantum operators under the influence of stochastic forces is neatly described by Langevins equations which, for an operator $\hat{O}$, is formulated [23]

$$\frac{\partial \hat{O}}{\partial t} = \frac{i}{\hbar}\left[\hat{H}, \hat{O}\right] + \hat{N}\,. \tag{2.55}$$

where $\hat{H}$ is the system Hamiltonian and $\hat{N}$ is the corresponding stochastic noise terms for the operator $\hat{O}$. In addition, the coupling to the environment will also open up a channel for energy in the optomechanical system to dissipate. Regarding the quantum system as open, input-output theory gives the rates at which dissipation and coupling to external forces takes place [31]. The interaction between systems, external noise and drive is depicted in Figure 2.8.

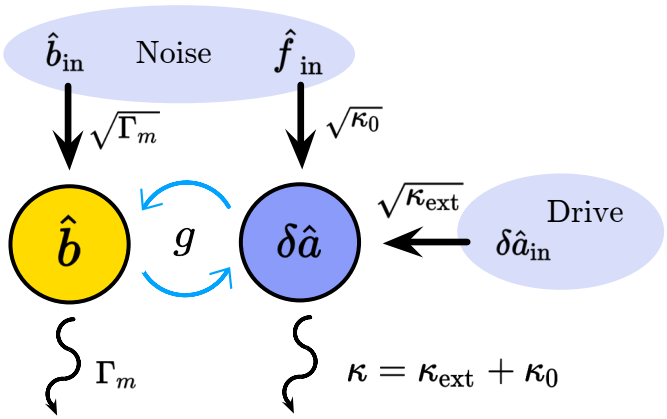

Figure 2.8: Schematic of the driven optomechanical system. The mechanical ($\hat{b}$) and optical ($\delta\hat{a}$) modes are coupled by the optomechanical coupling strength g. The modes are coupled to environmental noise fields $\hat{b}_{\text{in}}$ and $\hat{f}_{\text{in}}$ through couplings Γ_{m}, κ_0, respectively. The optical field is also driven by $\delta\hat{a}_{\text{in}}$ through the coupling κ_{ext}. Finally, the modes dissipate with rates Γ_{m} and $\kappa = \kappa_{\text{ext}} + \kappa_0$, respectively.

Now, taking the above system-environment interactions into consideration, we derive the equations of motion for the linearized optomechanical system by inserting the optomechanical Hamiltonian with the linearized interaction (2.51) into (2.55).

$$\begin{aligned}
\dot{\delta\hat{a}} &= \left(i\Delta - \frac{\kappa}{2}\right)\delta\hat{a} + ig(\hat{b}^\dagger + \hat{b}) + \sqrt{\kappa_{\text{ex}}}\delta\hat{a}_{\text{in}} + \sqrt{\kappa_0}\hat{f}_{\text{in}}\,, \\
\dot{\hat{b}} &= \left(i\Omega_{\text{m}} - \frac{\Gamma_{\text{m}}}{2}\right)\hat{b} + ig(\delta\hat{a}^\dagger + \delta\hat{a}) + \sqrt{\Gamma_{\text{m}}}\hat{b}_{\text{in}}\,.
\end{aligned} \tag{2.56}$$

These coupled differential equations model how the amplitudes of the mechanical and

optical fields evolve in time. The coupling between the optical and mechanical field is the optomechanical coupling strength g introduced above and is controlled by managing the population of the intracavity field. The equations also describe how the modes of interest are influenced by external fields being the input optical drive $\delta\hat{a}_{\mathrm{in}}$ and optical (mechanical) noise fields $\hat{f}_{\mathrm{in}}$ ($\hat{b}_{\mathrm{in}}$). Finally, added to these equations are also damping terms $-\kappa\delta\hat{a}/2$ ($-\Gamma_{\mathrm{m}}\hat{b}/2$) for the optical (mechanical) fields which is valid for small damping rates $\Gamma_{\mathrm{m}} \ll \Omega_{\mathrm{m}}$ [6].

2.3.3 Optical spring effect and optomechanical damping

With the results from the previous section in terms of the linear equations of motion, we are now ready to look at the consequences of the optomechanical coupling. Solving Langevins equations (2.56) is most conveniently done in the frequency domain by the means of the Fourier transform, similar to Section 2.1.1. Firstly, we go to the classical averaged version of (2.56) by expressing the second equation in terms of the position operator $\hat{x} = x_{\mathrm{ZPF}}(\hat{b} + \hat{b}^{\dagger})$ and then taking the average $\langle\cdot\rangle$. Utilizing that the vacuum fluctuations and thermal bath noise has zero mean *e.g.* $\langle\hat{a}_{\mathrm{in}}\rangle = \langle\hat{f}_{\mathrm{in}}\rangle = 0$ gives

$$\begin{aligned} \dot{\alpha} &= (\mathrm{i}\Delta - \frac{\kappa}{2})\alpha + \mathrm{i}Gx + \sqrt{\kappa_{\mathrm{ex}}}\alpha\,, \\ m\ddot{x} &= -m\Gamma_{\mathrm{m}}\dot{x} - m\Omega_{\mathrm{m}}x + G\hbar|\alpha|^2\,. \end{aligned} \tag{2.57}$$

with $\alpha = \langle\delta\hat{a}\rangle$, $x = 2x_{\mathrm{ZPF}}\mathrm{Re}\{\langle\hat{b}\rangle\}$ and $G = \omega_{\mathrm{cav}}/L$ is the optical frequency shift per unit length. Note that in going between the equations for $\hat{b}$ and $\hat{x}$ we require $\Gamma_{\mathrm{m}} \ll \Omega_{\mathrm{m}}$. Finally we can solve for the mechanical susceptibility in Fourier space yielding

$$\chi_{\mathrm{opt}} = \frac{1}{m(\Omega_{\mathrm{m}}^2 + 2\omega\delta\Omega_{\mathrm{m}}(\omega) - \omega^2 - \mathrm{i}\omega(\Gamma_{\mathrm{m}} + \Gamma_{\mathrm{opt}}(\omega)))}, \tag{2.58}$$

which has the same appearance as the unperturbed mechanical susceptibility (2.4) up to two additional terms

$$\begin{aligned} \delta\Omega_{\mathrm{m}}(\omega) &= g^2\frac{\Omega_{\mathrm{m}}}{\omega}\left(\frac{\Delta+\omega}{(\Delta+\omega)^2+\kappa^2/2} + \frac{\Delta-\omega}{(\Delta-\omega)^2+\kappa^2/2}\right), \\ \Gamma_{\mathrm{opt}}(\omega) &= g^2\frac{\Omega_{\mathrm{m}}}{\omega}\left(\frac{\kappa}{(\Delta+\omega)^2+\kappa^2/2} - \frac{\kappa}{(\Delta-\omega)^2+\kappa^2/2}\right), \end{aligned} \tag{2.59}$$

with quadratic dependence on the optomechanical coupling g. The terms in (2.59) are responsible for two optomechanical phenomena known as optical spring effect and optomechanical damping. Figure 2.9 visualizes the two terms at $\omega = \Omega_{\mathrm{m}}$ for a range of detunings Δ. The interaction is visualized in two different regimes: sideband resolved ($\kappa < \Omega_{\mathrm{m}}$) and sideband un-resolved ($\kappa > \Omega_{\mathrm{m}}$) which visualizes the importance of these ratios.

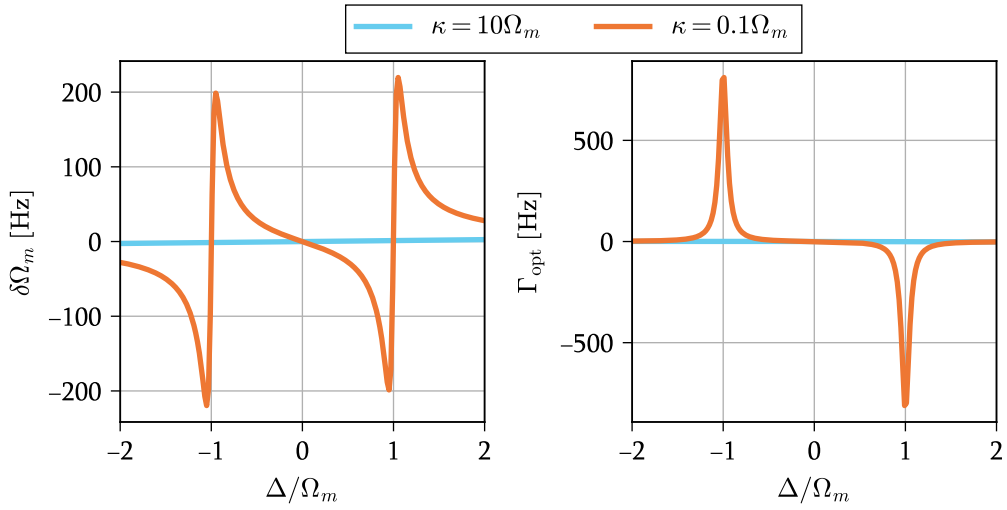

Figure 2.9: Calculation of **a.** $\delta\Omega_{\mathrm{m}}$ and **b.** Γ_{opt} with parameters $g/2\pi = 1$ kHz, $\omega/2\pi = \Omega_{\mathrm{m}} = 300$ kHz and $\kappa = 10\Omega_{\mathrm{m}}$ $(0.1\Omega_{\mathrm{m}})$ visualizing the un-resolved (resolved) sideband regimes. In **b.**, optomechanical damping (heating) is achieved for detunings $\Delta = -\Omega_{\mathrm{m}}$ $(+\Omega_{\mathrm{m}})$.

The optical spring effect is an optomechanical shift in the frequency of the mechanical mode. Intuitively, the force induced by the radiation pressure of the intracavity field displaces the resting position of the mechanical resonator where the force constant of the spring differs slightly, inducing a shift in the resonance frequency.

The nature of the optomechanical damping is a bit more intricate and originates from an inherent delay in the optomechanical back-action due to the cavity decay rate κ. Intuitively, it can be understood as Stokes- and Anti-Stokes processes. For negative (red) detunings the Anti-Stokes process dominates and photons are scattered into a higher energy state when interacting with the mechanical resonator which extracts energy from the mode, resulting in an effective cooling. The opposite is true for positive (blue) detunings where incident photons scatter into lower energy bands (Stokes process), depositing energy into the mechanical mode which effectively heats up the system. The effective temperature of the mechanical mode is connected to the damping rate through [24]

$$T_{\mathrm{eff}} = T\frac{\Gamma_{\mathrm{m}}}{\Gamma_{\mathrm{m}} + \Gamma_{\mathrm{opt}}} \tag{2.60}$$

where T is the unperturbed temperature. This can further be connected to the effective phonon occupation in the mode according to the Bose-Einstein distribution

$$n_{\mathrm{eff.phon}} = \frac{1}{\exp\{\hbar\Omega_{\mathrm{m}}/k_{\mathrm{B}}T_{\mathrm{eff}}\} - 1}\,. \tag{2.61}$$

The cooling phenomenon, known as sideband cooling, is not exclusive to this realization of the optomechanical system and is used for example to reach ground states of motion in

ion trap systems [32]. In the range of nano/micromechanics, this type of sideband cooling has demonstrated close to ground state cooling of mechanical modes in both cryogenic environments [7] and room temperature [33].

2.3.4 Optomechanics with multielement resonators

In the previous section, the optical spring effect and optomechanical cooling were introduced having magnitudes proportional to $g^2 = n_{\mathrm{cav}} g_0^2$. Thus by increasing the intracavity photon number, *i.e.* increasing the optical pump power, the interaction gets more pronounced. However, there are other reasons to increase the interaction for weak pump fields. This is done by increasing the single photon coupling strength g_0.

To see why this is important we remind ourselves that the single photon coupling strength $g_0 = x_{\mathrm{ZPF}} \partial\omega_{\mathrm{cav}}/\partial x$ is a measure of how much the zero-point-fluctuations of the mechanical mode affect the cavity frequency. Now, visualize a thought experiment where a stream of photons with frequency ω is incident on an unoccupied optomechanical cavity with resonance frequency $\omega_{\mathrm{cav}} = \omega$. The first photon reaching the cavity is resonant with the optical mode and is allowed to enter. Inside the cavity the photon interacts with the mechanical mode of the optomechanical system via the coupling strength g_0. If the optomechanical coupling is strong enough to displace the optical resonance frequency by more than a cavity linewidth κ, the next incident photon is no longer resonant with the cavity and is not allowed to enter. This effect is called *photon blockade effect* which is a single-photon nonlinear optical effect [34], [35]. It allows for studying single photon correlations with relevance in *e.g.* quantum information processing [36]. The photon blockade effect is enabled by a quantum optomechanical system which acts non-linearly *i.e.* enabling Gaussian input states to be mapped onto non-Gaussian output states. This non-linearity also allows for using light to generate non-classical mechanical states such as Fock-states and Schrödingers cat states. This is of fundamental physical interest in the realm of micro-mechanics due to its large mass and length scales, but can also open doors for novel ultra-sensitive sensing applications [6].

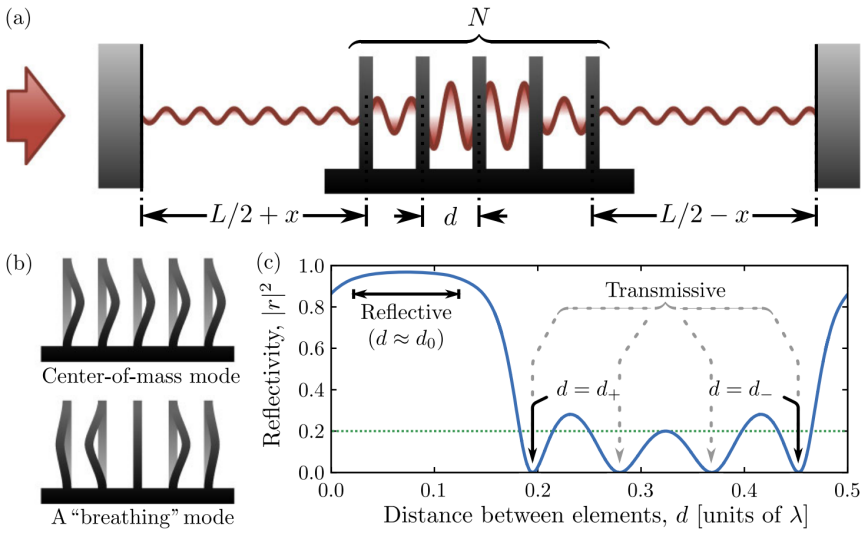

Figure 2.10: (a) Proposed multi-element optomechanical system with N dielectric membranes separated by d in a cavity of length L. (b) Depiction of collective mechanical modes to which the optical field is coupled to. (c) Stack reflectivity for $N = 6$ non-absorbing resonators as function of the seperation d (blue) and the single-element reflectivity (dotted green). Figure taken from [17]

.

One proposed way of increasing the single-photon coupling strength g_0 to be greater than the cavity decay κ and thus enter the single-photon strong coupling regime is by using multi-element mechanical resonators, introduced in 2012 by Xuereb *et al.* [17]. The suggested setup is depicted in Figure 2.10 where a stack of N independent and identical mechanical resonators is placed within a cavity and is collectively interacting with the intracavity field. As opposed to other membrane in the middle approaches [15], the distance d between individual resonators is such that the stack behaves transmissively for arbitrary single element reflectivities $R < 1$ which allows for long range optomechanical interactions in the stack.

The mechanical mode to which the intracavity field couples to is a collective motion of the independent membranes of the stack called supermodes, examples of which are shown in Figure 2.10(a). Due to the non-zero reflectivity of the membranes, the optical field strength between the membranes is increased which enhances the optomechanical coupling to the supermode. The coupling to a sinusodial supermode of a transmissive stack of N elements is given by

$$g_{\sin} = \sqrt{\sum_{j=1}^{N} (g_j)^2}\,, \tag{2.62}$$

where g_j is the coupling to the motion of the individual resonators.

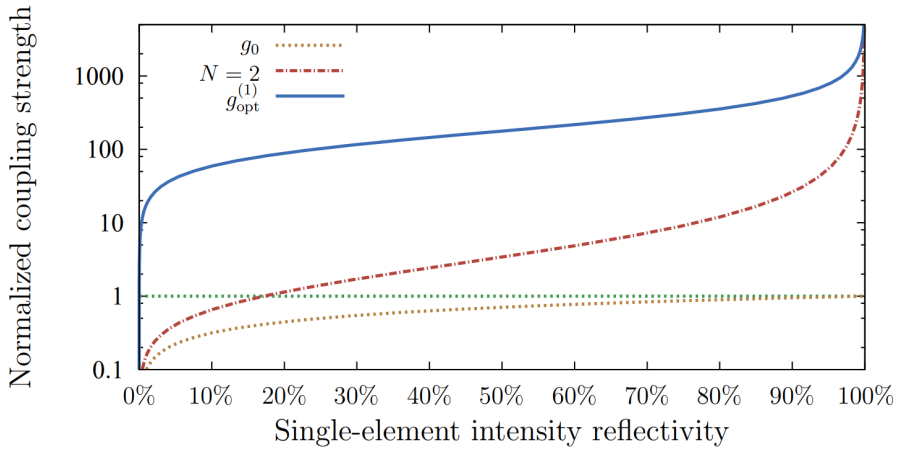

Figure 2.11: Optomechanical coupling strengths for different numbers of elements in the transmissive stack normalized to the perfectly reflecting single element coupling. The number of elements for the blue curve is optimized for high g_0 at each R whereas $N = 2$ (1) for the dot-dashed red (dotted yellow) curves. For $R \to 1$, $N = 2$ is enough to achieve a several orders of magnitude increase of g_0. Figure taken from [19].

The optimal number of elements N which yields the largest coupling of the transmissive stack is dependent on the reflectivity of the individual membranes which is shown in Figure 2.11. The blue curve shows the optomechanical coupling to a stack with the optimal number of membranes in the stack whereas dashed red (yellow) shows the coupling to two (one) membranes. The graph is normalized to the coupling to a perfectly reflecting back mirror of a canonical optomechanical system. For single-element reflectivities $R \to 1$, $N = 2$ is enough to achieve a several orders of magnitude increase of g_0 which can allow for reaching the $g_0 > \kappa$ strong coupling regime in a high finesse optical cavity.

2.4 Photonic crystals

Achieving high optomechanical coupling rates by the means of multi-element mechanical resonators requires either a large number of elements in the mechanical resonator stack, high single element reflectivities or a combination of both [17]. While high reflectivities can be achieved in stacks of alternating dielectric films (distributed bragg reflectors) [12] these devices are several micro-meters thick which makes them hard to incorporate into multielement stacks. On the other hand, sub-micron dielectric films such as SiN membranes provide stackable geometry but lack in reflectivity, $R \sim 0.4$ [15]. However, using modern microfabrication techniques, thin dielectric films can be periodically patterned with *photonic crystals* (PhC) allowing to create highly reflective nanometer-thin membranes by engineering photonic band gaps in the desired wavelength range.

The fundamentals of propagating electromagnetic waves in photonic crystals are very sim-

ilar to that of moving electrons in periodic potentials caused by atomic crystal structures. When solving for the electron dynamics within an atomic lattice, the periodicity of the boundary conditions is utilized to express solutions as Fourier expansions in reciprocal space. This allows for finding dispersion relations for the electron propagation inside the structure that most commonly are visualized as electronic band diagrams.

To understand how photonic band gaps emerge within periodic dielectric structures we study a one dimensional photonic crystal by means of *plane wave expansion* (PWE). The derivation given here is similiar to the one presented in [37]. The electric permittivity $\epsilon(x)$ of the dielectric medium in which the equations are solved is assumed to have translational symmetry with lattice constant X *i.e.* $\epsilon(x+X) = \epsilon(x)$. We start out with a stationary version of Maxwell's equations where the spatial distribution of the magnetic field component $H(x)$ is described by a Helmholtz equation similar to (2.22)

$$\frac{\partial}{\partial x}\frac{1}{\epsilon(x)}\frac{\partial}{\partial x}H(x) + \frac{\omega^2}{c^2}H(x) = 0\,, \tag{2.63}$$

the difference being the position dependent permittivity $\epsilon(x)$. We study the wave equation for the magnetic field component due to it having a more convenient form as opposed to when formulating the problem for the electric field. Assuming that the spatial extension of the photonic crystal is infinite, (2.63) is equivalent with finding the eigenstate $H(x)$ to the operator $\hat{\Theta} = -\frac{\partial}{\partial x}\frac{1}{\epsilon(x)}\frac{\partial}{\partial x}$ with eigenvalue $\lambda = \omega^2/c^2$. The boundary conditions of the problem allow for invoking the Bloch theorem

$$H(x) = h_{k,n}(x)\exp(ikx)\,. \tag{2.64}$$

This ansatz expresses the eigenfunction as a plane wave with wave vector k multiplied by a lattice periodic function[4] $h_{k,n}(x)$ for the specific wave vector k and energy state n. Now, expanding the periodic functions $\epsilon(x)$ and $h_{k,n}(x)$ in the reciprocal lattice vectors $G = \{g_n\}_{n=1}^{\infty}$,

$$\begin{aligned}\frac{1}{\epsilon(x)} &= \sum_{g\in G}\chi(g)\exp\{igx\}\,,\\ h_{k,n}(x) &= \sum_{g\in G}h_{k,n}(g)\exp\{igx\}\,,\end{aligned} \tag{2.65}$$

allows for rewriting (2.63) as a matrix equation

$$M\vec{h}_{k,n} = \frac{\omega^2}{c^2}\vec{h}_{k,n} \tag{2.66}$$

where

$$\begin{aligned}M &= \begin{bmatrix} M_{g_1g_1} & M_{g_1g_2} & \dots \\ M_{g_2g_1} & M_{g_2g_2} & \dots \\ \vdots & \vdots & \ddots \end{bmatrix}, \qquad \vec{h}_{k,n} = \begin{bmatrix} h_{k,n}(g_1) \\ h_{k,n}(g_2) \\ \vdots \end{bmatrix},\\ M_{gg'} &= \chi(g-g')((k+g')\cdot(k+g))\,.\end{aligned} \tag{2.67}$$

[4] meaning that the period is equal to that of the lattice $h_{k,n}(x+X) = h_{k,n}(x)$

This equation is called the "Master equation" for one dimensional PhCs. The solutions to the master equation are the eigenvalues of M which give the dispersion relation $\omega(k)$. The eigenvalue problem (2.66) can be truncated for a certain number of reciprocal lattice vectors g and solved numerically [37].

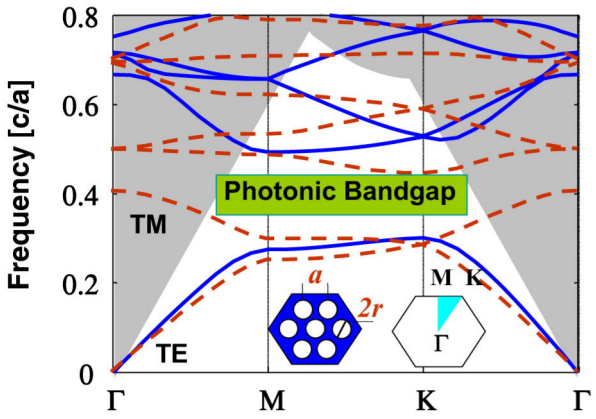

Figure 2.12: Photonic band diagram of the 2D PhC structure shown in the left inset. Dispersion relations for transverse magnetic (TM, red dashed) and transvers electric (TE, blue) are shown for the k-path shown in the left inset, connecting the high symmetry points of the Brillouin zone. A PBG is achieved for frequencies ~ 0.4 c/a [38]

.

The dispersion relation $\omega(k)$ holds information of the eigenenergies of the guided modes of the PhC which restricts waves of certain frequency to a specific k-vector in the PhC. The dispersion relation is most commonly visualized in a band diagram, an example of which is shown in Figure 2.12. The band diagram allows for identifying *photonic bandgaps* (PBG) where an incident electromagnetic wave of a certain frequency does not have an available wave vector in the material below the light line. In effect the energy of the wave is not allowed to pass into the PhC and must therefore be scattered. Photonic crystal engineering therefore allows for creating nano-meter thin broadband reflectors for a desired frequency range by carefully choosing photonic crystal patterns and lattice parameters [39]. The choice of parameters is guided by simulations performed in a software called S^4 which combines rigorous coupled wave analysis and scattering matrix formalism to calculate PhC reflectivities [20].

3. Experimental methods

To study an optomechanical system, state of the art experimental equipment and techniques are required, the principles of which will be discussed in this chapter. I begin by introducing the techniques which allow for precise optical measurements of the system under study. Next, the experimental setup is introduced, describing how micro-mechanical resonators are incorporated into high finesse optical cavities. Finally, the measurement setup is described.

3.1 Optical measurement and locking techniques

Several experimental techniques must be mastered to measure the relevant optomechanical quantities such as κ, Ω_{m}, Γ_{m} and g_0. In this section, two techniques involving precise control of a laser are presented, allowing for stable readout of the optomechanical system.

3.1.1 Cavity frequency locking

As seen in Section 2.2, to populate the intracavity field of an optical cavity, the frequency of an incident laser must fall within the linewidth of the cavity resonance frequency. To find the resonance, one simply scans either the laser frequency ω_{in} or the cavity length L over several free spectral ranges and looks for cavity transmission, as seen in Figure 2.4. However, the cavity resonance frequency is highly sensitive to thermal and mechanical noise, which makes stabilizing laser frequency at resonance paramount. In addition, the narrow line width of high finesse cavities impose further limits to frequency matching. Locking the laser frequency to the resonance of the cavity is a system control problem, which can be solved by a simple feedback loop given an appropriate error signal.

Consider the block diagram presented in Figure 3.1. Here, the input of the loop is a signal setting the laser frequency ω, which in this example is the control variable of the problem. The laser passes through the system under study, producing an output which is used to generate the error signal $\epsilon(\omega)$. The error signal is processed by a Proportional Integral Differential (PID) regulator before the result is added to the input signal, closing the feedback loop. The job of the feedback loop is to regulate the control variable around the desired value, which in this case is the cavity resonance frequency ω_{cav}. The error signal $\epsilon(\omega)$ of a feedback loop is generally a function with a distinct slope at a desired value. For this problem, we thus require

$$\epsilon(\omega) \propto \omega \quad \text{for} \quad \omega \sim \omega_{\mathrm{cav}} \,. \tag{3.1}$$

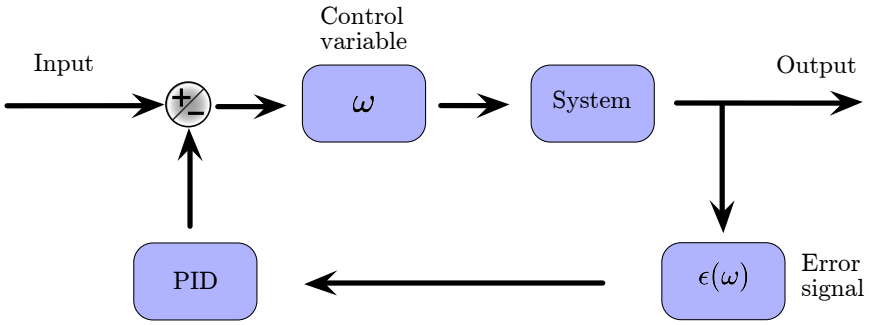

Figure 3.1: Block diagram of the system control problem to regulate the output frequency of the laser. The control variable ω is fed an initial input signal before its output gets sent to the system under study. The output of the system is used to generate an error signal $\epsilon(\omega)$ which goes through a PID servo before closing the feedback loop.

The linearity of the error signal around the desired value allows for systematic regulation of the control variable to stabilize the system output. The problem is thereby reduced to finding an error signal with the appropriate properties.

3.1.1.1 Side of fringe locking

The simplest form of an error signal generated as a cavity frequency response is the cavity transmission/reflection shown in Figure 2.4. The apparent problem of using this signal is that the condition (3.1) does not hold due to the signal having a local maximum at $\omega = \omega_{\text{cav}}$. However, the side of the cavity *fringe* can be seen as locally linearly proportional to the frequency and a lock can therefore be found to a slightly detuned cavity resonance frequency.

3.1.1.2 Pound-Drever-Hall locking

A more sophisticated method is required to lock the laser frequency to the center of the cavity resonance. At first glance, the derivative of the transmitted signal should be able to produce a signal that upholds the condition (3.1). The derivative can be accessed through electronic derivation of the reflected signal, but has risks of introducing phase shifts and electronic noise. Alternatively, sampling the derivative can be done through modulation of the laser phase, this is called the Pound-Drever-Hall (PDH) technique and is briefly introduced below. The following derivation follows closely that of [40].

We start out by looking at the amplitude reflection coefficient r of a symmetric, lossless FP cavity with intensity reflection coefficient of the mirrors denoted by R. From (2.31) it can be seen that

$$r(\omega) = \frac{A_{\text{refl}}}{A_{\text{in}}} = \sqrt{R}\frac{\mathrm{e}^{-\mathrm{i}\delta\phi(\omega)} - 1}{1 - R \cdot \mathrm{e}^{-\mathrm{i}\delta\phi(\omega)}}\,. \tag{3.2}$$

Measuring the intensity of the reflected signal, normalized to the incident intensity, gives access to $|r(\omega)|^2$. As mentioned above, this signal is not an optimal error signal due to it having a vanishing slope at $\omega = \omega_{\text{cav}}$. However, we now look at the reflection of a phase-modulated incident light field, which can be achieved by using an Electro Optical Modulator (EOM). The amplitude of a phase modulated incident light field can be expressed as

$$A_{\text{in}}(t) = A_0 \mathrm{e}^{\mathrm{i}\omega t + \mathrm{i}\gamma \sin \Omega t}\,, \tag{3.3}$$

where A_0 is the amplitude at $t = 0$, ω is the frequency of the light, γ is the modulation depth and Ω is the modulation frequency. For small modulation depths γ, a small angle approximation can be performed, which gives

$$A_{\text{in}}(t) \approx A_0 \mathrm{e}^{i\omega t}(1 + \mathrm{i}\gamma \sin(\Omega t)) = A_0 \left[\mathrm{e}^{i\omega t} + \frac{\gamma}{2}\left(\mathrm{e}^{\mathrm{i}t(\omega+\Omega)} - \mathrm{e}^{\mathrm{i}t(\omega-\Omega)}\right)\right], \tag{3.4}$$

which describes an electromagnetic wave of frequency ω modulated with sidebands at frequencies $\omega + \Omega$ and $\omega - \Omega$. Letting this signal reflect off the cavity will give each band a reflection coefficient at the appropriate frequency, *i.e.*

$$A_{\text{refl}} = A_0 \left[r(\omega)\mathrm{e}^{i\omega t} + \frac{\gamma}{2}\left(r(\omega+\Omega)\mathrm{e}^{\mathrm{i}t(\omega+\Omega)} - r(\omega-\Omega)\mathrm{e}^{\mathrm{i}t(\omega-\Omega)}\right)\right]. \tag{3.5}$$

We now look at the intensity of the reflected signal by taking the square of (3.5)

$$\begin{aligned} I_{\text{refl}}/I_0 = |A_{\text{refl}}/A_0|^2 =& |r(\omega)|^2 + \frac{\gamma^2}{4}\left(|r(\omega+\Omega)|^2 + |r(\omega-\Omega)|^2\right) + \\ & \gamma\cos(\Omega t)\mathrm{Re}\left\{r(\omega)r(\omega+\Omega)^* - r(\omega)^* r(\omega-\Omega)\right\} + \\ & \gamma\sin(\Omega t)\mathrm{Im}\left\{r(\omega)r(\omega+\Omega)^* - r(\omega)^* r(\omega-\Omega)\right\} + \\ & 2\Omega \text{ terms}. \end{aligned} \tag{3.6}$$

The above expression consists of two DC terms, two terms oscillating at the modulation frequency Ω and additional terms oscillating at twice the modulation frequency not explicitly written out for convenience.

Turning our attention to the term $r(\omega)r(\omega+\Omega)^* - r(\omega)r(\omega-\Omega)^*$, we look at the case when the modulation frequency is large compared to the line width of the cavity, *i.e.* $\Omega > \kappa$. In this case, when the carrier wave is resonant with the cavity, the sidebands at $\omega \pm \Omega$ will be totally reflected and hence $r(\omega \pm \Omega) \approx -1$, we thus have

$$r(\omega)r(\omega+\Omega)^* - r(\omega)^* r(\omega-\Omega) \approx -2\mathrm{i}\mathrm{Im}\left\{r(\omega)\right\}. \tag{3.7}$$

Therefore, the term proportional to $\cos(\Omega t)$ in (3.6) can be neglected.

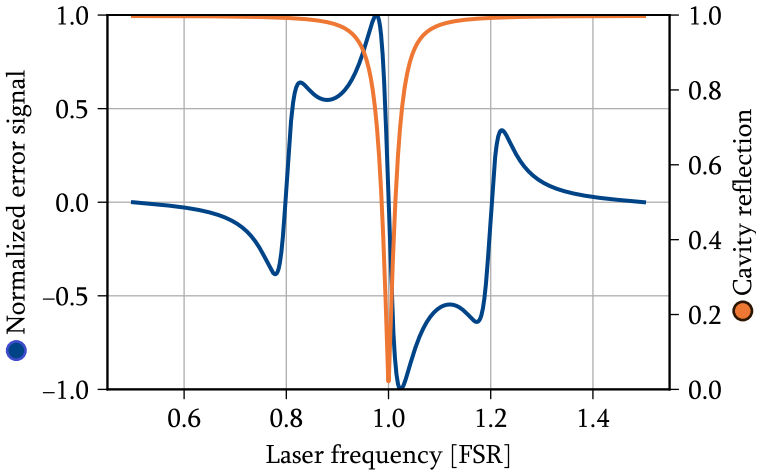

Figure 3.2: **Orange:** Cavity reflection $|r(\omega)|^2$. The negative linear slope of the error signal around the cavity resonance frequency is used to stabilize the laser-cavity system. **Blue:** Normalized Pound-Drever-Hall error signal for high modulation frequencies $\Omega > \kappa$.

Now, looking at the leftover term oscillating at the modulation frequency, plotted in Figure 3.2, we see that it successively produces a linear slope when $\omega \sim \omega_{\text{cav}}$ and is thus a valid error signal. This is the so called Pound-Drever-Hall error signal and can be extracted by demodulation. Demodulation is performed by multiplying the cavity reflection output with a signal oscillating at the modulation frequency, which produces a DC component proportional to the error signal. Finally, the DC component is singled out with a lowpass filter.

3.1.2 Homodyne detection

The micromechanical systems discussed in Section 3.3.1 exhibit oscillating motion with amplitudes in the nm range. This motion has to be accurately monitored to examine the mechanical properties of the optomechanical system. In this section, we discuss how the motion of the micromechanical system can be mapped as phase noise on the optical field and subsequently monitored using *Homodyne Detection*.

We remind ourselves of the canonical optomechanical system in Figure 2.7 where the intracavity field impinges parallel to the motion of the back mirror of the cavity. Due to the time-dependent displacement of the mirror $x(t)$, the distance travelled by the light that enters the cavity and reflects off the moving mirror will also depend on time. The difference in path length is thus mapped onto the phase of the reflected field $\Delta\phi(t) = 2kx(t)$, where k is the wave vector of the incident light and the factor 2 accounts for the reflected wave travelling the extra path length twice. This mapping allows for inferring the back mirror movement by monitoring the phase of the reflected light.

To measure the phase of the light reflected off the optomechanical system, an interferometric system using a reference beam referred to as the *local oscillator* (LO) is used. We now introduce a detection scheme that uses an LO with strong coherent amplitude to monitor the phase quadrature of a signal beam. When the frequency of the LO is equal to that of the signal beam the detection scheme is called homodyne detection (HD), otherwise we refer to it as heterodyne detection.

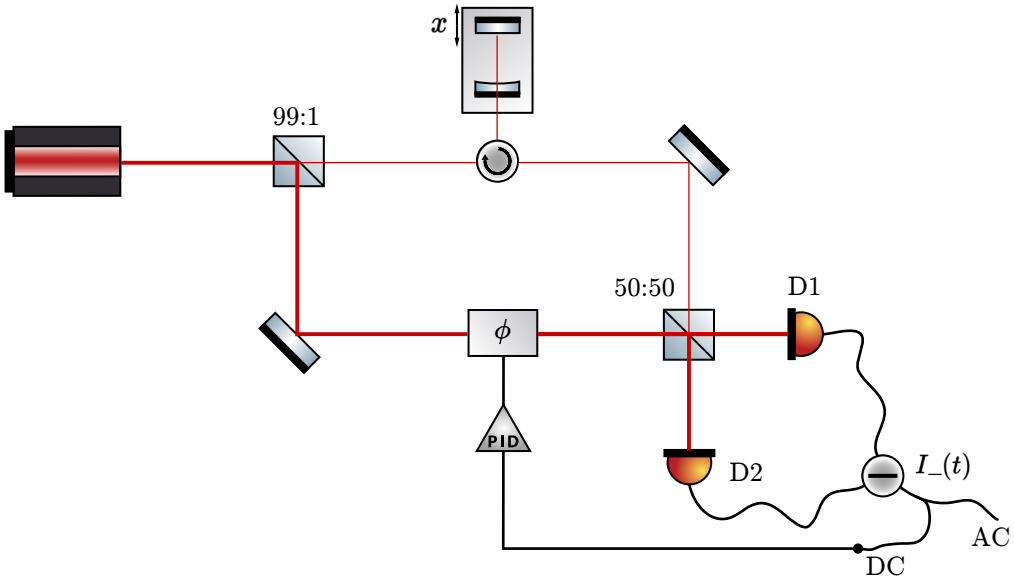

Figure 3.3: Standard homodyne detection setup. The power output of a laser is split on a 99:1 BS, sending 99 % to the LO arm and 1 % to the signal arm. The signal arm interacts with the system under study while the LO picks up a phase ϕ before they are recombined on a 50:50 BS and detected on PDs D1 and D2. The current $I_{-}(t)$ is simultaneously monitored and used as error signal for locking to the phase quadrature of the signal.

The standard HD setup is presented in Figure 3.3. The output of a laser diode is split on a 99:1 beamsplitter (BS) sending 99% of the light to the LO arm and 1% to the signal arm. The beams are redirected through separate paths, where the signal arm is allowed to interact with the optomechanical system and the LO gathers a variable phase ϕ, before being recombined on a 50:50 BS. The output of the 50:50 BS is detected with two photo diodes (PD) D1 and D2. The complex amplitude of the signal (LO) arm before hitting the 50:50 BS is denoted $\alpha_{\mathrm{sig}}(t)$ ($\alpha_{\mathrm{LO}}(t)$) and are given by

$$\begin{aligned} \alpha_{\mathrm{sig}}(t) &= \alpha_{\mathrm{sig}} + \delta X_{\mathrm{sig}}(t) + \mathrm{i}\delta Y_{\mathrm{sig}}(t)\,, \\ \alpha_{\mathrm{LO}}(t) &= \left(\alpha_{\mathrm{LO}} + \delta X_{\mathrm{LO}}(t) + \mathrm{i}\delta Y_{\mathrm{LO}}(t)\right) \mathrm{e}^{i\phi}\,. \end{aligned} \tag{3.8}$$

In this description, we assume that both arms have large and time-independent coherent amplitudes $\alpha_{\mathrm{sig}}, \alpha_{\mathrm{LO}} \in \mathbb{R}$ compared to the associated amplitude and phase quadrature noise terms δX, δY. In addition, due to the 99:1 BS we have $|\alpha_{\mathrm{sig}}| \ll |\alpha_{\mathrm{LO}}|$. As discussed above, the mechanical displacement noise of the optomechanical system is stored in the

phase noise of the signal arm $\delta Y_{\mathrm{sig}}(t)$, which therefore is the variable of interest.

To calculate the intensities on the two PDs we propagate the amplitudes of the signal and LO arm through the 50:50 BS which gives [27]

$$\begin{aligned} \alpha_{\mathrm{D1}}(t) &= \frac{1}{\sqrt{2}}(\alpha_{\mathrm{LO}}(t) - \alpha_{\mathrm{sig}}(t)) \,, \\ \alpha_{\mathrm{D2}}(t) &= \frac{1}{\sqrt{2}}(\alpha_{\mathrm{LO}}(t) + \alpha_{\mathrm{sig}}(t)) \,, \end{aligned} \tag{3.9}$$

where the minus sign in the first equation is picked up due to the reflected part of the signal arm being assumed to reflect off a medium with high refractive index. Now, taking the difference of the photo currents of D1 and D2 while only keeping terms proportional to α_{LO} due to the intensity difference between signal and LO arms we get

$$\begin{aligned} I_{-}(t) =& \left|\alpha_{\mathrm{D2}}(t)\right|^2 - \left|\alpha_{\mathrm{D1}}(t)\right|^2 = 2\mathrm{Re}\left\{\alpha^*_{\mathrm{sig}}(t)\alpha_{\mathrm{LO}}(t)\right\} \approx \\ & 2\alpha_{\mathrm{LO}}\alpha_{\mathrm{sig}}\cos(\phi) + 2\alpha_{\mathrm{LO}}\left[\cos(\phi)\delta X_{\mathrm{sig}}(t)) + \sin(\phi)\delta Y_{\mathrm{sig}}(t)\right] . \end{aligned} \tag{3.10}$$

Looking at the above equation we see that there are DC and AC signal components. The DC component and the amplitude quadrature noise of the signal arm is proportional to $\cos(\phi)$, whereas the signal phase quadrature is proportional to $\sin(\phi)$. Therefore, by setting the tunable phase difference $\phi = \pi/2$ by locking to the phase for which the DC signal component vanishes, the current $I_{-}(t)$ successfully monitors the phase noise of the signal arm which, in addition, is proportional to the intensity of the strong LO arm. Keeping the phase ϕ constant at the desired value is, once again, a system control problem that can be solved by a PID feedback loop as discussed in Section 3.1.1.

3.2 Experimental measurement setups

To successfully readout membrane mechanics under cavity optical influence, the experimental techniques described in Section 3.1 must be properly implemented while monitoring of all relevant information. Simultaneously, the setup must be isolated from external noise sources which may interfere with measurement outcomes. In this section, the experimental setup aimed to accomplish this is presented. A more detailed explanation of the free space optics part of the setup is given in Appendix **??**.

3.2.1 Optical characterization of photonic crystal resonators

The optical response of the devices must be investigated in order to locate the wavelength regime of maximal reflectivity. The relevant quantity to measure is the total device reflectivity, which defines the quality of an optical resonator formed with the devices. To characterize the optical properties an additional setup is used which was designed in a previous work done by Karim Elkhouly [41] and Sushanth Kini [20].

The measurement setup is presented in Figure 3.4 and is designed to monitor the intensity ratio between the light reflected off the device under study and a reference beam.

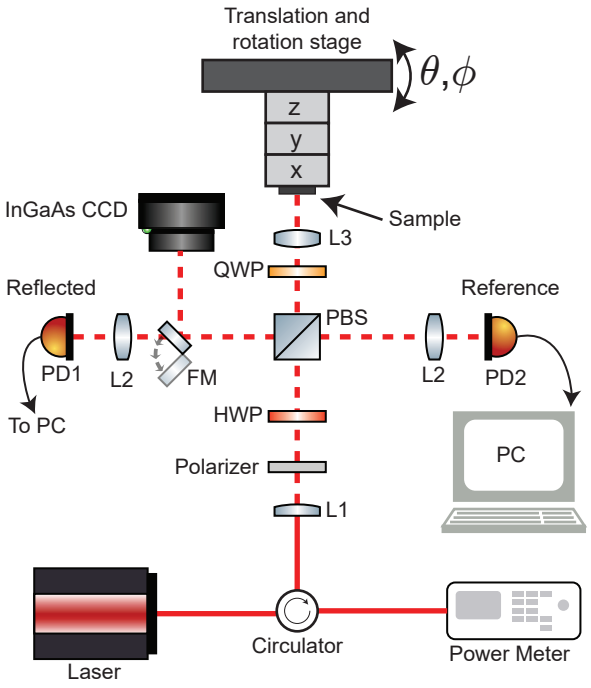

Figure 3.4: Schematic of the reflectivity measurement setup. A tunable laser is sent through a Half Wave Plate (HWP) and PBS to split half of the incoming power to a reference arm and half to the sample. Using a Quarter Wave Plate, the polarization of the reflected light is rotated 90° allowing the reflection to be redirected to the reflection arm. The power of the reference and reflected signals are picked up by two PDs and subsequently monitored by a PC. Figure taken from [20].

Wavelength-dependent reflectivity is recorded by varying the output wavelength of the tunable laser. The results of measurements are normalized to the reflectivity of a silver mirror with a known reflectivity curve. For more information on the setup, see the supplementary information of [20].

3.2.2 Mechanical characterization of photonic crystal resonators

Before investigating how coupling to an intracavity light field affects membrane mechanics, the unperturbed system must first be fully understood. This is done by mechanical characterization using homodyne detection, described in Section 3.1.2. The experimental setup that accomplish this was developed in previous work done by Karim Elkhouly [41] and Sushanth Kini [20].

The setup is presented in Figure 3.5 which adopts the homodyne detection technique to read out mechanics of the micromechanical membranes while placed in a vacuum chamber where pressures drop to $\sim 10^{-4}$ mbar. The device chips can be moved inside the vacuum chamber by using a piezo-actuated translation stage, which allows for sub-micrometer xyz-translations. Using the translation stage, the measurement laser can be focused on the device where mechanics is to be measured. The homodyne signal is read by a balanced photo diode and displayed on a spectrum analyzer (SA).

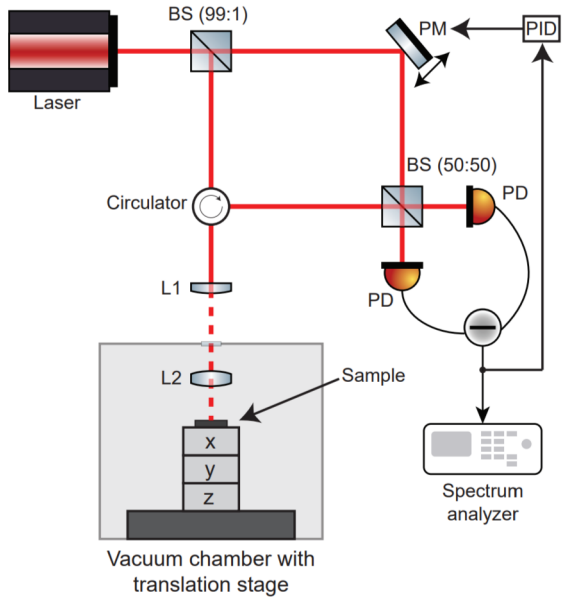

Figure 3.5: Schematic of the mechanical characterization setup. The measurement laser is split up on a 99:1 beam splitter (BS) into signal and local oscillator arms. The signal arm is focused down on the micromechanical membranes placed on a xyz-translation stage in high vacuum ($\sim 10^{-4}$ mbar) to reduce viscous damping. The homodyne signal is generated by mixing the local oscillator and signal arms on a 50:50 beam splitter and reading with a balanced photo diode. The result is displayed on a spectrum analyzer. Figure taken from [20].

The measurement results are displayed as power spectral densities where the harmonic motion of membrane eigenmodes are displayed as peaks in the spectrum, see Section 2.1.1. A typical spectrum is presented in Figure 3.6 where three different traces can be seen. The blue trace represents the noise level of the SA, while the cyan curve shows the electronic noise level in the detector amplifier circuit. Activating the laser output and homodyne detection generates the orange trace, where three membrane mechanical modes are visible above 500 kHz. Lower frequency peaks is assumed to originate from self oscillations in the PID loop which stabilizes the length of the local oscillator arm.

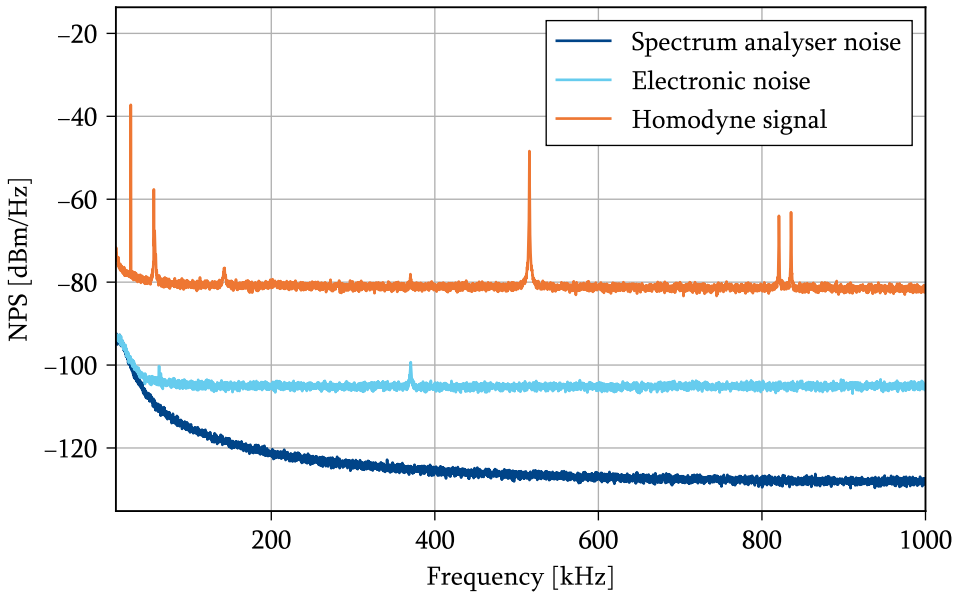

Figure 3.6: Typical noise power spectrums for the mechanical characterization setup. The blue trace represents the noise level of the spectrum analyzer, while the cyan curve shows the electronic noise level in the detector amplifier circuit. Activating the laser output and homodyne detection generates the orange trace where three membrane mechanical modes is clearly visible above 500 kHz.

3.2.3 Optomechanical readout

Presented in Figure 3.7 is the measurement setup performing optomechanical readout. A continuously tunable telecom laser (Toptica CTL 1550-027126) outputs laser in the 1520-1630 nm wavelength range which is split into LO and signal arms by an in-line 50:50 BS. The signal arm is phase modulated in an in-line Electro Optical Modulator (EOM, iXblue MPZ-LN-10) before getting coupled to free space for mode matching to the cavity. The cavity reflection is redirected by an optical circulator and sent to readout. The readout beam is first split on a Polarizing Beam Splitter (PBS) which, along with a $\lambda/2$-retardation plate, allows for variable power distribution between the PDH and HD loops. This is crucial for keeping the ratio between the LO and signal arms in the correct range as discussed in Section 3.1.2.

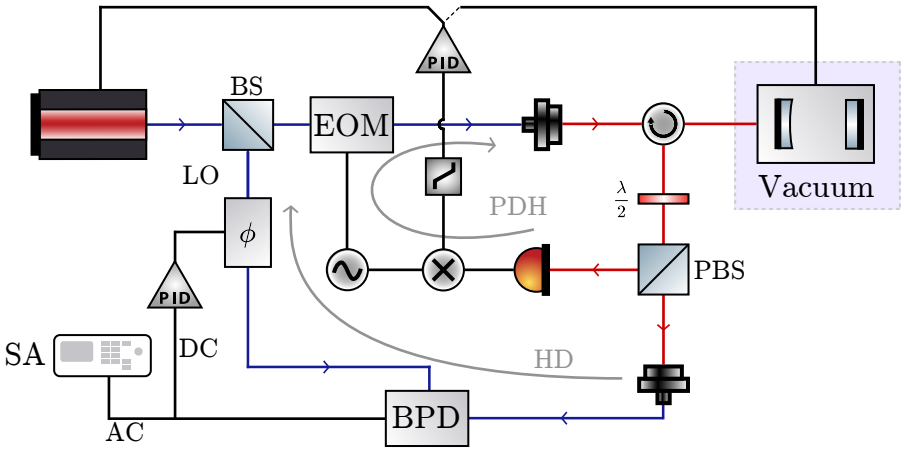

Figure 3.7: Simplified schematic for the experimental setup used to probe the optomechanical system. Blue lines correspond to in-fiber laser propagation, whereas red lines depict free space propagation. The laser output is immediately split up into signal and LO arms for HD readout. The signal arm is phase-modulated before being sent to the cavity. The reflection is split on a PBS for closing both the PDH and HD loops. The phase noise of the signal arm is read out on a Spectrum Analyzer (SA). EOM = Electro Optical Modulator, BPD = Balanced Photo Diode, BS = Beam Splitter.

The PDH loop is closed by detecting the laser power on a PD and feeding the output to a mixer where it is demodulated by the signal generator driving the EOM (Keysight 33500B). The demodulated signal is fed to a PID which controls the laser wavelength output (Toptica DLC pro) or the cavity piezo (Toptica Regulator PID110).

The other output port of the PBS is coupled back into optical fiber and is combined with the LO on a Balanced Photo Diode (BPD) which converts the current $I_{-}(t)$ into a voltage. The homodyne signal containing the phase noise of the signal arm is both monitored on a Spectrum Analyzer (SA, Keysight MXA N9020B) and sent through a PID (Toptica Regulator PID110) to control the in-line variable phase ϕ of the LO.

3.2.4 Cavity optical mode matching

As discussed in Section 2.2.3, a high finesse cavity operates as both a spatial and spectral filter. This fact implies that for the cavity resonant mode to be excited by an external light source, the spectral and spatial conditions of the cavity must be met. An input optical field which deviates from the spatial mode of the cavity will be decomposed into the basis modes of the cavity and therefore only part of the input power will be resonant with the cavity at a given frequency (see Figure 2.6). For a single Hermite-Gauss mode input field to be fully coupled to the corresponding cavity mode, perfect mutual alignment between the modes is required. The alignment can be broken down into three conditions required for the input optical field:

- optical axis transverse aligned to cavity optical axis,
- position of focus along optical axis matched to cavity resonant mode,
- size of focus matched to cavity resonant mode.

Failure to reach the above stated conditions will split the input power into several spatial modes, thus wasting optical power [42].

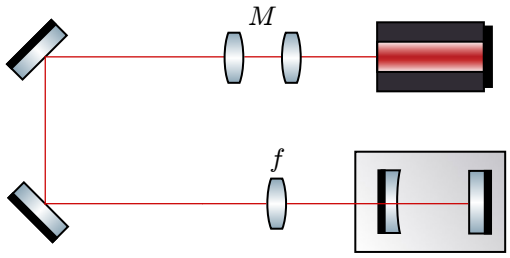

Figure 3.8: Cavity mode matching setup. The input mode size at the cavity back mirror is controlled with a telescope with magnification M and a focusing lens with focal length f. The transverse and angular alignment of the input beam is controlled with two adjustable mirrors.

To satisfy the above conditions of the resonant cavity mode, a mode matching setup is used. The principles of the setup are presented in Figure 3.8. A single-mode output laser that excites the fundamental Gaussian mode (2.37) is coupled to free space for further mode manipulation. The coupling between single-mode fiber and free space is performed by a Triplet Collimator (TC12APC-1550) which outputs a collimated beam with radius 1.135 mm. To achieve angular and transverse alignment of the input field two mirrors mounted on sensitive adjustable mirror mounts are used. To match the radius of the cavity resonant mode, calculated to be 25 μm, a telescope with magnification $M = 3$ is used along with a focusing lens with $f = 150$ mm. The focal distance of the focusing lens is lower bounded by the cryostat geometry that does not easily allow for additional optical components in the sample chamber. With such a weak focusing lens, a large input beam is required to achieve the desired focus at the cavity back mirror. This is not beneficial due to risks of clipping losses on free space optical components. This can be avoided by integrating a small diameter focusing lens that can fit inside the cryostat sample chamber in a future setup.

3.2.5 Imaging

As discussed in previous sections, the size of the intracavity mode as well as the micromechanical membranes are in the ~ 10 μm range which sets the scale on the alignment conditions when investigating a certain membrane on a chip. To decide on which device to perform measurements, proper imaging has to be implemented which allows for monitoring the intracavity mode. This is a challenge due to the samples being positioned behind the incoupler mirror of the cavity. However, the anti-reflection (AR) coating of the incoupler

mirror has its high reflectivity band in the telecom wavelengths and is thus partially transparent in the visible spectrum. This allows for using a camera to monitor the devices inside the cavity. To achieve good image quality inside the cavity on the μm range a

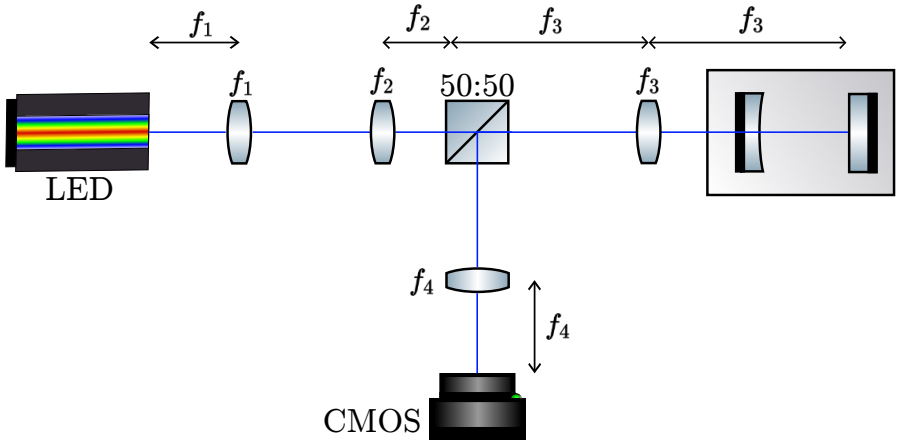

Figure 3.9: Imaging setup using Köhler illumination. A white light source (LED) is collimated by f_1 and subsequently focused by f_2 onto the back focal plane of f_3. The focusing lens f_3 collimates the image of the sample which is finally focused by the objective lens f_4 on the Complementary Metal Oxide Semiconductor (CMOS) camera.

telescope with Köhler illumination is used, the principles of which is shown in Figure 3.9. A white light LED is used to uniformly illuminate the sample inside the cavity. This is achieved by first collimating the output of the LED with the lens f_1 and then focusing on the back focal plane of f_3 using f_2. This creates a collimated light beam which uniformly illuminates the sample. The image of the sample is then collected by f_3 and redirected through the 50:50 BS into the objective lens which focuses the image on the objective. The image is picked up by a Complementary Metal Oxide Semiconductor (CMOS) camera. The magnification M of this setup is defined by the lenses f_3 and f_4 and is given by

$$M = \frac{f_4}{f_3}\,. \tag{3.11}$$

Because of the CMOS' insensitivity to telecom wavelengths which is used for mechanical readout, the optical mode inside the cavity is not visible on the images. To solve this issue, an additional laser is used which helps with orientation on the sample chip. The laser is inserted into the fiber path of the signal arm before being coupled to free space using a wavelength division multiplexer. The additional laser is a 980 nm LED with variable output power. Due to the extensive free space optical path, optimized for 1550 nm, (see Appendix A) the orientation laser is heavily attenuated due to scattering and requires high input power for the CMOS to pick up a readable signal.

In the current setup, the focusing lens f_3 is multi-purposed, providing both focus for

the imaging and the right mode matching conditions of the cavity coupling. Due to the difference in wavelength, (telecom and visible) the optical components cannot be optimized for all purposes. In this setup, the measurement setup is prioritized, and the lens f_3 is thus AR coated for 1550 nm, which will cause reflections in the visible spectrum. The effective focal distance of the lenses will also vary between the arms due to the frequency dependent index of refraction of the fused silica lenses. In addition, the 1550 nm optimized incoupler mirror will induce aberrations in the image as well as additional reflections. The effect of this is a partly compromised image quality with a lot of potential improvements such as filtering the white light to reduce unwanted reflections.

3.3 Optomechanical system design

In this section, I introduce the designs of the optical and mechanical systems that are used throughout all measurements. We first present the GaAs micromechanical resonators made from AlGaAs heterostructures and finish with introducing the 10 mm long hemispheric Fabry-Pèrot cavity in which the devices can be integrated to form the optomechanical system.

3.3.1 Fabrication of high quality micromechanical resonators

The micromechanical systems used in this work are fabricated from AlGaAs heterostructures and are designed for high mechanical quality factors and optical reflectivities. The manufacturing process begins by epitaxially growing an AlGaAs heterostructure on a GaAs substrate using molecular beam epitaxy (MBE). Firstly, a sequence of AlGaAs, GaAs layers are grown to create a Distributed Bragg Reflector (DBR) optimized for high reflectance at telecom wavelengths. Next, a 730 nm thick AlGaAs sacrificial layer is grown on top of the DBR. Lastly, the 100 nm device layer of GaAs is grown, which completes the heterostructure. For wafers with double layer devices, another sequence of sacrificial-/device layers is grown on top of the structure. The thickness of the sacrificial layer is chosen to achieve a transmissive stack of reflectors [17]. Following the MBE, the PhC

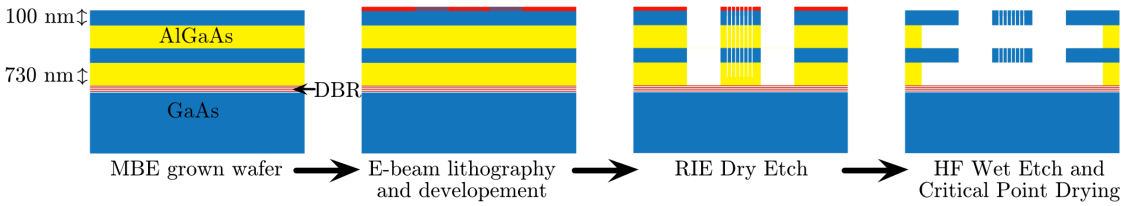

Figure 3.10: The process used to fabricate the GaAs PhC membranes on an epitaxially grown AlGaAs heterostructure. Courtesy of Sushanth Kini.

membranes are patterned onto the 100 nm thick GaAs layers. The finished devices are circular, suspended GaAs membranes varying in size from 50 to 77 μm in diameter. The devices are fabricated by the process shown in Figure 3.10. The wafer is first spin-coated

with resist (red) on which the device patterns are exposed using electron beam lithography. The first etching process is a Reactive Ion Etching (RIE) where the devices are etched into the upper layers of GaAs. After etching, the top resist is removed with a chemical remover (MICROPOSIT Remover 1165). Next, the sacrificial layers are removed with a Hydroflouric (HF) acid based wet etch. Etch remnant salts such as AlF and AlHO on the device is removed by cleaning the sample in potassium hydroxide (KOH). The last fabrication step is drying the sample with CO_2 critical point drying, which protects the membranes from collapsing due to surface tension forces while drying. The PhC pattern is optimized for a high reflectivity in the 1520-1540 nm wavelength range by choosing appropriate PhC lattice constant and hole radius. The lattice has a square structure with lattice constant $a = 1081$ nm and radius $r = 455.5$ nm.

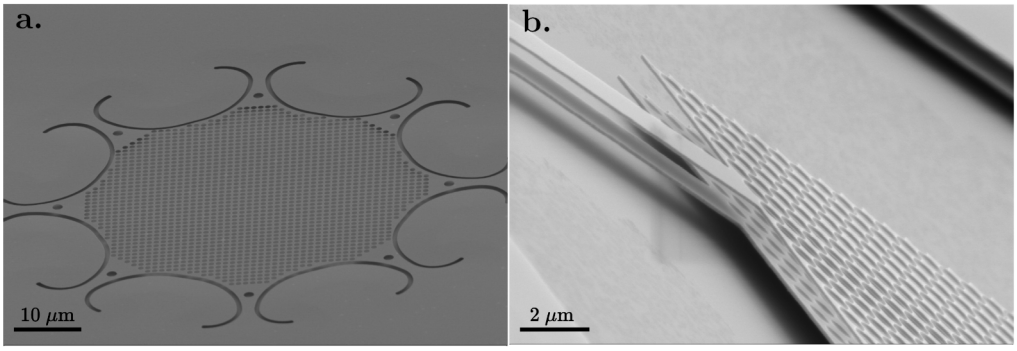

Figure 3.11: **a.** Tilted SEM image of a 100 nm thick suspended GaAs membrane attached to the surrounding substrate by eight tethers. **b.** Side view of a stack of GaAs suspended double layer rectangular membranes with a vertical separation of ~ 732 nm. Courtesy of Sushanth Kini and Anastasiia Ciers.

3.3.2 Optical cavity design

The optical cavity used during this work is a monolithic copper structure designed for mechanical rigidity to provide stable optical resonances. A cross-section view of the cavity is presented in Figure 3.12. The laser enters from the left and encounters the spherical fused silica incoupler mirror. The left (right) side of the mirror is anti- (high) reflection coated for telecom wavelengths. The total losses through transmission and scattering of the high reflectivity coating for telecom wavelengths is $\sim 10 - 20$ ppm.

Next, the laser encounters the 5×5 mm^2 AlGaAs sample containing a matrix of etched membrane devices, see inset **a.** of Figure 3.12. The surface of the sample is on a distance $L = 9.84$ mm from the incoupler mirror, which allows for calculating the spotsize of the intracavity Gaussian mode according to (2.36). Given the radius of curvature $r = 10$ mm of the incoupler mirror and a laser wavelength of 1550 nm, the radius of the intracavity focus is calculated to $w = 25$ μm, which is in the same length scale as our devices. However,

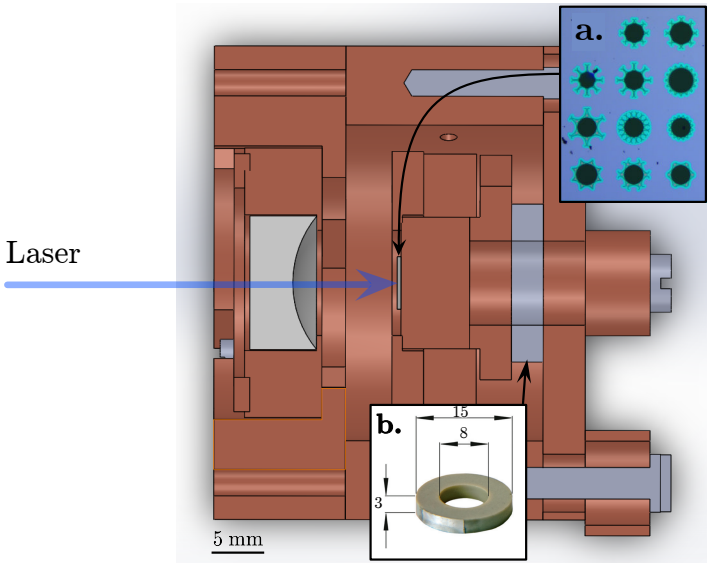

Figure 3.12: Cross-section view of the monolithic optical cavity design. The laser input enters from the left and impinges on the Ø= 12.7 mm incoupler mirror (light gray). The light entering the cavity focuses down on the sample chip (dark gray) which is clamped to a copper adapter. The copper adapter is in turn glued along with a ring piezo actuator (blue gray) to the cavity back wall. Insets: **a.** Optical micrograph of device matrix **b.** Ring-piezo controlling the cavity length, length unit = mm.

due to the Gaussian nature of the beam, clipping losses $\mathcal{L}_{\text{cl}}$ are introduced [43]

$$\mathcal{L}_{\text{cl}} = e^{-2\frac{D^2}{(2w)^2}}, \tag{3.12}$$

where D is the diameter of the membrane. For membranes studied the diameter is $D \approx 80$ μm which gives $\mathcal{L}_{\text{cl}} \approx 6000$ ppm. Note that this assumes that the field exceeding the extent of the membrane vanishes, which most likely is not the case for our samples due to the reflectivity of the underlying DBR. However, phase differences in the field reflecting of the devices and sample substrate can induce similar losses.

The length of the cavity can be controlled electronically with the use of a piezo-electric ring, see inset **b.** of Figure 3.12, that connects the sample adapter and the back of the cavity. Connecting the piezo to a voltage source allows for scanning the cavity length by up to ~ 4 μm at room temperature.

The back wall of the cavity is clamped onto the body of the cavity with four M3 screws with concentric springs. The springs keep the back wall fixed to the cavity along the optical axis of the incoming light. However, extra screw clearance in the back wall allows for transverse movement of the back wall, offering a way of choosing between devices on sample chips.

The cavity is placed within an attoDRY800 cryostat to allow for high vacuum environments, which reduces viscous damping of the membrane mechanics caused by atmospheric molecules. During experiments, the pressure in the chamber is $\sim 10^{-4}$ mbar. The cryostat can also be used to cool down the optomechanical cavity to cryogenic temperatures of ~ 4 K. This was however not the focus of this thesis.

4. Results

This thesis is centered on implementing the first steps towards realizing an optomechanical system with micromechanical multi-element resonators. This chapter presents the measurement results for the optical and mechanical properties of the devices. Furthermore, I discuss the results gathered with the optomechanical setup. The performance of the optomechanical system is analyzed and improvements are discussed.

4.1 Suspended photonic crystal structure resonators

The suspended GaAs membranes are an integral part of both the optical and mechanical degrees of freedom in our optomechanical system. Thus individual membrane properties must be well known before they are integrated into a macroscopic optical cavity for optomechanical readout. In this section, the optical and mechanical characterization of two devices are presented. Scanning electron micrographs of the considered geometries are shown in Figure 4.1 . Panel **(a)** shows a Single-Layer (SL) device on top of a DBR mirror whilst panel **(b)** depicts a Double-Layer (DL) device. The diameter of the devices are 77 μm for SL and 80 μm for DL, respectively. The DL device is not fabricated on top of a DBR mirror and thus only has an underlying GaAs substrate. This is a crucial difference between the two samples which will become apparent in the optical characterization of the devices. Part of the characterization data was gathered before the start of this thesis and is credited to Sushanth Kini and Anastasiia Ciers.

4.1.1 Optical characterization

As seen in Section 2.2.1, a high finesse optical cavity is formed from two highly reflective mirrors. High finesse cavities show narrow linewidths κ which, along with high mechanical frequency, would allow to reach the sideband resolved regime of optomechanics and achieve efficient sideband cooling of mechanical modes. If sideband resolution is not achieved, feedback cooling can be utilized to reach the quantum ground state of motion. Regardless of sideband resolution, knowing the reflectivity of the devices is crucial to being able to avoid impedance mismatch for the optomechanical cavity. Therefore, the reflectivity of the devices considered for optomechaincal experiments is characterized. The reflectivity spectrum is measured by methods described in Section 3.2.1.

The reflectivity spectra for the considered devices along with a DBR mirror reference sample are presented in Figure 4.2. Solid lines represent measured data, whilst dashed lines

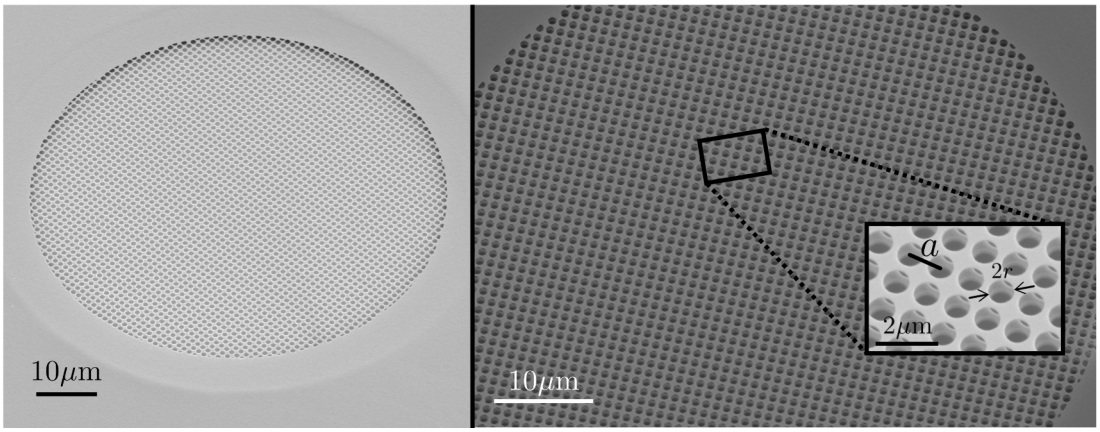

Figure 4.1: Scanning electron micrographs of the characterized device geometries. **(a)** Single-layer circular membrane resonator on top of a DBR mirror. The diameter of the device is 77 μm. **(b)** Double-layer circular membrane device with a diameter of 80 μm. Photonic crystal lattice parameters of the devices are lattice constant $a \approx 1080$ nm and hole radius $r \approx 450$ nm.

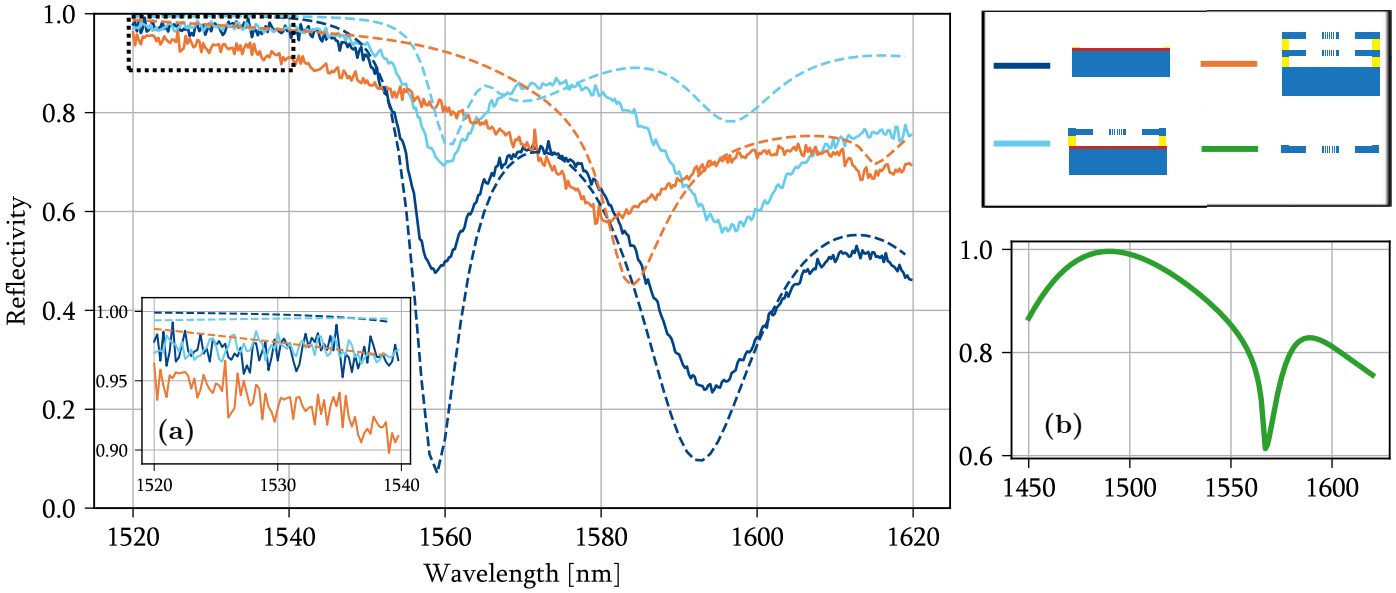

Figure 4.2: Measured (solid) and simulated (dashed) reflectivity for three types of samples. The Distributed Bragg Reflector (DBR, blue) reflectivity is shown as a reference to the Single-Layer (cyan) on DBR. The Double-Layer (orange) device is fabricated on a plain GaAs wafer and does not inherit any DBR characteristics. **(a)** Zoomed in view of the boxed high reflectivity wavelength range of 1520-1540 nm. **(b)** simulated reflectivity for an isolated PhC membrane with geometry matching the SL device membrane.

represent simulated data using S^4. We note that an expected plateau-like characteristic can be seen for the simple DBR mirror for wavelengths in the 1520-1540 nm range. However, the maximum of the DBR reflectivity plateau is shifted towards a lower wavelength range that is not reachable for the used tunable laser. This is a design flaw of the DBR and is attributed to inaccurate growth parameters for the DBR. The simulated spectra capture the overall features of the DBR, but does not agree in magnitude. This can be due to imperfections in the DBR grow or slight deviations in the refractive indices used for simulation. The SL device retains a lot of the features of the underlying DBR, but has a higher reflectivity for longer wavelengths due to extra reflection off the PhC membrane. The simulation shows an additional feature in the spectrum at 1570 nm which is attributed to PhC guided resonances caused by finite sized laser beam waists discussed in [20]. The same feature is shown in the simulated spectrum presented in panel **(b)** of Figure 4.2 that depicts a spectrum for an isolated PhC membrane with equal lattice parameters as the SL device. Lacking the features of the DBR, the DL device on GaAs substrate show two broad dips at 1580 nm and 1615 nm, which can be explained by simulation. The first is attributed to a Fabry-Pèrot cavity forming between the membranes at the given wavelength, whilst the latter is caused by PhC guided resonances.

Due to the high reflectivity of the input mirror of the cavity (for details, see Section 3.3.2) high reflectivity devices is required to avoid impedance mismatch in the mirrors. Attention is therefore turned to the short wavelength range where high reflectivities are shown, see inset **(a)** of Figure 4.2. With the used characterization setup, the measured performance of the SL device and the reference DBR are indistinguishable in this wavelength range. The DL device, however, show slightly lower reflectivities which can be attributed to the lack of an underlying DBR mirror. Due to the superior reflectivity, the SL device is therefore prioritized above the DL device when considering optomechanical effects.

To further increase the reflectivity of the devices, careful engineering of PhC patterns and DBR parameters is required. From inset **(b)** we see that the wavelength of maximum reflectivity for the PhC membranes is reached for $\lambda = 1480$ nm. Shifting that maximum for both the PhC and the DBR into the wavelength range of the used laser might allow for observation of even higher reflectivities. The simulations indicate that the actual reflectivities are even higher than measured. However, the measurement setup does not allow for well resolved reflectivity measurements in the ppm range, which would be required to more accurately specify reflectivities in this range. This can for instance be solved with a setup using a high finesse FP cavity. This will be discussed further in Section 4.2.2.

4.1.2 Mechanical characterization

The figures of merit for a mechanical resonator are the resonance frequency Ω_m, the quality factor $Q_\mathrm{m} = \Omega_\mathrm{m}/\Gamma_\mathrm{m}$ and their product $Q_\mathrm{m} \cdot f_\mathrm{m} = Q_\mathrm{m}\Omega_\mathrm{m}/2\pi$. These parameters affect the level of sideband resolution in the final optomechanical system, as well as the coupling

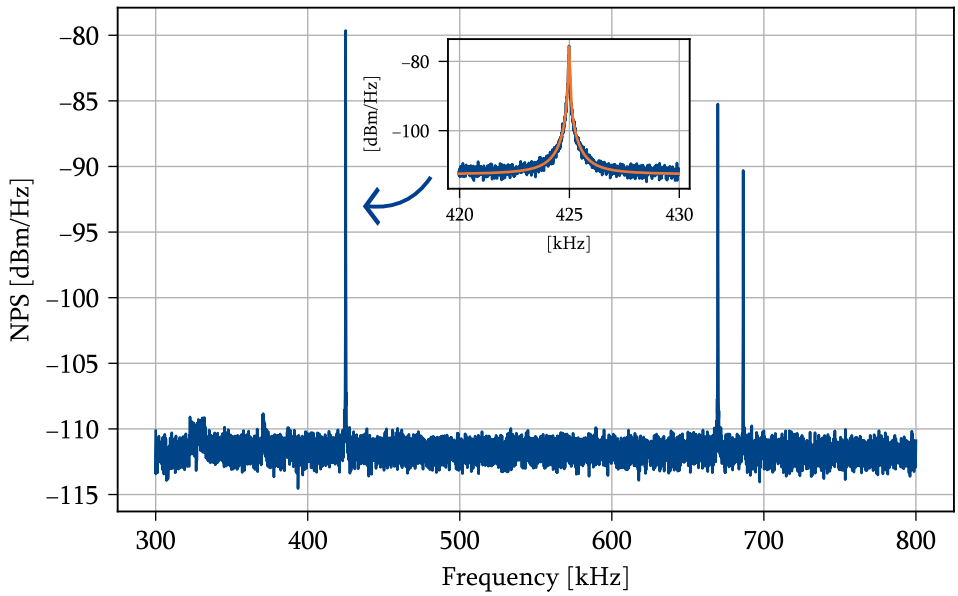

Figure 4.3: Thermal mechanical noise power spectrum (NPS) for a single suspended photonic crystal membrane showing three mechanical modes. Inset depicts a Lorentzian fit to the mechanical mode with $\Omega_m/2\pi \approx 425$ kHz, giving a quality factor of $Q_m = 3.5 \cdot 10^4$.

to the thermal environment. The latter dictates how effective an optomechanical cooling must be to reach a certain level of resonator phonon occupation at a given environment temperature, see Section 2.3.3. We study the mechanical properties of the same single and double-layer devices as in the previous section. The principles and experimental setup used for the characterization are described in Chapter 2 of this thesis.

First, we study the thermal noise power spectrum (NPS) of the SL device, which is presented in Figure 4.3. In the spectrum, three mechanical modes are visible in the given frequency range. The parameters of interested are extracted from the spectrum by fitting a Lorentzian function (2.11) to the excitation peaks. The inset of Figure 4.3 shows a fit[1] to the resonance with $\Omega_m/2\pi = 425$ kHz, which show the greatest quality factor out of the three resonances with a value of $Q_m = 3.5 \cdot 10^4$ yielding $Q_m \cdot f_m = 1.48 \cdot 10^{10}$ Hz. This is on the lower end of $Q_m \cdot f_m$ products that have been achieved with on-chip micromembranes, where values surpassing 10^{12} Hz have been reached that allow to observe the quantum mechanical regime of optomechanics at room temperature [6].

Next, the mechanical properties of the DL device are investigated. The presence of two suspended membranes is apparent due to the increased number of mechanical modes in the NPS presented in panel **(a)** of Figure 4.4. To confirm the presence of two independent membranes, a mode tomography study is performed. The device is swept across the

[1] note the logarithmic y-scale

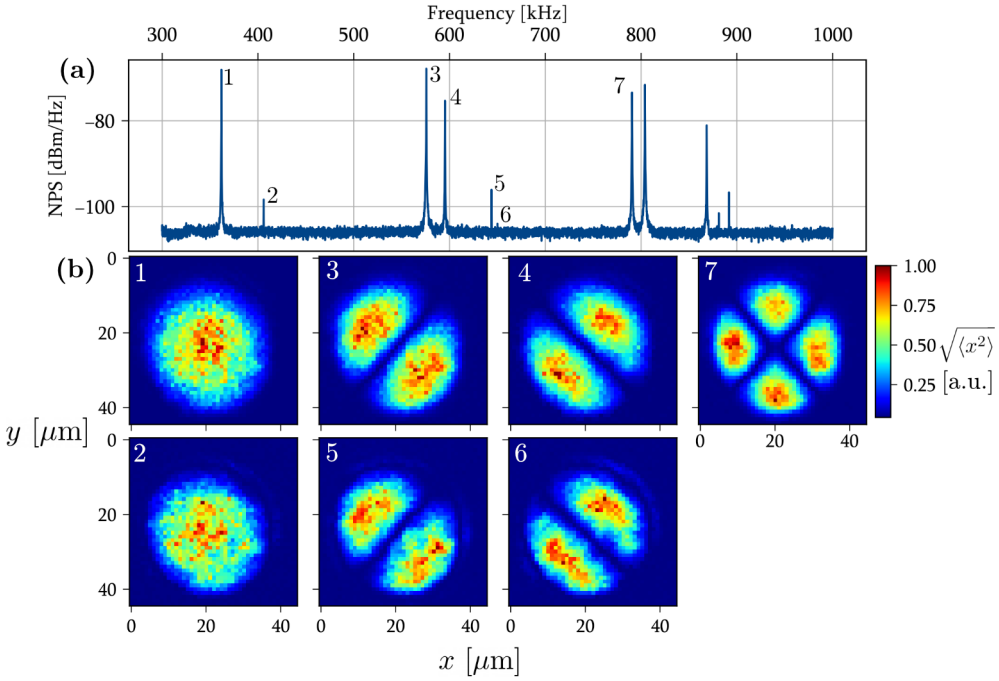

Figure 4.4: **(a)** Thermal mechanical noise power spectrum (NPS) for a double layer photonic crystal membrane stack. The signals originating from the motion of the bottom membrane are significantly weaker due to the reflection of the top membrane. **(b)** Individually normalized mode tomography images of the first 7 modes from the NPS in panel (a). The top (bottom) row corresponds to the modes of the top (bottom) membrane.

measurement laser in a grid and the thermal NPS is recorded at each point. For each NPS, the mean square displacement for a chosen number of modes are calculated by integrating the NPS according to Equation (2.12). Finally, the displacement data for each mode is normalized and shown in a 2D plot presented in panel **(b)** of Figure 4.4. The modes are labelled and connect each individual tomography map with the corresponding mode in the NPS. Notably, multiple copies of the same spatial mode are present with non-degenerate frequencies. Additionally, the second occurrence of the same spatial mode is several orders of magnitude fainter in the NPS indicating that the signal is coming from the lower membrane in the stack. The difference in frequencies between the same spatial mode in the two membranes are most likely due to tensile stress differences in the two membranes. This is caused by lattice constant mismatch between membrane and the sacrificial layer which introduces stress. The resonance frequency of a circular membrane with radius r and density ρ under isotropic stress σ can be modeled by [44]

$$\Omega_{n,j} = \frac{\alpha_{n,j}}{r}\sqrt{\frac{\sigma}{\rho}} \tag{4.1}$$

where $\alpha_{n,j}$ are constants related to the mode (n, j). Note that this assumes that the forces inside the membrane is dominated by stress. Using the ratio between the resonance frequencies of two identical modes in the membranes, an estimation of the stress difference between the membranes can be estimated under the assumption that all other parameters are equal. Using the gathered data, we observe $\sigma_{\text{bottom}} \approx 1.13\sigma_{\text{top}}$. Additionally, using (4.1), we can derive the maximum allowed stress difference between top and bottom membranes for the resonance frequencies to match within their linewidths. Starting from the constraint $|\Omega_{\text{t}} - \Omega_{\text{b}}| < \Gamma_{\text{t}}$ yields

$$\frac{|\Delta\sigma|}{\sigma_{\text{t}}} < 2Q_{\text{t}}^{-1}\,. \tag{4.2}$$

where σ_{t} (σ_{b}) is the isotropic stress of the top (bottom) membrane, $\Delta\sigma = \sigma_{\text{b}} - \sigma_{\text{t}}$ and is only valid for a $Q_{\text{t}} \ll 1$. This is interesting when considering multi-element optomechanics which requires similar frequencies for all resonators in the stack. For this particular DL device, this gives that the relative difference in stress between the top and bottom membranes cannot surpass 57 ppm.

As previously mentioned, the $Q_{\text{m}} \cdot f_{\text{m}}$ products of $\sim 10^{10}$ Hz presented for our membranes does not allow for quantum optomechanics experiments starting at room temperature. This is caused by excess loss mechanisms in the system, where clamping loss and thermoelastic damping are the dominating ones [45]. Reducing losses without sacrificing optical properties of the device is a great challenge tackled by several groups in the field. The reduction of clamping losses in similar on-chip devices has seen great success for groups using highly tensile-stressed SiN membranes [46], [47] presenting $Q_{\text{m}} \cdot f_{\text{m}}$ products $\ll 10^{12}$. In addition, phononic crystal shielding of membranes has been reported to further reduce losses in high frequency resonators [48], [49]. Reaching high tensile stress levels in our devices is however limited by the small lattice mismatch between GaAs and AlGaAs. To

counteract this, materials with large lattice mismatch relative to the AlGaAs sacrificial layer such as InGaP can be considered. These membranes have shown to be feasible for quantum optomechanics with $\Omega_m/2\pi \sim 1$MHz and $Q_m \cdot f_m$ products of $2 \cdot 10^{12}$ which can offer an alternative route to multi-element optomechanics [50]. The increased mechanical frequency shown for InGaP devices is also beneficial for optomechanical sideband resolution. With frequencies for our devices in the 100 kHz regime, high quality optical cavities are required for sideband resolution putting additional constraints on the device reflectivities, see Section 4.2.2.

4.2 Optical cavities

The macroscopic 10 mm long cavity presented in Section 3.3.2 offers a way to fully integrate the AlGaAs samples presented in previous section into an optomechanical system. In this section, we investigate the optical properties of the cavity with the SL device seen in Figure 4.1 as back mirror. However, before inserting the devices, a symmetric cavity is investigated to specify the properties of the input mirror which is kept constant for all experiments.

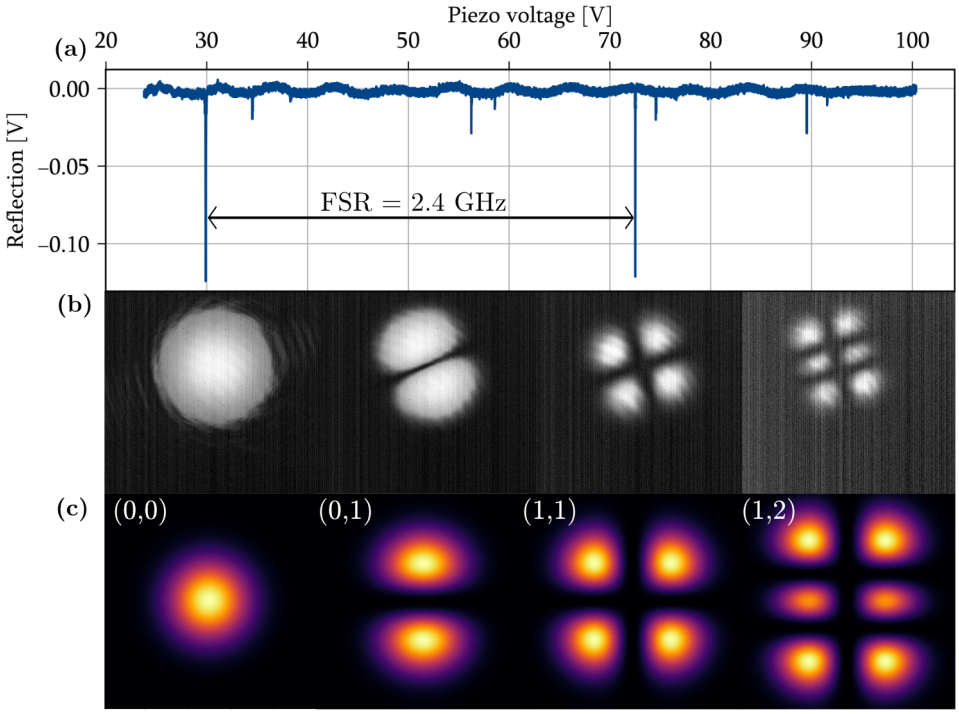

Figure 4.5: **(a)** Typical cavity reflection signal as a function of applied piezo voltage. The repeating pattern in cavity resonant modes indicate the free spectral range. **(b)** CMOS images of cavity transmission at different cavity lengths. **(c)** Corresponding Hermite-Gauss calculations according to (2.38) with indicated indices (l, m).

4.2.1 Bare cavity

To isolate the properties of the input mirror we first study a symmetric cavity without micromechaincal membranes. During these tests the back mirror is a flat fused silica mirror provided by Layertec with identical HR coating as the input mirror ($T \approx 8$ ppm). This symmetric case is considered as a reference system when later analyzing the performance of our fabricated samples. The back side of the flat Layertec mirror is anti reflection coated for 1550 nm allowing for cavity transmission to be analyzed in addition to reflection. The incoming laser at 1550 nm is mode matched to the intracavity mode while using the cavity ring piezo to alter the cavity length. The reflection is recorded on a photodiode and displayed on an oscilloscope. A typical cavity reflection as a function of applied piezo voltage with partial mode matching is shown in panel **(a)** of Figure 4.5. When the resonance condition of the cavity length is met, light is allowed to pass through, reducing the reflected signal. The imperfections in mode periodicity seen between two FSR's are assumed to originate from non-linearities in the piezo displacement response. When a mode resonance condition is fulfilled, the cavity transmission is picked up by a CMOS camera which shows the spatial distribution of the intracavity field. Panel **(b)** of Figure 4.5 shows the captured cavity transmission at four different resonance conditions for the cavity length. The Hermite-Gaussian spatial distribution of the intracavity field at each resonance is observed and compared to the corresponding calculations of (2.38) in panel **(c)** of the same figure.

4.2.2 Finesse characterization

As for the mechanical resonators characterized in Section 4.1.2, the optical resonator, *i.e.* the cavity, has energy dissipation defined by the spectral linewidth κ of the resonant mode. This is a fundamental parameter of the optomechanical system and must therefore be characterized. The linewidth κ is found by observing individual modes in the cavity reflection when scanning parameters such as laser frequency or cavity length. The frequency axis scale in such measurements is found by modulating sidebands to the incident laser with a well-defined modulation frequency. This can be achieved by phase modulation, as shown in Equation (3.4). The separation between the carrier wave and the sidebands along with the modulation frequency defines the frequency axis of the recorded signal. This principle is presented in Figure 4.6 where the cavity reflection of a sideband modulated signal with a modulation frequency of 25 MHz is depicted. With the frequency axis calibrated, the cavity linewidth κ can be determined from (2.33) with a Lorentzian fit. Inset **(a)** in Figure 4.6 shows a measurement of piezo non-linearities. The relative position of the sidebands to the carrier is plotted in time domain versus frequency domain. A linear fit indicates that a linear relation between applied piezo voltage and displacement can be assumed for the relevant voltage span. Note however that this can not be assumed for large voltage spans, as indicated in panel **(a)** of a 4.5.

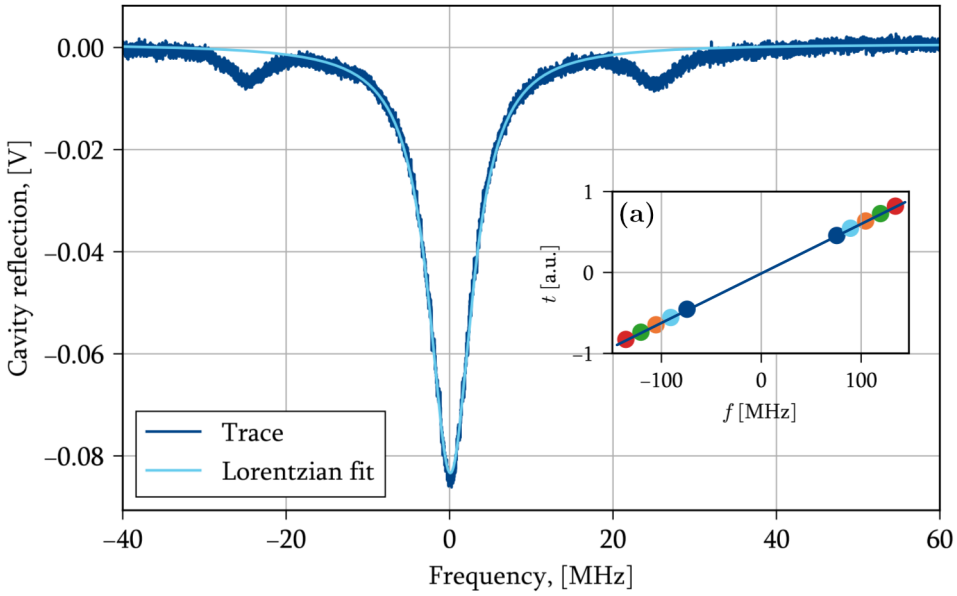

Figure 4.6: Reflection frequency response of a cavity with an SL PhC membrane on DBR as back mirror. The incident laser is phase modulated at 25 MHz, showing clear sidebands to which the frequency axis is calibrated. A Lorentzian fit (not accounting for the sidebands) is used to determine the linewidth κ. **(a)** Piezo linearity measurement. Relative position of the sidebands plotted for time and applied modulation frequency.

Using the presented analysis, the finesse of cavities with four different back mirrors are determined:

1. Layertec HR coated fused silica mirror,
2. AlGaAs DBR mirror,
3. SL device substrate,
4. SL device.

Due to the lower reflectivity of the DL structure and time limitations, cavity properties with DL devices were not investigated further. From the results in Section 4.1.1, the fabricated AlGaAs device shows a high reflectivity for incident wavelengths in the 1520-1540 nm band. Thus, for all following measurements involving the devices, the wavelength is set to 1520 nm.

For the case of the bare cavity, equal reflectivities for the two mirrors are assumed. This allows for an estimation of the incoherent surface losses $\mathcal{L}$ of the two mirrors. Assuming an amplitude reflection of $\sqrt{R(1-\mathcal{L})}$ for the intracavity field reflecting off both inner cavity walls, the cavity roundtrip attenuation factor takes the form

$$g_m = R(1-\mathcal{L})\,. \tag{4.3}$$

Using this expression in Equation (2.32) and fitting to the cavity resonance yields $1-R \approx$ 3.8 ppm and $\mathcal{L} \approx 13$ ppm for the Layertec mirrors. The high losses are attributed to surface losses on the $r = 10$ mm curved mirror due to its large curvature ($r = 10$ mm).

The losses and reflectivities of the AlGaAs samples can in principle be found with the same analysis when knowing the reflectivity and losses of the input mirror. This was however not possible due to additional loss effects such as improper mode matching restricting the $(R, \mathcal{L})$ parameter space while fitting. However, assuming a lossless cavity allows to calculate the reflectivity of the second mirror from Equation (2.28) which gives an estimate of the reflectivity of the back mirror when neglecting any additional losses $\mathcal{L}$. The results of both finesse and reflectivity estimations are presented in Table 4.1 along with simulated reflectivities for the DBR mirror and the SL device at $\lambda = 1520$ nm, taken for from Section 4.1.1.

The results show finesse values surpassing 10^3 for all configurations with linewidths in the 1 MHz range for the AlGaAs samples. We observe a two orders of magnitude drop in finesse for the AlGaAs samples compared with the reference cavity. This drop is attributed to lower reflectivities on the AlGaAs samples. The finesse of the cavity formed with the SL device shows a lower finesse than with the sample substrate. This is interesting due to the sample substrate not being optimized in terms of reflectivity having additional layers of unpatterned GaAs/AlGaAs on top of the DBR mirror. This decrease in finesse can be attributed in part to excess clipping of the intracavity mode on the surrounding substrate, see Figure 4.8. The reflection of this light can interfere destructively with the light reflecting off the PhC membrane due to differences in phase change of the two reflections. However, from the simulated reflectivity data, the reflectivity of the SL device seem to perform better than expected. This can be explained by deviations between simulation and reality in photonic crystal lattice parameters.

End mirror	Layertec	DBR	SL sample substrate	SL device
$\kappa/2\pi$ [kHz]	80 ± 10	2053 ± 3	3700 ± 100	6380 ± 80
$\mathcal{F}$	$1.8 \cdot 10^5 \pm 0.2 \cdot 10^5$	7420 ± 10	4100 ± 100	2370 ± 30
1 - R [ppm]	3.4 ± 0.4	840 ± 4	1520 ± 40	2620 ± 10
1 - R_{S^4} [ppm]	–	831	–	4877
$\mathcal{L}$ [ppm]	13 ± 2	–	–	–
I_{rel} [%]	40	6	1	0.5

Table 4.1: Cavity parameters for four different cavity configurations. Reflection and incoherent surface losses for the Layertec mirror are estimated with Equation (2.32) while a lossless cavity is assumed for the AlGaAs samples. The less informative model gives a rough estimation for the sample reflectivities. For AlGaAs heterostructure growth parameters, see Section 3.3.1.

From an optomechanical viewpoint, the linewidth of the cavity observed for the SL PhC membrane device does not allow for sideband resolution given mechanical frequencies in the 100 kHz range. This reduces the lowest phonon occupation accessible with sideband based optomechanical cooling as seen in Section 2.3.3. However, even in the non-sideband resolved case, mechanical mode cooling can still be performed using feed-back cooling which has been demonstrated by several teams. In the case of micromechanical membranes, measurement based feedback cooling to the quantum ground state was demonstrated by Rossi *et al.* in 2018 [51].

To achieve higher finesse for our system, the loss mechanisms discussed above must be reduced. To reduce clipping losses, larger membrane designs can be considered. Using the assumed values for the cavity mode waist $w = 25$ μm and membrane diameter $D = 77$ μm, we estimate clipping losses $\mathcal{L}_{\text{cl}} = 8710$ ppm from Equation (3.12). This value is considered to be approximate since the waist size is highly sensitive for cavity lengths approaching the radius of curvature for the cavity input mirror, see Equation (2.36). In the future, by increasing the membrane diameter, a reduction of clipping loss can be achieved. Figure 4.7 plots clipping loss $\mathcal{L}_{\text{cl}}$ as function of device diameter D for three different intracavity mode radii. To assure clipping losses $\mathcal{L} < 1$ ppm for the current cavity mode size ($w = 25$ μm), device diameters greater than 135 μm are required.

From the reflectivity results in Section 4.1.1 we see that the SL device gives similar reflectivity to the DBR mirror. The reflectivity measurement is performed with a spot size of $w = 4.6$ μm and thus have negligible clipping losses. We can thus assume that by avoiding clipping losses for the SL devices, performances equal to the DBR sample can be expected. Additionally, increasing the reflectivity of the devices will also affect the finesse. Shifting the point of maximum reflectivity for both the DBR and the PhC membrane into the range of the laser will improve reflectivity of the stack, increasing the finesse of the cavity.

4.3 Cavity frequency lock

With the mechanical and optical degrees of freedom characterized, attention is turned to observe optomechanical effects. As discussed in Chapter 3, two PID servos are required for the experimental setup. The purpose of the servos is to stabilize the output signal when fed error signals generated by the optomechanical system. When done correctly, this allows for stable and accurate readout. In this section, we discuss challenges encountered in the laser-cavity frequency lock.

4.3.1 Cavity impedance mismatch

To successfully lock the laser frequency to the cavity resonance, an error signal with high signal-to-noise (SNR) ratio is required. In both frequency locking schemes presented in

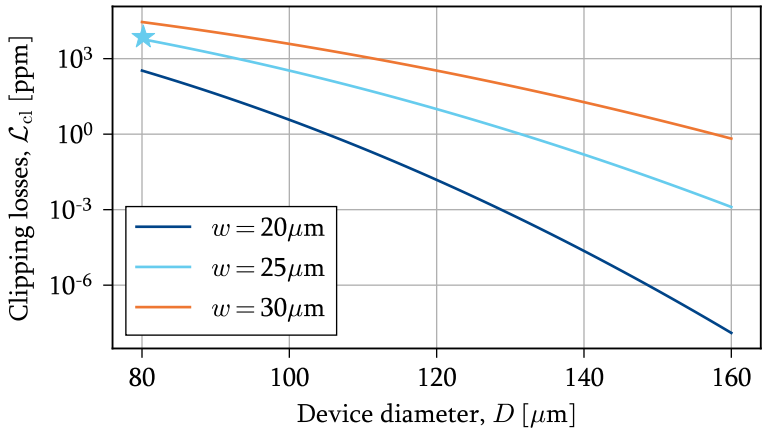

Figure 4.7: Calculation of clipping losses for three waist sizes as function of device diameter D. Cyan star indicates the approximate operating point for the SL device cavity.

Section 3.1.1, the SNR of the error signal is in part defined by the SNR of the cavity resonance signal. Parameters that limit the optical intensity of the cavity resonance are scattering loss, improper mode matching and cavity mirror impedance mismatch. To analyze these effects, we look at the relative reflected intensity on resonance

$$I_{\mathrm{rel}} = 1 - \left.\frac{I_{\mathrm{refl}}}{I_{\mathrm{in}}}\right|_{\omega=\omega_{\mathrm{cav}}} . \tag{4.4}$$

Here, I_{refl} and I_{in} are the reflected and input intensities respectively. The data for the four cavity configurations are presented in Table 4.1. In theory, the lossless symmetric cavity yields $I_{\mathrm{rel}} = 100$ %, however the symmetric HR Layertec cavity shows a resonance with $I_{\mathrm{rel}} \sim 40$ % explained by the internal losses $\mathcal{L} \approx 14$ ppm calculated in the previous section. For the AlGaAs samples we see a large drop in resonance with $I_{\mathrm{rel}} = 0.5$ % for the SL device. For this asymmetric case, impedance matching of the cavity mirrors is crucial in yielding strong cavity resonances. Using equation (2.32) we calculate I_{rel} for two mirrors with reflectivities R_1 and R_2. The reflection of mirror one is fixed while R_2 is swept over several orders of magnitude, the results are shown in Figure 4.8.

We conclude that the impact of slight impedance mismatch of the cavity mirrors is stronger for mirrors with high reflectivity. Thus, the reflectivity of the input mirror greatly constricts the reflectivity range for the back cavity mirror in which a strong cavity resonance is achieved. The drop in cavity resonance for the AlGaAs samples makes the error signal used for frequency locking more susceptible to excess noise sources.

4.3.2 Laser intensity noise

One source of noise studied here is intensity noise inherent to the laser. Laser intensity noise is lower bounded by shot noise which is a quantum effect that can be described by the stochastic nature of photon occurrences on a measurement device such as a photo

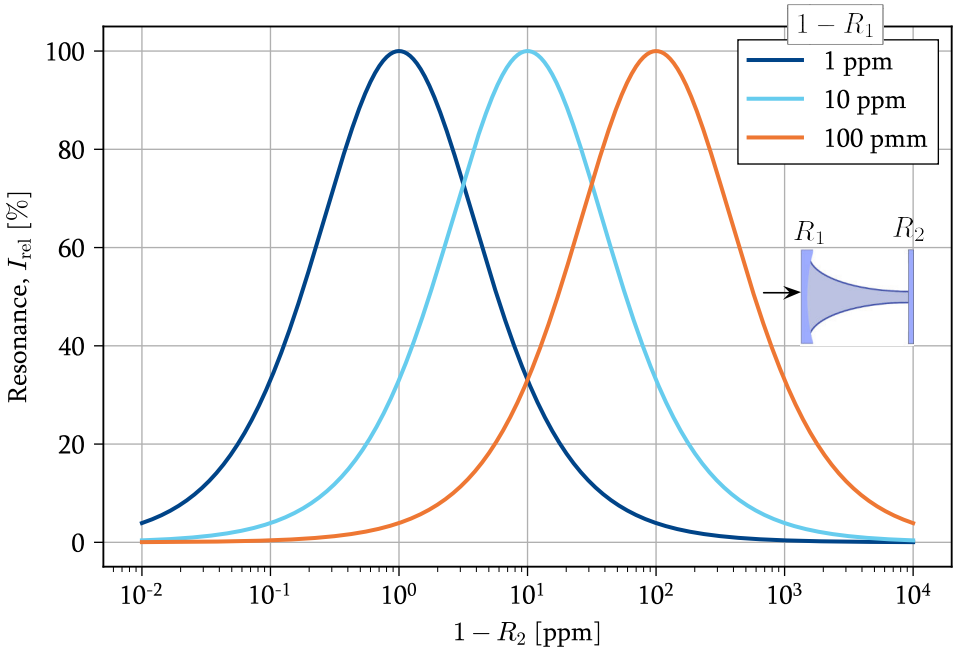

Figure 4.8: Cavity resonance for different impedance mismatch. The reflectivity R_2 is varied over a logarithmic scale whilst R_1 is fixed to the indicated values. Strong resonance is achieved if $1 - R$ of the two mirrors are matched within one order of magnitude.

diode. This noise is independent of frequency, *i.e.* white noise, and is linearly proportional to the laser power P. However, excess intensity noise in the electric field of the laser scales quadratically with P. This type of noise is commonly seen for laser outputs in lower frequency regimes and originates from external sources such as electrical noise in the injection current or relaxation oscillations.

For a steady state laser output, the optical power $P_{\mathrm{opt}}(t)$ can be described by

$$P_{\mathrm{opt}}(t) = \bar{P}_{\mathrm{opt}} + \delta P_{\mathrm{opt}}(t) \tag{4.5}$$

where $\delta P_{\mathrm{opt}}(t)$ is the power fluctuations around the mean value $\bar{P}_{\mathrm{opt}}$. The statistics of the optical power fluctuations are commonly studied relative to $\bar{P}_{\mathrm{opt}}$ by looking at the power spectrum of the Relative Intensity Noise (RIN) defined as

$$S_{\mathrm{RIN}}(\omega) = \frac{2}{\bar{P}_{\mathrm{opt}}^2} \int_{\infty}^{\infty} \langle \delta P_{\mathrm{opt}}(t) \delta P_{\mathrm{opt}}(t+\tau) \rangle \mathrm{e}^{-i\omega t} \mathrm{d}\tau \,. \tag{4.6}$$

For a laser with frequency ω_l and average power $\bar{P}_{\mathrm{opt}}$ operating at the shot noise limit we have $\langle \delta P_{\mathrm{opt}}(t) \delta P_{\mathrm{opt}}(t+\tau) \rangle = \hbar\omega \bar{P}_{\mathrm{opt}} \delta(\tau)$ due to the white noise statistics which gives the RIN shot noise limit as

$$S_{RIN,SN}(\omega) = \frac{2\hbar\omega_l}{\bar{P}_{\mathrm{opt}}} \tag{4.7}$$

Which serves as the RIN limit for laser light.

When using a photodiode amplified by a transimpedance amplifier to measure the optical power on an oscilloscope, the relation between optical power and measured voltage is linear and is given by

$$V(t) = \eta S G P_{\mathrm{opt}}(t), \tag{4.8}$$

where S is the photosensitivity of the photo diode and G is the transimpedance gain and η is photo diode efficiency. This relation allows us to study the RIN of the laser by measuring the relative noise in the detected output voltage. We thus have

$$\begin{aligned} S_{\mathrm{RIN}}(\omega) &= \frac{2}{\bar{P}_{\mathrm{opt}}^2} \int_{\infty}^{\infty} \langle \delta P_{\mathrm{opt}}(t) \delta P_{\mathrm{opt}}(t+\tau) \rangle \mathrm{e}^{-i\omega t} \mathrm{d}\tau \\ &= \frac{2}{\bar{V}^2} \int_{\infty}^{\infty} \langle \delta V(t) \delta V(t+\tau) \rangle \mathrm{e}^{-i\omega t} \mathrm{d}\tau = \frac{S_{VV}(\omega)}{\bar{V}^2}\,, \end{aligned} \tag{4.9}$$

where $S_{VV}(\omega)$ is the NPS of the measured voltage signal $V(t) = \bar{V} + \delta V(t)$. This can be easily accessed by measuring the voltage output of the transimpedence amplifier with a spectrum analyzer.

The RIN of the Toptica CTL1550 at an output of 1550 nm, injection curret at 200 mA and detected optical power at the photo diode of 300 μW is presented in Figure 4.9 along with the shot noise limit. The during measurement is Notably, the noise contains several sharp peaks and increased noise towards lower frequencies. The excess noise in the spectrum for low frequencies is attributed to electronic noise in the injections laser.

The results of the measurement show that the shot noise limit is reached for frequencies above 300 kHz implying that excess classical noise will not interfere with homodyne measurements of the membrane mechanics with frequencies above 300 kHz. Classical noise will however interfere with the PID regulators that typically operates at frequencies lower than 300 kHz.

4.4 Homodyne measurement of optical cavity output

With the aim of observing the motion of the micromechanical mirrors when coupled to the intracavity field, the optomechanical cavity is integrated into the setup described in Section 3.2.3. The input laser is first aligned to the cavity with the alignment mirrors. Using the CMOS camera and the imaging setup along with the 980 nm alignment laser, the intracavity mode is identified and placed on the sample of interest on the GaAs chip by manually moving the back cavity mirror. The device used for this experiment is the SL device discussed in previous sections. Next, the PDH error signal is generated by either scanning the cavity length or the laser wavelength which allows for frequency locking the laser to the cavity resonance. Mechanics of the back cavity mirror is detected by coupling the cavity reflection to the homodyne measurement setup and observing the response with the spectrum analyzer. As discussed in Section 4.3, the resonance of the cavity mode when focusing on the micromechanical membranes is weak due to impedance mismatch and

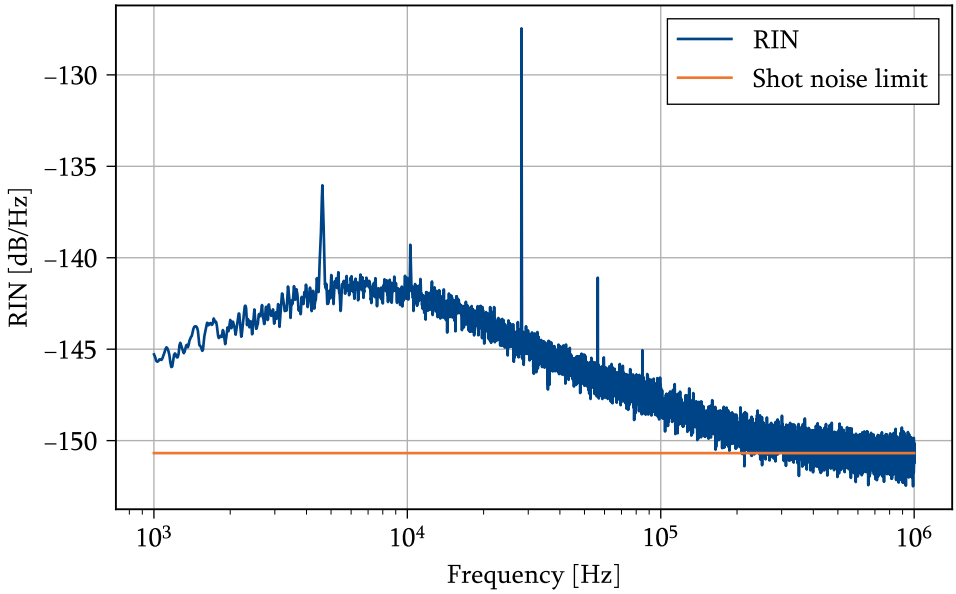

Figure 4.9: Laser intensity NPS of the Toptica CTL1550 at a laser output of 1550 nm and injection current of 200 mA. The noise contains several sharp peaks and a larger weight towards lower frequencies.

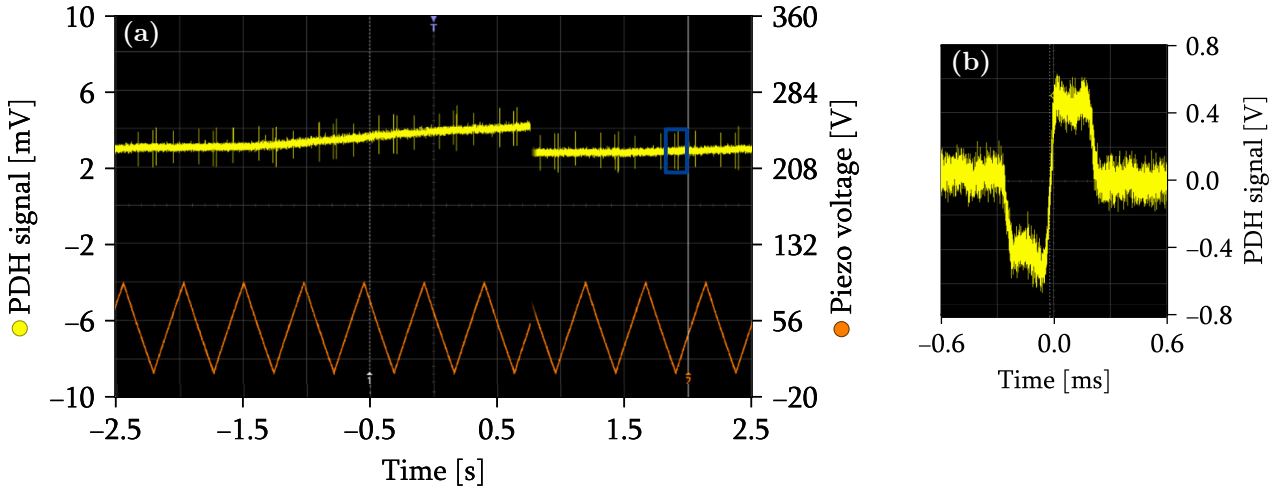

Figure 4.10: **(a)** Oscilloscope picture illustrating DC drifts in the PDH error signal. **(b)** Zoomed in view of the blue boxed area showing an amplified PDH signal.

internal cavity losses. This decrease in SNR drastically affects the ability to obtain stable, low noise cavity frequency locks. In particular, slow drifts in the DC level with comparable amplitude to the error signal offset the set point, preventing stable locks. This is shown in Figure 4.11. The observed DC drift is partly due to residual amplitude modulation (RAM) in the EOM which is converted to a DC signal in the down modulation of the PDH loop. The RAM of an EOM is highly dependent on the polarization of the input laser light which is fixed to the preferred fiber axis by inserting an in-fiber PBS before the input to the EOM. Due to excess polarization drifts in the fiber network connecting the laser output to the EOM, the PDH error signal still experience slow drifts in set point. Turning to a side of fringe locking scheme bypasses the drifts caused by polarization effects in the EOM and allows for short locks of up to 20 s using the Toptica Regulator PID110 to stabilize the cavity length, shown in Figure 4.11. During a cavity frequency lock, the displacement

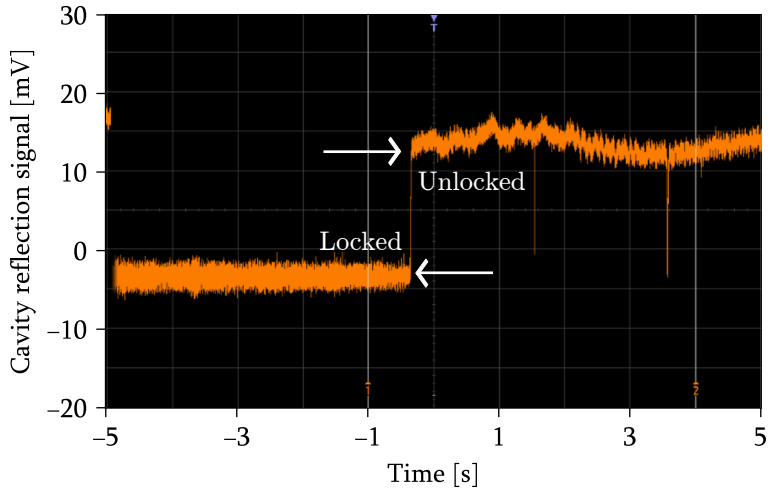

Figure 4.11: **(a)** Oscilloscope picture illustrating side of fringe locking to the optomechanical cavity. The right side of the sweep shows an unlocked state where the PID scans the cavity length occasionally hitting cavity resonance. While locked, the reflected signal is stabilized at the set point which is seen to the left side of the oscilloscope sweep.

NPS of the back cavity mirror is recorded on the spectrum analyser. Readout of the cavity back mirror displacement is confirmed by applying a calibration tone to the piezo regulating the cavity length and observing the mechanical NPS before and after successful cavity frequency lock. The calibration tone is observed on the spectrum analyzer solely when the laser frequency is locked to the cavity resonance, indicating that the signal is picked up from within the cavity. This is illustrated in Figure 4.12.

However, the mechanics of the membrane is not observed in the homodyne signal indicating a loss of mechanical signal in the measurement setup. This loss can be caused by slight misalignment in the intracavity mode focus on the device. In addition, due to the weak magnitude of the cavity resonance, small amounts of the incident light field is allowed

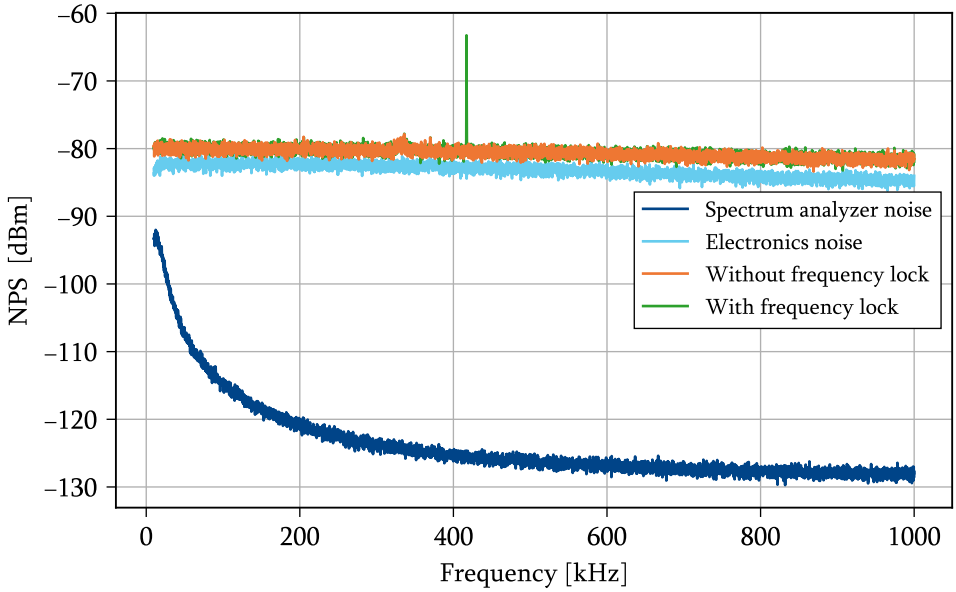

Figure 4.12: Noise levels of the homodyne readout when observing mechanical displacements from within the cavity. A pure sinusoidal tone applied to the cavity piezo is detected when the cavity is locked.

to interact with the mechanical system to pick up signal, lowering the sensitivity of the measurement. This signal is further reduced when coupled into the in-fiber part of the experimental setup where coupling efficiencies η were limited to 50 %.

4.5 Discussion

To be able to successively read out the mechanical motion of the membranes when placed in the cavity requires improvement of the experimental parameters. This includes increases in 1) cavity signal SNR, 2) stability of PID servo locks and, 3) accuracy in intracavity mode focus on the device chips. The time constraints of this thesis did not allow for further improvements of the system to successfully observe optomechanical interaction with the single and double-layer mechanical resonators. However, several accessible solutions to some problems encountered are available. The issue with weak cavity signals can be solved by optimization the reflectivity and minimizing losses of the AlGaAs devices. Increasing the radius of the membranes to 135 μm renders clipping losses negligible and should bring the cavity response of the SL device closer to that of the DBR mirror. Therefore, minimizing clipping losses can be expected to give an increase in finesse by a factor of at least 3. In terms of reflectivity, the range of high reflectivity for both the PhC membranes and the DBR back mirror is not available to the measurement laser as seen in Figure 4.2. Shifting the wavelength of maximum reflectivity for the devices into the desired range will cause a reduction of impedance mismatch and an increase in cavity signal strength. These changes will cause improvements in both frequency locking capabilities and sensitivity in mechanical readout. Another solution to solve the impedance mismatch of the cavity is

to reduce the reflectivity of the cavity input mirror which however will result in a lower cavity finesse.

To increase the mechanical properties of the membranes, new membrane and wafer designs can be considered. The lack of high tensile stress in the GaAs membranes limits strain engineering capabilities when designing the suspended membranes. The GaAs membranes have been estimated to be under a homogeneous stress in the 10 MPa range [20] whilst high stress SiN membranes reaching $Q_\mathrm{m} \cdot f_\mathrm{m}$ values of 10^{12} Hz have been reported to have stress levels surpassing 1 GPa. Turning to InGaP devices, an estimation that stress levels of over 1 GPa can be achieved for this material when grown on AlGaAs sacrificial layers has been presented [50]. This makes this platform a promising way forward for multi-element optomechanics. However, working with several layers of tensile strained membranes will make frequency matching of the membrane mechanical modes challenging as seen in Section 4.1.2. To solve this issue other frequency tuning parameters such exploiting the piezoelectricity of the employed materials might have to be considered.

A limitation to the presented cavity design is the manual alignment of intracavity focus on the device chips. The monolithic structure of the cavity and the choice of avoiding a piezo actuated stage increases cavity stability which have caused struggle for groups in the past [24]. However, the lack of a sub-micrometer actuated transverse movement of the device chip severely limits the accuracy with which the cavity mode can be focused to the membranes. This is a trade-off in limitations which might have to be taken into account going forward.

Part of the noise observed during attempts of frequency locking to the cavity is caused by mechanical or thermal drifts in the fiber network connecting the output of the laser to the optomechanical measurement setup. Moving the laser closer to the setup will allow bypassing part of the fiber propagation that might pick up polarization noise due to vibrations or local drifts in temperature. This also reduces the amount of polarization dependent components that is required to stabilize polarization drifts.

As a summary, the observed parameters of the optomechanical system when considering the fundamental mode of the SL device is presented in Table 4.2. The single photon optomechanical coupling g_0 is calculated from Equation (2.48) by using the effective mass of the fundamental mode calculated in [52]. Together with the measured results, estimated parameter values for a membrane with increased size to account for clipping losses is presented. Changes in the diameter of the membrane affect its mechanics by reducing resonance frequency and increasing effective mass. The change in frequency can be estimated by using Equation (4.1) which gives $\Omega_\mathrm{m} \propto 1/D$. For an increase of membrane diameter to $D = 130\mu$m a decrease in Ω_m by a factor of 0.57 is expected. The effect of increasing the membrane size on the quality factor of the mechanical mode is more complicated and would require numerical simulations of the system. However, by adopting a

Parameter		SL device	Modification
Mechanics			
D	[μm]	77	135
$\Omega_\mathrm{m}/2\pi$	[kHz]	425	242
Q_m		$3.5 \cdot 10^4$	10^6
Optics			
$1-R$	[ppm]	2620	840
$\mathcal{L}_\mathrm{cl}$	[ppm]	8710	0.4
$\kappa/2\pi$	[kHz]	6380	2053
$\mathcal{F}$		2370	7420
Optomechanics			
$g_0/2\pi$	[Hz]	234	177
Ω_m/κ		0.06	0.1
$C_0 = g_0^2/(\Gamma_\mathrm{m}\kappa)$		$0.7 \cdot 10^{-3}$	0.2

Table 4.2: Summary of the characterized optomechanical system utilizing a SL PhC crystal on top of a DBR mirror. Measured values of important parameters are presented along with predicted values for the same device with increased membrane diameter to account for clipping losses. Expected quality factor assumes an InGaP material system as presented in [50].

material system such as InGaP on AlGaAs, quality factors exceeding 10^6 can be expected [50].

Looking at the changes in system parameters for the two different membrane diameters indicates the intricate coupling between the optical and mechanical degrees of freedom. The optical properties are improved as clipping losses can be omitted whilst mechanical frequency and optomechanical coupling are decreased. We therefore conclude that a more significant change in cavity or chip design would have to be considered to take the next step towards observing quantum optomechanical effects. This can potentially be achieved with the DL devices studied in Section 4.1 that will offer a way to study multi-element optomechanical coupling. The device was omitted for optomechanics in this work due to its lower overall reflectivity which can be solved by successfully integrating DL devices with an underlying DBR mirror.

5. Conclusion

The work of this thesis has centered around designing, building and operating an experimental setup with the purpose of performing characterization of optomechanical devices. The working principle behind the setup relied on two experimental techniques, which were individually implemented and tested. The first technique, homodyne detection, was implemented to interferometrically read out the displacement of mechanical resonators, while the Pound-Drever-Hall technique was used to match the frequency output of a laser to the resonance condition of a Fabry-Pèrot-type cavity. Utilizing both techniques simultaneously is required to read out mechanical motion of micromechanical membranes inside a Fabry-Pèrot cavity, which allows to study the mutual interaction between the mechanical and optical degrees of freedom.

Before performing optomechanics experiments, the optical and mechanical subsystems were characterized individually. The mechanical subsystem, made up of both single- and double-layer photonic crystal membrane resonators, was characterized and showed resonance frequencies in the 100 kHz regime and room temperature quality factors of 10^4 in high vacuum environments. A mode tomography study was performed for a double-layer device, showing clear independent movement of the two 100 nm thick GaAs membranes with sub-micrometer separation.

The micromechanical membranes were fabricated from an AlGaAs heterostructure which is to serve as the back mirror of a Fabry-Pèrot cavity. Therefore, optical properties of the AlGaAs heterostructures were investigated and showed high reflectivities of > 95 % for laser light with $\lambda = 1520$ nm. Devices with and without underlying distributed Bragg reflectors (DBR) were investigated. This showed that an underlying DBR mirror is crucial for high finesse cavity implementations as it drastically increases reflectivities in the high reflectivity band of the DBR. This conclusion motivated the decision to prioritize the single-layer devices which, unlike the double-layer devices, had underlying DBR mirrors and showed clear membrane suspension.

The optical linewidth of a 10 mm long hemispheric cavity was investigated where the flat back mirror was exchangeable, allowing for integration of the high reflectivity AlGaAs heterostructures as back cavity mirrors. The optomechanical cavity formed with a single-layer (SL) device on DBR showed a cavity linewidth of 6.38(8) MHz, corresponding to a finesse of 2370(30). When analyzing the reflectivity of the cavity mirrors, a difference in reflectivity on the order of 10^2 ppm was measured for the cavity input mirror and the SL device chip. This implied severe impedance mismatch of the cavity mirrors, drastically

reducing the achievable intracavity intensity.

With the optomechanics setup, experiments were performed to read out the mechanics of the SL device while integrated into the Fabry-Pèrot cavity. It was confirmed that mechanical motion of the back cavity mirror was detected by picking up a homodyne signal when driving the cavity piezo with a periodic. However, the mechanical motion of the SL membrane was not detected in the homodyne detection spectrum. The lack of vibrating membrane signature in the homodyne spectrum was attributed to loss of mechanical signal in the setup, causing it to be exceeded by excess noise from the experimental setup. Signal loss factors were identified as

- Impedance mismatch,
- Membrane clipping losses,
- Inaccuracy in cavity mode placement on membrane devices.

Impedance mismatch reduced the detectable cavity signature to less than 1 % to what is expected for a symmetric cavity with equal reflecting mirrors, while clipping losses were estimated to reduce the detectable mechanical signal on the order of 10^3 ppm. The accuracy in placing the intracavity mode on the devices was limited by not having a piezo-actuated stage to move the device chips within the cavity. These challenges can be solved by increasing membrane size and lowering cavity input mirror reflectivity. This will greatly increase both the detectable cavity signature and fraction of intracavity light that interacts with the membrane, which will increase the signal-to-noise ratio in the homodyne signal.

Looking forward, beyond achieving optical readout of intracavity membrane mechanics, the optics and mechanics of the membrane devices can be improved to allow for sensitive optomechanical systems in the future. Given the strict reflectivity condition imposed on the device chips by the input cavity mirror, future double-layer devices should be fabricated with underlying DBR. The mechanical quality factors of the membranes are in part upper bounded by clamping loss, which can be reduced by using stress engineering and dissipation dilution in highly stressed materials, such as InGaP on GaAs. However, this can pose a problem for multi-element optomechanics which require arrays of resonators with equal resonance frequencies. For stress dominated circular membranes with high quality factors, the relative difference in membrane stress must be $< 2Q^{-1}$ to ensure equal resonance frequencies. This problem can be tackled by for instance using piezoelectric properties of the used material system in order to actively and in-situ tune the mechanical resonance frequencies.

By addressing the aforementioned challenges, the optomechanics setup presented in this thesis will allow for a platform to investigate the properties of novel optomechanical systems in the future. This includes fully integrated on-chip optomechanical microcavities with interesting applications in quantum limited sensing.

References

[1] J. Kepler, *De cometis libelli tres*, ser. De cometis libelli tres. Typis Andreæ Apergeri, sumptibus Sebastiani Mylii bibliopolæ Augustani, 1619. [Online]. Available: https://books.google.se/books?id=5Z1BQAAACAAJ.

[2] P. Lebedew, "Untersuchungen über die druckkräfte des lichtes," *Annalen der Physik*, vol. 311, no. 11, pp. 433–458, 1901. DOI: https://doi.org/10.1002/andp.19013111102. eprint: https://onlinelibrary.wiley.com/doi/pdf/10.1002/andp.19013111102. [Online]. Available: https://onlinelibrary.wiley.com/doi/abs/10.1002/andp.19013111102.

[3] E. F. Nichols and G. F. Hull, "The pressure due to radiation," *Astrophysical Journal*, vol. 17, p. 315, 1903-06.

[4] A. Ashkin, "Trapping of atoms by resonance radiation pressure," *Phys. Rev. Lett.*, vol. 40, pp. 729–732, 12 1978-03. DOI: 10.1103/PhysRevLett.40.729. [Online]. Available: https://link.aps.org/doi/10.1103/PhysRevLett.40.729.

[5] W. Neuhauser, M. Hohenstatt, P. Toschek, and H. Dehmelt, "Optical-sideband cooling of visible atom cloud confined in parabolic well," *Phys. Rev. Lett.*, vol. 41, pp. 233–236, 4 1978-07. DOI: 10.1103/PhysRevLett.41.233. [Online]. Available: https://link.aps.org/doi/10.1103/PhysRevLett.41.233.

[6] M. Aspelmeyer, T. J. Kippenberg, and F. Marquardt, "Cavity optomechanics," *Rev. Mod. Phys.*, vol. 86, pp. 1391–1452, 4 2014-12. DOI: 10.1103/RevModPhys.86.1391. [Online]. Available: https://link.aps.org/doi/10.1103/RevModPhys.86.1391.

[7] J. Chan, T. P. M. Alegre, A. H. Safavi-Naeini, *et al.*, "Laser cooling of a nanomechanical oscillator into its quantum ground state," *Nature*, vol. 478, no. 7367, pp. 89–92, 2011-10, ISSN: 1476-4687. DOI: 10.1038/nature10461. [Online]. Available: https://doi.org/10.1038/nature10461.

[8] L. Ding, C. Baker, P. Senellart, *et al.*, "Wavelength-sized gaas optomechanical resonators with gigahertz frequency," *Applied Physics Letters*, vol. 98, no. 11, p. 113 108, 2011. DOI: 10.1063/1.3563711. eprint: https://doi.org/10.1063/1.3563711. [Online]. Available: https://doi.org/10.1063/1.3563711.

[9] W. Jiang, C. J. Sarabalis, Y. D. Dahmani, *et al.*, "Efficient bidirectional piezo-optomechanical transduction between microwave and optical frequency," *Nature Communications*, vol. 11, no. 1, p. 1166, 2020-03, ISSN: 2041-1723. DOI: 10.1038/s41467-020-14863-3. [Online]. Available: https://doi.org/10.1038/s41467-020-14863-3.

[10] A. Dorsel, J. D. McCullen, P. Meystre, E. Vignes, and H. Walther, "Optical bistability and mirror confinement induced by radiation pressure," *Phys. Rev. Lett.*, vol. 51, pp. 1550–1553, 17 1983-10. DOI: 10.1103/PhysRevLett.51.1550. [Online]. Available: https://link.aps.org/doi/10.1103/PhysRevLett.51.1550.

[11] O. Arcizet, P.-F. Cohadon, T. Briant, and A. Pinard M.and Heidmann, "Radiation-pressure cooling and optomechanical instability of a micromirror," *Nature*, vol. 444, no. 7115, pp. 71–74, 2006-11, ISSN: 1476-4687. DOI: 10.1038/nature05244. [Online]. Available: https://doi.org/10.1038/nature05244.

[12] S. Gröblacher, J. B. Hertzberg, M. R. Vanner, *et al.*, "Demonstration of an ultracold micro-optomechanical oscillator in a cryogenic cavity," *Nature Physics*, vol. 5, no. 7, pp. 485–488, 2009-07, ISSN: 1745-2481. DOI: 10.1038/nphys1301. [Online]. Available: https://doi.org/10.1038/nphys1301.

[13] G. Anetsberger, R. Rivière, A. Schliesser, O. Arcizet, and T. J. Kippenberg, "Ultralow-dissipation optomechanical resonators on a chip," *Nature Photonics*, vol. 2, no. 10, pp. 627–633, 2008-10, ISSN: 1749-4893. DOI: 10.1038/nphoton.2008.199. [Online]. Available: https://doi.org/10.1038/nphoton.2008.199.

[14] M. Mirhosseini, A. Sipahigil, M. Kalaee, and O. Painter, "Superconducting qubit to optical photon transduction," *Nature*, vol. 588, no. 7839, pp. 599–603, 2020-12, ISSN: 1476-4687. DOI: 10.1038/s41586-020-3038-6. [Online]. Available: https://doi.org/10.1038/s41586-020-3038-6.

[15] J. D. Thompson, B. M. Zwickl, A. M. Jayich, F. Marquardt, S. M. Girvin, and J. G. E. Harris, "Strong dispersive coupling of a high-finesse cavity to a micromechanical membrane," *Nature*, vol. 452, pp. 72–75, 7183 2008-03. DOI: 10.1038/nature06715. [Online]. Available: https://doi.org/10.1038/nature06715.

[16] C. Gärtner, J. P. Moura, W. Haaxman, R. A. Norte, and S. Gröblacher, "Integrated optomechanical arrays of two high reflectivity sin membranes," *Nano Letters*, vol. 18, no. 11, pp. 7171–7175, 2018-11, ISSN: 1530-6984. DOI: 10.1021/acs.nanolett.8b03240. [Online]. Available: https://doi.org/10.1021/acs.nanolett.8b03240.

[17] A. Xuereb, C. Genes, and A. Dantan, "Strong coupling and long-range collective interactions in optomechanical arrays," *Phys. Rev. Lett.*, vol. 109, p. 223 601, 22 2012-11. DOI: 10.1103/PhysRevLett.109.223601. [Online]. Available: https://link.aps.org/doi/10.1103/PhysRevLett.109.223601.

[18] P. Piergentili, L. Catalini, M. Bawaj, *et al.*, "Two-membrane cavity optomechanics," *New Journal of Physics*, vol. 20, no. 8, p. 083 024, 2018-08. DOI: 10.1088/1367-2630/aad85f. [Online]. Available: https://doi.org/10.1088/1367-2630/aad85f.

[19] A. Xuereb, C. Genes, and A. Dantan, "Collectively enhanced optomechanical coupling in periodic arrays of scatterers," *Phys. Rev. A*, vol. 88, p. 053 803, 5 2013-11. DOI: 10.1103/PhysRevA.88.053803. [Online]. Available: https://link.aps.org/doi/10.1103/PhysRevA.88.053803.

[20] S. Kini Manjeshwar, K. Elkhouly, J. M. Fitzgerald, *et al.*, "Suspended photonic crystal membranes in algaas heterostructures for integrated multi-element optomechanics," *Applied Physics Letters*, vol. 116, no. 26, p. 264 001, 2020. DOI: 10.1063/5.0012667. eprint: https://doi.org/10.1063/5.0012667. [Online]. Available: https://doi.org/10.1063/5.0012667.

[21] J. P. Sethna, *Statistical Mechanics: Entropy, Order Parameters, and Complexity*. 2021-03, ISBN: 9780198865254.

[22] S. Gröblacher, A. Trubarov, N. Prigge, G. D. Cole, M. Aspelmeyer, and J. Eisert, "Observation of non-markovian micromechanical brownian motion," *Nature Communications*, vol. 6, no. 1, p. 7606, 2015-07, ISSN: 2041-1723. DOI: 10.1038/ncomms8606. [Online]. Available: https://doi.org/10.1038/ncomms8606.

[23] W. T. Coffey, Y. P. Kalmykov, and J. T. Waldron, *Langevin Equation, The: With Applications To Stochastic Problems In Physics, Chemistry And Electrical Engineering (2nd Edition) : With Applications to Stochastic Problems in Physics, Chemistry, and Electrical Engineering*. Singapore, SINGAPORE: World Scientific Publishing Company, 2004, ISBN: 9789812795090. [Online]. Available: http://ebookcentral.proquest.com/lib/chalmers/detail.action?docID=1679721.

[24] S. Gröblacher, *Quantum Opto-Mechanics with Micromirrors: Combining Nano-Mechanics with Quantum Optics*. Berlin, Heidelberg: Springer Berlin Heidelberg, 2012, ISBN: 978-3-642-34955-3. DOI: 10.1007/978-3-642-34955-3. [Online]. Available: https://doi.org/10.1007/978-3-642-34955-3.

[25] J. J. Sakurai and J. Napolitano, *Modern Quantum Mechanics*, 2nd ed. Cambridge: Cambridge University Press, 2017. DOI: 10.1017/9781108499996. [Online]. Available: https://doi.org/10.1017/9781108499996.

[26] J. D. Teufel, T. Donner, D. Li, *et al.*, "Sideband cooling of micromechanical motion to the quantum ground state," *Nature*, vol. 475, no. 7356, pp. 359–363, 2011-07, ISSN: 1476-4687. DOI: 10.1038/nature10261. [Online]. Available: https://doi.org/10.1038/nature10261.

[27] H.-A. Bachor and T. C. Ralph, *A Guide to Experiments in Quantum Optics*. John Wiley & Sons, Ltd, 2004, ISBN: 9783527619238. DOI: https://doi.org/10.1002/9783527619238. eprint: https://onlinelibrary.wiley.com/doi/pdf/10.1002/9783527619238. [Online]. Available: https://onlinelibrary.wiley.com/doi/abs/10.1002/9783527619238.

[28] H. Kogelnik and T. Li, "Laser beams and resonators," *Appl. Opt.*, vol. 5, no. 10, pp. 1550–1567, 1966-10. DOI: 10.1364/AO.5.001550. [Online]. Available: http://ao.osa.org/abstract.cfm?URI=ao-5-10-1550.

[29] S. Feng and H. Winful, "Physical origin of the gouy phase shift," *Optics letters*, vol. 26, pp. 485–7, 2001-05. DOI: 10.1364/OL.26.000485.

[30] C. Gerry and P. Knight, *Introductory Quantum Optics*. Cambridge University Press, 2004. DOI: 10.1017/CBO9780511791239.

[31] B. Yurke, "Input-output theory," in *Quantum Squeezing*, P. D. Drummond and Z. Ficek, Eds. Berlin, Heidelberg: Springer Berlin Heidelberg, 2004, pp. 53–96, ISBN: 978-3-662-09645-1. DOI: 10.1007/978-3-662-09645-1_3. [Online]. Available: https://doi.org/10.1007/978-3-662-09645-1_3.

[32] J. F. Goodwin, G. Stutter, R. C. Thompson, and D. M. Segal, "Resolved-sideband laser cooling in a penning trap," *Physical Review Letters*, vol. 116, no. 14, 2016-04, ISSN: 1079-7114. DOI: 10.1103/physrevlett.116.143002. [Online]. Available: http://dx.doi.org/10.1103/PhysRevLett.116.143002.

[33] U. Delić, M. Reisenbauer, K. Dare, *et al.*, "Cooling of a levitated nanoparticle to the motional quantum ground state," *Science*, vol. 367, no. 6480, pp. 892–895, 2020, ISSN: 0036-8075. DOI: 10.1126/science.aba3993. eprint: https://science.sciencemag.org/content/367/6480/892.full.pdf. [Online]. Available: https://science.sciencemag.org/content/367/6480/892.

[34] A. Imamo ḡlu, H. Schmidt, G. Woods, and M. Deutsch, "Strongly interacting photons in a nonlinear cavity," *Phys. Rev. Lett.*, vol. 79, pp. 1467–1470, 8 1997-08. DOI: 10.1103/PhysRevLett.79.1467. [Online]. Available: https://link.aps.org/doi/10.1103/PhysRevLett.79.1467.

[35] P. Rabl, "Photon blockade effect in optomechanical systems," *Phys. Rev. Lett.*, vol. 107, p. 063 601, 6 2011-08. DOI: 10.1103/PhysRevLett.107.063601. [Online]. Available: https://link.aps.org/doi/10.1103/PhysRevLett.107.063601.

[36] D. Bouwmeester, A. Ekert, and A. Zeilinger, *The Physics of Quantum Information*. Berlin, Heidelberg: Springer Berlin Heidelberg, 2000, ISBN: 978-3-662-04209-0. DOI: 10.1007/978-3-662-04209-0. [Online]. Available: https://doi.org/10.1007/978-3-662-04209-0.

[37] I. Sukhoivanov and I. Guryev, *Photonic Crystals. Physics and Practical Modeling*. 2009-01, ISBN: 978-3-642-02645-4.

[38] W. Zhou, D. Zhao, Y.-C. Shuai, *et al.*, "Progress in 2d photonic crystal fano resonance photonics," *Progress in Quantum Electronics*, vol. 38, no. 1, pp. 1–74, 2014, ISSN: 0079-6727. DOI: https://doi.org/10.1016/j.pquantelec.2014.01.001. [Online]. Available: https://www.sciencedirect.com/science/article/pii/S0079672714000020.

[39] H. Yang, D. Zhao, J.-H. Seo, *et al.*, "Broadband membrane reflectors on glass," *IEEE Photonics Technology Letters - IEEE PHOTONIC TECHNOL LETT*, vol. 24, pp. 476–478, 2012-03. DOI: 10.1109/LPT.2011.2181351.

[40] E. D. Black, "An introduction to pound–drever–hall laser frequency stabilization," *American Journal of Physics*, vol. 69, no. 1, pp. 79–87, 2001. DOI: 10.1119/1.1286663. eprint: https://doi.org/10.1119/1.1286663. [Online]. Available: https://doi.org/10.1119/1.1286663.

[41] K. Elkhouly, *High Reflectivity GaAs-based Photonic Crystal Reflectors for Cavity Optomechanics*. 2019.

[42] D. Z. Anderson, "Alignment of resonant optical cavities," *Appl. Opt.*, vol. 23, no. 17, pp. 2944–2949, 1984-09. DOI: 10.1364/AO.23.002944. [Online]. Available: http://ao.osa.org/abstract.cfm?URI=ao-23-17-2944.

[43] D. Hunger, T. Steinmetz, Y. Colombe, C. Deutsch, T. W. Hänsch, and J. Reichel, "A fiber fabry–perot cavity with high finesse," *New Journal of Physics*, vol. 12, no. 6, p. 065 038, 2010-06. DOI: 10.1088/1367-2630/12/6/065038. [Online]. Available: https://doi.org/10.1088/1367-2630/12/6/065038.

[44] S. Schmid, L. G. Villanueva, and M. L. Roukes, "Resonance frequency," in *Fundamentals of Nanomechanical Resonators*. Cham: Springer International Publishing, 2016, pp. 1–56, ISBN: 978-3-319-28691-4. DOI: 10.1007/978-3-319-28691-4_1. [Online]. Available: https://doi.org/10.1007/978-3-319-28691-4_1.

[45] M. Imboden and P. Mohanty, "Dissipation in nanoelectromechanical systems," *Physics Reports*, vol. 534, no. 3, pp. 89–146, 2014, Dissipation in nano-electromechanical systems, ISSN: 0370-1573. DOI: https://doi.org/10.1016/j.physrep.2013.09.003. [Online]. Available: https://www.sciencedirect.com/science/article/pii/S0370157313003475.

[46] R. A. Norte, J. P. Moura, and S. Gröblacher, "Mechanical resonators for quantum optomechanics experiments at room temperature," *Phys. Rev. Lett.*, vol. 116, p. 147 202, 14 2016-04. DOI: 10.1103/PhysRevLett.116.147202. [Online]. Available: https://link.aps.org/doi/10.1103/PhysRevLett.116.147202.

[47] C. Reinhardt, T. Müller, A. Bourassa, and J. C. Sankey, "Ultralow-noise sin trampoline resonators for sensing and optomechanics," *Phys. Rev. X*, vol. 6, p. 021 001, 2 2016-04. DOI: 10.1103/PhysRevX.6.021001. [Online]. Available: https://link.aps.org/doi/10.1103/PhysRevX.6.021001.

[48] P.-L. Yu, K. Cicak, N. S. Kampel, *et al.*, "A phononic bandgap shield for high-q membrane microresonators," *Applied Physics Letters*, vol. 104, no. 2, p. 023 510, 2014. DOI: 10.1063/1.4862031. eprint: https://doi.org/10.1063/1.4862031. [Online]. Available: https://doi.org/10.1063/1.4862031.

[49] Y. Tsaturyan, A. Barg, E. S. Polzik, and A. Schliesser, "Ultracoherent nanomechanical resonators via soft clamping and dissipation dilution," *Nature Nanotechnology*, vol. 12, no. 8, pp. 776–783, 2017-08, ISSN: 1748-3395. DOI: 10.1038/nnano.2017.101. [Online]. Available: https://doi.org/10.1038/nnano.2017.101.

[50] G. D. Cole, P.-L. Yu, C. Gärtner, *et al.*, "Tensile-strained inxga1xp membranes for cavity optomechanics," *Applied Physics Letters*, vol. 104, no. 20, p. 201 908, 2014-05, ISSN: 0003-6951. DOI: 10.1063/1.4879755. [Online]. Available: https://doi.org/10.1063/1.4879755.

[51] M. Rossi, D. Mason, J. Chen, Y. Tsaturyan, and A. Schliesser, "Measurement-based quantum control of mechanical motion," *Nature*, vol. 563, no. 7729, pp. 53–58, 2018-11, ISSN: 1476-4687. DOI: 10.1038/s41586-018-0643-8. [Online]. Available: https://doi.org/10.1038/s41586-018-0643-8.

[52] B. Hauer, C. Doolin, K. Beach, and J. Davis, "A general procedure for thermomechanical calibration of nano/micro-mechanical resonators," *Annals of Physics*, vol. 339, pp. 181–207, 2013, ISSN: 0003-4916. DOI: https://doi.org/10.1016/j.aop.2013.08.003. [Online]. Available: https://www.sciencedirect.com/science/article/pii/S0003491613001723.

A. Appendix - Free space optics setup

Presented in Figure A.1 is the free space optics part of the setup presented in Section 3.2.3. The setup is split up into three sections: Alignment, Detection, and Imaging. The alignment and detection setups use the telecom measurement laser at telecom wavelengths $\lambda \sim 1550$ nm (depicted in red) whilst the imaging setup uses the white light output of a Thorlabs MCWHF2 6200 K LED (depicted in blue).

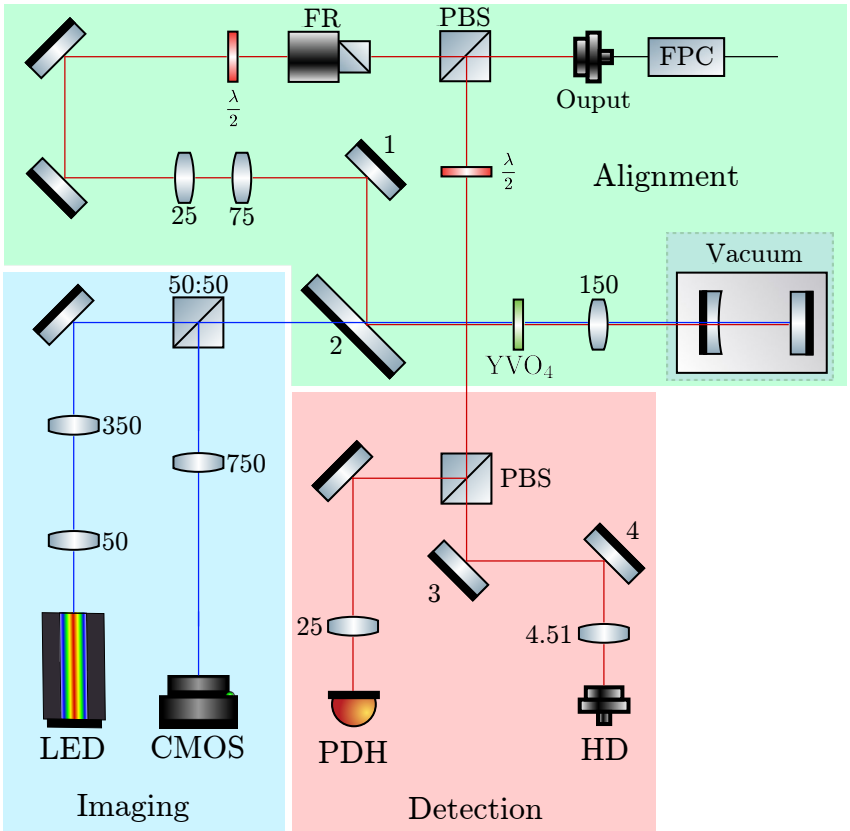

Figure A.1: Free space optics part of the optomechanics experimental setup. It consists of three sections, Alignment, Detection and Imaging. The red beam path depicts telecom measurement laser, whilst the blue beam path depicts white LED light used for imaging. For detailed description, see main text. FPC = Fiber coupled polarization controller, PBS = Polarizing beam splitter, FR = Faraday rotator, PDH = Pound-Drever-Hall, HD = Homodyne detection.

The telecom laser is first coupled to free space with a Thorlabs TC12APC-1550 triple triplet collimator, producing a beam with waist radius $w = 1.13$ mm. The free space beam first encounters a polarizing beam splitter (PBS), which filters away the vertical polarization component. Controlling the amount of light in each polarization state is performed with a fiber-coupled polarization controller (FPC) before laser output. Next, the beam travels through a Faraday Rotator (FR) and a half-wave plate, the purpose of which is to rotate the reflected beam to vertical polarization. Lenses and mirror pair $(1, 2)$ now mode match the beam to the cavity before the beam hits an yttrium orthovanadate (YVO_4) crystal, which rotates the polarization of the input beam to the coordinate system of the cavity. Finally, the beam is focused down on the back cavity mirror, where the micromechanical membranes are placed.

The returning reflection is guided along the input path, but is reflected on the first PBS due to the half-wave plate and FR. This beam now enters the detection part of the setup and is first split up on a PBS. The reflection is directed to a photodiode (PD) which picks up the raw reflection signal that is used for Pound-Drever-Hall locking. The transmission of the PBS is mode matched with mirror pair $(3, 4)$ to the input of a single mode optical fiber, where the signal is led to homodyne detection of membrane mechanics.

The imaging setup follows the principles described in 3.2.5 to light up the interior of the cavity and take images with a Chameleon®3 color camera (CMOS). Since the mirror labeled 2 is designed for high reflectivity at telecom wavelengths, it is semi-transparent for the white LED light used for imaging. The cavity focusing lens serves as objective lens and produces a magnification of 3 on the CMOS camera.

DEPARTMENT OF MICROTECHNOLOGY AND NANOSCIENCE
CHALMERS UNIVERSITY OF TECHNOLOGY
Gothenburg, Sweden
www.chalmers.se

CHALMERS
UNIVERSITY OF TECHNOLOGY